Author:
Oner, Bahar

Title:
Sub-Micron Resolution Hyperspectral Quantum Rod Thermal Imaging and Thermal Challenges of AlGaN/GaN Power Devices

Sub-Micron Resolution Hyperspectral Quantum Rod Thermal Imaging and Thermal Challenges of AlGaN/GaN Power Devices

By

BAHAR ÖNER

Department of Physics
UNIVERSITY OF BRISTOL

A dissertation submitted to the University of Bristol in accordance with the requirements of the degree of DOCTOR OF PHILOSOPHY in the Faculty of Science.

FEBRUARY 2020

Word count:37,158

Abstract

Device life-time and performance is directly linked to its operating temperature, which necessitates accurate temperature measurements. However, reliable temperature measurement at the device level is challenging due to small device dimensions which are on the order of micrometres. Considering that the trend is toward the miniaturisation of electronic devices, from the micro-scale to the nano-scale, temperature measurements become even more challenging. The available techniques have limitations in terms of either resolution, calibration, acquisition time or equipment cost. This thesis provides an alternative solution to address these challenges by developing a new thermography technique called hyperspectral quantum rod thermal imaging (HQTI), which exploits temperature dependent photoluminescence (PL) emission of quantum rods to obtain the surface temperature map of a biased electronic device, with a straight-forward calibration. This method uses relatively simple, low cost equipment, while achieving sub-micron spatial resolution. This technique is demonstrated by measuring the thermal map of a direct current (DC) operated Gallium Nitride (GaN) high electron mobility transistor (HEMT), achieving an average temperature precision of 4^{o}C, and a 680±20 nm measured lateral optical resolution. The technique was benchmarked against the standard infrared (IR) thermography and it was shown that IR underestimated device thermal resistance by 3 times for the device under test. HQTI is a versatile method for both measurement in sub-micron scale regions of interest and of larger areas in the hundreds of micrometres range. The technique is further extended to time resolved measurements, (T-HQTI), to be able to characterise thermal dynamics of a pulsed operated device. An average time resolution of 20 μs was achieved with the box-car averaging approach. T-HQTI measurements were also verified with sub-micron resolution transient thermoreflectance thermometry (TTR) and a good agreement was found for the 100s of MHz operating regime, which is the typical switching rate for power devices.

Multi-finger enhancement mode GaN-on-Si power devices, which are of concern for the cost-competitive power semiconductors industry, were also thermally assessed at the wafer level, using a combination of thermal measurements and finite element thermal simulations. Identifying thermal bottlenecks of the GaN power devices is critical in order to provide the most cost-effective cooling solution as these devices operate at high powers and any development is limited by the cost constraints. We identified the substrate as the main thermal bottleneck while buffer layer (along with the strain relief layer) possesses a negligible thermal resistance for these large area power devices. It was suggested that thinning the substrate by 7 times could reduce the junction temperature by down to 70% at DC operation, supported by calibrated finite element simulations.

The developments carried out and the findings of this work are expected to help achieving the maximum benefits of GaN technology. The impact of the new thermography technique is even expected to be wider as it can be adopted to, for example, biomedical applications or composite materials, where thermal dynamics at the sub-micron scale are of interest.

Acknowledgements

I would like to thank my supervisor Prof. Martin Kuball for offering me this opportunity. I had not considered doing my PhD in Physics with my mechanical engineering background up until his offer. He paved the way for me to have this interesting experience and has been supportive when needed during my PhD studies. The second thanks goes to Dr. James Pomeroy, from whom I learned many life lessons in addition to trying to ask the next good question (and also to answer!). I also enjoyed his humour in the lab from time to time and found his technical knowledge quite impressive and helpful, which deserve another thanks.

Another big thanks goes to Infineon Technologies and University of Bristol Alumni Foundation for having fully sponsored my PhD. I would like to thank Dr. Clemens Ostermaier from Infineon Technologies for sending us the devices we used in this work and being our point of contact there, when needed. I do thank Dr. Natasa Vasiljevic and Prof. Michael Uren for their helpful feedback during my annual progress monitoring meetings. I also would like to thank Dr. Andrew Murray for his help in the cleanroom. The mechanical workshop team, and in particular Patrick Alexander and Adrian Crimp, have been very timely and helpful whenever I needed a part for my set-up; thanks for this.

There have been very nice people I met in CDTR and also in the PhD office, who brought joy to my time in Bristol. Special thanks go to Filip Gucmann and Stefano Dalcanale for making the work more fun and sometimes easier. I particularly acknowledge Stefano for having read several chapters of my thesis and providing useful feedback. I also would like to thank the exclusive members of the Film Club, in the PhD office. I very much enjoyed our movie sessions even though they found my film choices a bit unusual. Thanks also go to Zuzana Gucmann for her friendship. Outside the work, I also would like to thank METU alumni, who I met in Bristol and have been my company here: specifically Dondu Sahin, Sema Dumanli Oktar, Mehmet Alper Oktar, Merve Cayir Kucukdisli and Murat Kucukdisli. Special thanks go to Eylul Simsek and Deniz Turan for their long-lasting friendship despite the pond in between. I would like to particularly thank Deniz for sharing his technical insights with me whenever asked. There have been many other METU alumni, who touched my life even when I was miles away from home; I thank all of them for their kindness. I also would like to thank Prof. Hakan Erturk from Bogazici University for sharing his wisdom and experiences with me at the beginning of my PhD, which I found eye-opening.

Finally, I would like to thank my family for their support and love. I specifically thank my parents for instilling universal values in me and unconditionally loving me and my sister for her very special and invaluable friendship and support since my university years. Last but not least, I would like to thank my fiancé, Oktay, who has been beyond supportive during my PhD studies. Although we have been miles away in this period, I have always felt his love and support and enjoyed every minute of our very limited time together in the last four years. Thanks for bringing me joy during this journey despite the distances.

AUTHOR'S DECLARATION

I declare that the work in this dissertation was carried out in accordance with the requirements of the University's Regulations and Code of Practice for Research Degree Programmes and that it has not been submitted for any other academic award. Except where indicated by specific reference in the text, the work is the candidate's own work. Work done in collaboration with, or with the assistance of, others, is indicated as such. Any views expressed in the dissertation are those of the author.

SIGNED: ..... DATE: .....

TABLE OF CONTENTS

Page

List of Tables **xi**

List of Figures **xiii**

Acronmys and Abbreviations **xvii**

1 Introduction **1**

2 Theoretical Background **9**

2.1 GaN based materials and devices 9

2.1.1 Crystal properties of wurtzite GaN 9

2.1.2 Phonons in wurtzite GaN 13

2.1.3 GaN based High Electron Mobility Transistor (HEMT) 14

2.1.4 Growth methods 26

2.2 Temperature dependent photoluminescence of quantum rods (QRs) 27

2.2.1 Size effects in low dimensional systems 27

2.2.2 Fabrication techniques and morphology of quantum rods 29

2.2.3 Photoluminescence 30

2.2.4 Quantum rods as temperature sensors 33

2.3 Heat conduction in solids 34

3 Complementary experimental methods **39**

3.1 Raman thermography 40

3.1.1 Basics of Raman scattering 40

3.1.2 Raman thermography 46
3.2 Infrared (IR) Thermography 57
3.2.1 Quantum Focus Instruments (QFI) Infrared System 57
3.3 Transient Thermoreflectance (TTR) Thermometry 60

4 Hyperspectral Quantum Rod Thermal Imaging (HQTI): Demonstrated on a GaN HEMT 65

4.1 The working principle of the technique 65
4.2 Experimental set-up 67
4.3 Device details and the effect of QR deposition on device performance 84
4.4 Image processing 88
4.5 Results and Discussion 91
4.6 Additional considerations 100
4.7 Conclusion 106

5 Time Resolved Hyperspectral Quantum Rod Thermal Imaging: Temperature Transients in a GaN HEMT 107

5.1 Experimental set-up and device details 108
5.2 Results and Discussion 111
5.3 Conclusion 119

6 Thermal Bottlenecks of GaN on Silicon Multifinger Power Devices 121

6.1 Multi-Finger Power Device Details 122
6.2 Wafer level thermal characterisation 122
6.3 Conclusion 129

7 Conclusion and Future Work 131

7.1 Future Work 135

A Error Analysis and Supporting Data for the HQTI system 137

A.1 Error Analysis 137

A.2 Supporting Data 139
A.2.1 Thermal Image and Noise for a Single Acquisition 139

B Publications and Conferences Attended **141**
B.1 Publications 141
B.2 Conference Presentations 141

Bibliography **143**

List of Tables

Table **Page**

2.1 Bulk material properties at room temperature for selected semiconductors used for power devices. 15

List of Figures

Figure **Page**

1.1 A sample Arrhenius plot where the data points (red triangles) represent the high temperature tests performed at various temperatures between 270^{o}C and 310^{o}C. . . 4

2.1 The wurtzite crystal structure of GaN. 10

2.2 The first Brillouin zone of the wurtzite GaN and its band structure. 11

2.3 Change in the band gap and the lattice constant of nitrides with alloying. 12

2.4 Phonon dispersion curve of the wurtzite GaN. 14

2.5 Schematics of a typical lateral GaN HEMT and 2DEG formation. 17

2.6 Channel formation in a normally-OFF p-GaN HEMT. 21

2.7 Output and transfer characteristics of a normally-ON HEMT. 25

2.8 0-D structure and a sample energy band diagram. 30

2.9 Schematics showing the relaxation mechanisms of an exciton in quantum rods. 32

2.10 Red shift in the photoluminescence emission peak with the increase in quantum dot size. 33

2.11 Sample mesh of a HEMT in ANSYS. 38

3.1 Schematic of quantum mechanical interpretation of scattering 41

3.2 Schematic of GaN crystal and its optical phonon modes 45

3.3 Schematic of Raman spectroscopy set-up. 49

3.4 Sample Raman spectrum of the GaN-on-Si device at room temperature. 51

3.5 Sample Raman spectrum of the TiO_2 deposited GaN-on-Si device at room temperature. 53

3.6 Working principle of the time resolved Raman thermography 55

3.7 Schematic of the acousto-optic modulator (AOM) and the optical set-up of the time resolved Raman thermography 56
3.8 Schematic of QFI IR thermography set-up. 58
3.9 Response of the IR system. 59
3.10 Spectrum of C_{th} measured in the case of bare gold (circles), and calculated in the case of Si_3N_4 coated gold (line). 64
3.11 Schematic of TTR set-up. 64

4.1 The schematic of the test set-up. 68
4.2 The schematic of the basic working principle and the image of the liquid crystal tunable filter used in this work 70
4.3 The transmission properties of the liquid crystal tunable filter(LCTF) used in this work 71
4.4 Emission images of the QR deposited test structure where electroluminesence is observed. 72
4.5 Optical resolution measurement 75
4.6 MRTD test set-up 77
4.7 The emission images of the calibration sample (QRs drop casted on a Si piece) from 440-720 nm 78
4.8 Temperature calibration function with and without image correction 80
4.9 Temperature calibration of the QRs deposited on a Si piece and a sample spectrum when DUT is operated 82
4.10 The verification of the full FOV calibration approach by investigating the calibration parameters across various ROIs by 50x50 pixel area 83
4.11 DUT details 84
4.12 Sample SEM image of the QR deposited DUT 85
4.13 Sample emission intensity of QRs through the emission spectrum, at the region of interest (ROI) of the DUT. 86
4.14 Thickness measurements with the AFM at the edge of the QR deposition. 87
4.15 Transfer and output characteristics after quantum rod deposition. 88

4.16 Image processing flowchart for temperature map reconstruction from emission images. 89

4.17 Kernel fit to the reconstructed temperature map on a DUT held at 25^oC. 90

4.18 Temperature rise vs P_{diss} maps in the ROI. 92

4.19 Thermal conductivity estimation of the strain relief layer (SRL) using a combination of Raman thermography and thermal FEM simulations. 95

4.20 Thermal FEM simulation of the GaN HEMT 96

4.21 Simulated effect of the QR thermal resistance on the measured temperature 97

4.22 Temperature rise (ΔT) maps of GaN on Si single finger device. 97

4.23 Temperature line profile and temperature rise(ΔT) vs power dissipation 99

4.24 QR heating and stability due to optical absorption. 101

4.25 SNR change with temperature to estimate acquisition time. The data shown is from the calibration. 102

4.26 The effect of Quantum Confined Stark Effect on the HQTI measurements for the ON state: V_{ds}=10 V, V_{gs}=5 V, I_{ds}=83.2 mA. 104

4.27 QR layer removal by sonication. 105

5.1 The schematic of the operating principle of the time resolved HQTI set-up. 108

5.2 Experimental set-up for the T-HQTI measurements 110

5.3 Temperature transients (absolute) of the DUT during the device pulse period, measured with time resolved HQTI. 112

5.4 The schematics of the location of the temperature measurements and their corresponding depth resolution on the DUT. 115

5.5 The effect of nanoparticle deposition on the transient dynamics of the single finger GaN-on-Si device, which is identical to the device on which T-HQTI was performed, to verify that the thermal time constant of the "clean" device is unaffected by TiO_2 nanoparticle deposition. 116

5.6 TTR calibration with TiO_2 assisted transient Raman measurements performed at the same location on the source connected field plate metal of the DUT. 117

5.7 Comparison of TTR and T-HQTI measurements on the source connected field plate metal of the GaN HEMT device. 117

6.1 Multi-finger design of power devices 123
6.2 Thermal model implementation for multi-finger power devices 124
6.3 Thermal model and the verification of the heating profile assumption by IR thermography. 125
6.4 Raman thermography and simulated temperature of the channel and through the depth of the 100-finger-device epilayer. 127
6.5 The effect of device geometry on the temperature rise. 128

A.1 Sample HQTI images and the line profiles across the channel for a single image acquisition, showing the noise before averaging. 139

Acronmys and Abbreviations

- **MOSFET** : Metal oxide field effect transistor
- **IGBT** : Insulated-gate bipolar transistor
- **MESFET** : Metal semiconductor field effect transistor
- **HEMT** : High electron mobility transistors
- **WBG** : Wide band gap
- **LED** : Light emitting diode
- **RF** : Radio frequency
- **DC** : Direct current
- **AC** : Alternative current
- **MTTF** : Mean time to failure
- **IR** : Infrared
- **AFM** : Atomic force microscopy
- **SThM** : Scanning thermal microscopy
- **PCB** : Printed circuit board
- **LDA** : Local density approximation
- **LCAO** : Linear combination of atomic orbitals

- **2DEG** : Two dimensional electron gas
- **CMOS** : Complementary metal-oxide-semiconductor
- **GIT** : Gate injection transistor
- **CTE** : Coefficient of thermal expansion
- **SRL** : Strain relief layer
- **TBR**$_{eff}$: (Effective) thermal boundary resistance
- **MBE** : Molecular beam epitaxy
- **MOCVD** : Metal organic chemical vapor deposition
- **UHV** : Ultra high vacuum
- **QR** : Quantum rod
- **QE** : Quantum efficiency
- **PL** : Photoluminescence
- **AMM** : Acoustic mismatch model
- **DMM** : Diffuse mismatch model
- **FEM** : Finite element method
- **HQTI** : Hyperspectral quantum rod thermal imaging
- **TTR** : Transient thermoreflectance
- **SNR** : Signal-to-noise ratio
- **CCD** : Charged coupled detector
- **FWHM** : Full-width-at-half-maximum
- **AOM** : Acoustooptic modulator

- **CW** : Continous wave
- **DUT** : Device under test
- **FOV** : Field of view
- **LCTF** : Liquid crystal tunable filter
- **ROI** : Region of interest
- **EL** : Electroluminescence
- **PSF** : Point spread function
- **NA** : Numerical aperture
- **LSF** : Line spread function
- **MRTD** : Minimum resolvable temperature difference
- **IPA** : Isopropyl alcohol
- **DFT** : Discrete Fourier Transform
- **NRMSE** : Normalized root mean square error
- **FFT** : Fast Fourier Transform
- **SEM** : Scanning electron microscope
- **MAD** : Mean absolute deviation
- **QCSE** : Quantum confined Stark effect
- **T-HQTI** : Time resolved (transient) hyperspectral quantum rod thermal imaging
- **LR** : Low resolution

CHAPTER 1

INTRODUCTION

Many electronic inventions that we take for granted today are in fact a result of the dedicated investments of the defense industry, which are then commercialized and turn into the products that we use in our daily lives, such as the internet, drones and surveillance cameras to name a few. Transistors are also one of those inventions, the research efforts on which started during World War II in order to replace bulky, energetically inefficient and short lifetime vacuum tubes used for signal amplification. Since the demonstration of the first transistor, made of germanium, in December 1947, by Shockley and his co-workers Bardeen and Brattain in Bell Laboratories [1, 2], there has been ever growing interest in improving its performance and reliability, for example in terms of reduced leakage currents, higher operating temperature and higher operating frequency with a long-lasting durability, all of which to be accomplished preferably at a low cost. These motivations paved the way for silicon transistors, which were first fabricated by Tanenbaum in 1955 [3] and were able to withstand higher temperatures and have lower leakage currents compared to its germanium counterparts due to its higher band gap (Ge band gap: 0.7 eV ; Si band gap: 1.1 eV). Since then, silicon based transistors have been dominating the ≈ $400 billion-revenue-semiconductor industry as of 2020 [4]. These devices are used not only for signal amplification but also for power conversion and switching applications. Silicon-based metal oxide field effect transistors

(MOSFETs), insulated-gate bipolar transistors (IGBTs) and thyristors dominate today's power conversion applications.

Despite the dominance of Si devices in the industry, simultaneous efforts have been ongoing to explore *compound semiconductors*, such as III-V group semiconductors, e.g. GaAs and GaN, which could potentially allow higher operating frequencies. The first GaAs metal semiconductor field effect transistor (MESFET) was realised in 1966 [5], exploiting the superior material properties of GaAs, such as 5x higher electron mobility than that of Si [6]. This was followed by the first demonstration of GaAs high electron mobility transistors (HEMT) in 1980, which gave 5.5x higher mobility and 3x larger transconductance compared to GaAs MESFET [7]. The shift from Si, Ge and GaAs based devices to the devices based on *wide band gap (WBG)* semiconductors, which have a band gap of 2-4 eV, started with the high quality single crystal growth of GaN (3.4 eV) and achieving p-type doping with Mg in the late 1980s and early 1990s [8, 9]. This achievement enabled the fabrication of the first blue GaN, p-n junction, light emitting diodes (LEDs) and brought the Nobel Prize to Akasaki, Amano and Nakamura in 2014. Having available techniques for the growth of epitaxial GaN, the first GaN HEMT was demonstrated in 1993 [10]. 10x larger breakdown strength and 1.5x higher electron mobility of GaN than those of Si (Si electron mobility: 1350 $cmV^{-1}s^{-1}$; GaN electron mobility: 2000 cm $V^{-1}s^{-1}$ (within the *2 dimensional electron gas* (2DEG)) [11]) translate into more compact devices operating at higher frequencies for the same application range.

GaN-based devices have been commercialised as radio frequency (RF) amplifiers in the first decade of 2000s; yet, commercial GaN power devices are relatively new for power conversion applications and there have been increasing research efforts to optimise GaN HEMTs for power applications [12]. This research direction is motivated by the increasing demand for electric generation worldwide, which is projected to increase more than 50% in the next 25 years [13]. Power electronics comes into play to distribute and convert this energy for the end-user. It is projected that by 2030, 80% of the electricity generated will be processed through power electronics [14]. It is estimated that GaN devices can increase the power conversion efficiency by 3% (for DC-AC conversion) to 10% (for DC-DC conversion) [15]. These high efficiencies due to lower power losses also mean reduced cooling needs and more compact power modules. The

GaN power industry has focused on GaN grown on Si substrates due to their low cost, taking advantage of the already established Si processing line technology. However, integrating such dissimilar materials has been a challenge due to their different lattice constant and coefficient of thermal expansion [16]. The integration has been successfully achieved by incorporating various interlayers, also known as strain relief layers, resulting in acceptable levels of defect densities at the interface and 650 V devices have already been demonstrated [16]. Yet, the industry aims to reach 1200 V and beyond [16]. Optimisation of the GaN-on-Si integration and strain relief layers is an important aspect to reach this target as these layers affect thermo-electrical performance by introducing interface resistance and traps.

As the intrinsic properties of GaN enable the miniaturisation of devices, along with advances in the fabrication technologies, there is an increasing demand in operating these devices at high powers. Reduced device dimensions and high power operations result in increased power densities, due to Joule heating (self-heating), reaching up to tens of W/mm, and increase device temperature up to 175^{o}C [17, 18] and temperature gradients of 10's ^{o}C/µm [17]. This requires incorporating thermal considerations into device design. Increased channel temperatures due to high power densities limit device performance as, for example, threshold voltage and device ON resistance are temperature dependent. Device lifetime is also impacted by the peak channel temperature. In the semiconductor industry, the standard to predict device lifetime is conducting accelerated life tests. These tests are performed by varying only one parameter, either voltage or temperature at a time; often temperature. Lifetime of the device is estimated at each set of temperature and extrapolated to the temperature of interest [19]. The failure of the device is defined as, for example, 20% change in the drain current [19]. Mean time to failure (MTTF), which is the average time that it takes for a device to fail, is given by Arrhenius relation:

$$MTTF = A\frac{-E_a}{k_B T} \tag{1.1}$$

where A is a constant of proportionality, E_a is the activation energy of the lowest energy failure mechanism which can be thermally induced, k_b is the Boltzmann constant and T is the peak channel temperature [20]. For example, if the targeted operation temperature is 175 ^{o}C, the accelerated tests are performed at various temperatures between 270^{o}C and 310^{o}C and extrap-

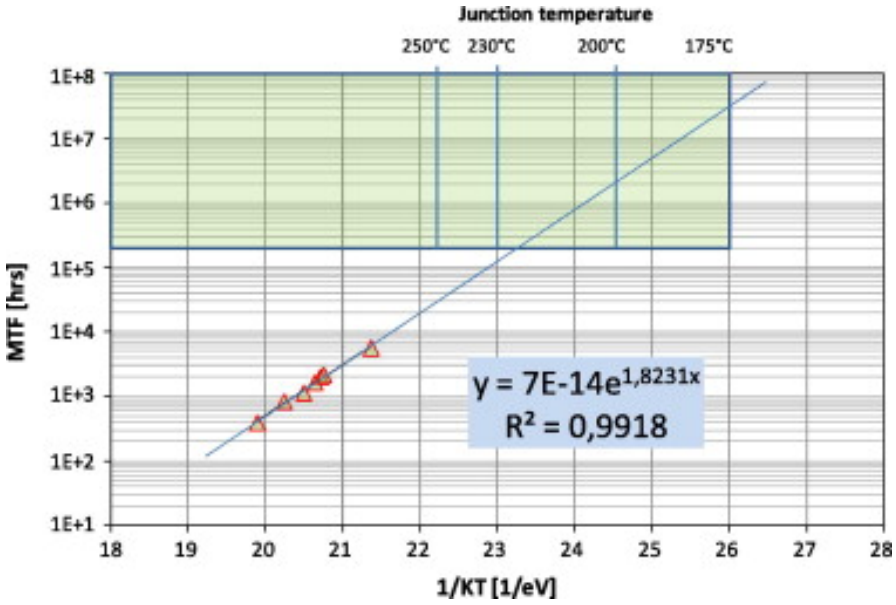

FIGURE 1.1. A sample Arrhenius plot where the data points (red triangles) represent the high temperature tests performed at various temperatures between 270^{o}C and 310^{o}C. Junction temperature represents the peak temperature of the device. The goodness of fit value of R^2=0.9918 indicates the accuracy of the fitting. A life time of 3x10^7 hours was estimated at 175^{o}C by extrapolating from the high temperature measurements, with an associated activation energy of 1.82 eV [21]. Figure from [21][1].

olated to the actual operating temperature of 175^{o}C from Equation 1.1. A sample Arrhenius plot is shown in Figure 1.1 [1], showing an estimated life time of 3x10^7 hours at 175^{o}C, which is extrapolated from the life time .

It is critical to estimate peak channel temperature accurately for reliable lifetime estimations. It is possible to estimate temperature theoretically, by thermal simulations; however, any inaccuracies in the material parameters can result in unreliable predictions. Some of the material data might not be also available, in particular when the new materials concepts are being considered. Therefore, the more accurate approach is to measure channel temperature experimentally. There are numerous temperature measurement techniques employed for semiconductor devices. These can be categorised as electrical, optical and contact techniques:

Electrical techniques exploit temperature dependent device properties, such as ON resistance,

[1] *Reprinted from Microelectronics Reliability, 52(9-10), Lambert, B. et al., Reliability data's of 0.5 μm AlGaN/GaN on SiC technology qualification, 2200-2204, Copyright (2012), with permission from Elsevier.*

gate resistance, leakage current or transconductance [22–24]. Once the temperature dependent relation of the device parameter is extracted from calibration, the device temperature can be estimated. These techniques are non-invasive, fast and practical. They do not require additional characterisation equipment. However, they do not provide any spatial resolution. Measured temperature is averaged through the active area (or along the gate dimensions for gate resistance thermometry), requiring additional device simulations to extract the peak temperature. Since measured temperature is the average over a large area within the device, associated errors are also large when extracting peak temperatures from simulations. Another disadvantage is that each device structure requires calibration.

Optical techniques are advantageous compared to electrical techniques regarding providing spatial resolution. The popular optical temperature measurement techniques are infrared(IR) thermography, Raman thermometry and transient thermoreflectance imaging [2]. Infrared (IR) thermography, based on measuring temperature dependent IR emission, has been the most commonly used thermal imaging tool over the last 50 years and is a very useful qualitative failure analysis technique [25]. However, the spatial resolution of all far field optical measurement techniques is diffraction limited to a maximum of $\approx \lambda/2$, where λ is the wavelength of the light being analyzed. This is a major restriction for IR thermography which is sensitive in the 3-5 μm wavelength range. Besides, transparency of the substrate results in an underestimation of the actual peak temperature [17], making reliable quantitative temperature assessment difficult [17, 25–28].

Micro-Raman thermography, based on probing temperature dependency of phonon frequencies, was developed as a higher spatial resolution alternative and an 0.5 μm resolution and ±1-10 ^{o}C temperature precision has been demonstrated, depending on the illumination wavelength and material under test, respectively [29]. Although this is an established technique in research laboratories, it is a serial point-by-point measurement, requiring long acquisition times to obtain a temperature map. The acquisition times for a single point measurement can vary from seconds

[2] *The overview for the optical and contact thermography techniques presented here were reproduced, from our recent publication, in part with permission from ACS Appl. Electron. Mater. 2, 1, 93–102, Oner, B. et al., Submicrometer Resolution Hyperspectral Quantum Rod Thermal Imaging of Microelectronic Devices, Copyright (2020), American Chemical Society. For this publication, the author designed and conducted the feasibility study, carried out the experiments and the simulations, developed the thermal image reconstruction algorithm, analyzed the data, generated the figures and wrote the manuscript with the assistance from the co-authors.*

to several minutes, depending on the material under test. Microparticle assisted Raman and photoluminescence thermometry along with the scanning thermography have been established to probe surface temperature of microelectronic devices [30, 31], while mapping is time consuming due to single point scanning.

Recently, transient thermoreflectance imaging has emerged for wide field temperature measurements [32–34]. Although the technique can provide submicron spatial resolution (0.3-0.5 μm) thermal images with better than a 1 ^{o}C precision, calibrating the thermo-optic coefficient is a challenge for full field imaging of complex multilayer structures. Besides, a pixel by pixel calibration of each particular test structure is required, which is time consuming.

Contact techniques include atomic force microscopy (AFM) based scanning thermal microscopy (SThM) and micro or nano-particle assisted fluorescence based methods, where the surface of the device and the measurement probe are in physical contact. SThM is among the emerging submicron thermal imaging techniques with its high resolution (≈100s of nm) below the optical diffraction limit [35]. Whilst it offers high spatial resolution, this is an AFM based technique requiring expertise and expensive equipment. The variable tip-to-surface thermal contact resistance depends on the surface topology and poses a challenge for the quantitative thermal mapping of typical electronic device structures which have trenches and step edges. It also requires special thermal designs of cantilever tips to overcome contact resistance related artefacts [36]. Quantification of the effect of topology on SThM is an active area of research [35, 37, 38]. Temperature measurement techniques based on fluorescence imaging have also been established [39–42] and recently the fluorescence intensity ratio of a coating material has been used to measure the thermal image of a PCB [41]. Although the technique can be applied to larger structure, the thick fluorescent paint coating obscures accurate temperature measurement at the device level.

These temperature measurement challenges are a concern not only for the reliability of GaN-based devices, but also for all other microelectronic devices, including future device concepts, channel dimensions of which could go down to nm range. The challenges associated with the existing device thermography techniques call for alternative solutions; the possible solutions would be beneficial for the whole semiconductor industry.

This work focuses on a thermal metrology development for device-level temperature measure-

ments and thermal aspects of GaN-based power devices. **The main motivation** is to address above mentioned challenges by developing a novel thermal metrology tool: a wide field, low cost thermal imaging technique measuring effective surface temperature with sub-micron resolution. A technique based on a combination of high quantum efficiency *quantum rods* and *hyperspectral imaging* has been developed for both steady state and time resolved temperature measurements and demonstrated on a GaN HEMT. In addition to this, thermal bottlenecks of a GaN-on-Si multi-finger power device are identified in an effort to provide a cost-effective solution in terms of thermal management.

Chapter 2 of the thesis discusses theoretical background. operating principle of GaN based devices, the unique properties of quantum rods used as temperature sensors in this work and heat transfer theory are explained. Chapter 3 gives the background information and the details of the experimental techniques used in this work, in order to verify the new metrology and identify thermal bottlenecks of power devices. In Chapter 4, the new steady-state device thermography technique developed in this work, *hyperspectral quantum rod thermal imaging*, is explained in detail and demonstrated on a GaN HEMT. Chapter 5 demonstrates the extension of *hyperspectral quantum rod thermal imaging (HQTI)* for pulse operated devices, enabling time resolved temperature measurements. Thermal bottlenecks of GaN-on-Si multifinger power devices are identified in Chapter 6.

CHAPTER 2

THEORETICAL BACKGROUND

The purpose of this chapter is to give the relevant theoretical background on the materials and the operation of the devices used in this work along with the heat transfer in solids. First, the crystal properties of GaN, a typical AlGaN/GaN device and its operation principle are introduced. The current growth and fabrication technology adopted for commercial GaN based devices along with thermal challenges are briefly discussed. Following this, the unique opto-electronic properties of quantum rods, in particular CdSe/CdS core-shell structures, which makes them suitable for the technique developed in this thesis, are explained. Finally, the heat transport in solids and its application on device self-heating is discussed to provide the necessary background for the device-level thermal analysis.

2.1 GaN based materials and devices

2.1.1 Crystal properties of wurtzite GaN

GaN is a III-V group semiconductor. It can crystallise in both zincblende (also named as cubic or β-GaN) and wurtzite (also named as hexagonal or α-GaN) structure, the latter being thermodynamically more stable due to its lower crystal energy [43] and exhibits larger polarisation [44], making that more suitable for device applications. Numerical studies also showed that wurtzite

structure has higher breakdown voltage [45], which is favorable for high power applications. The wurtzite structure, shown in Figure 2.1, is almost exclusively used for device applications due to these reasons and is the only phase discussed in this study.

The wurtzite lattice shown in Figure 2.1 is characterised by three lattice parameters: a= 3.189 Å, c= 5.185 Å [46], and u= 0.376 Å [47]. This structure is called *non-centrosymmetric* in crystallography, meaning that it lacks symmetry along some or all axes in the lattice. GaN lacks inversion symmetry along c axis. Non-centrosymmetric materials exhibit certain properties, such as polarity and piezoelectrity, which are the properties of GaN exploited for device applications. Wurtzite crystals exhibit a characteristic polarity along c axis as (0001) plane (c plane highlighted in Figure 2.1) is not geometrically equivalent to $(000\bar{1})$. (0001) and $(000\bar{1})$ planes are called Ga-face and N-face, respectively. Although numerical studies suggest that N-face devices have the potential to yield higher output performance due to, for example, better confinement of electrons in the channel [48], the material quality is lower compared to more stable Ga-face structures with the current growth technology, which in practice, yields poorer performance [49]. This is why majority of GaN devices are fabricated on Ga-face, which is the focus in this work.

As the atoms are spaced periodically in crystals, it is useful to use the Fourier transform to study the behaviour of electrons and phonons in order to simplify the mathematical treatment of

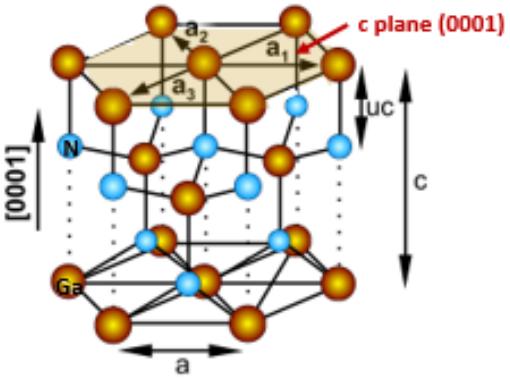

FIGURE 2.1. The wurtzite crystal structure of GaN.Brown and blue spheres represent Ga and N atoms, respectively. Brown highlighted c plane is the common plane of the choice for device fabrication. The crystal is asymmetric along c axis. Figure adopted from [27].

periodic functions, such as periodic potentials seen by electrons. The Fourier transform of the real space of the lattice can be used to construct a new lattice called *the reciprocal lattice*. The Wigner-Seitz primitive unit cell in the reciprocal space is called as *Brillouin zone*, which is a hexagonal prism for wurtzite crystals, as shown in Figure 2.2(a). At the centre of the Brillouin zone, Γ point, the reciprocal lattice vector is equal to zero, $\boldsymbol{k}$=0. The energy band structure of semiconductors are of critical importance for opto-electronic applications. The band structure, i.e. the energy-momentum relation, $E(\boldsymbol{k})$, is calculated by solving *Schrödinger equation*:

$$\frac{-\hbar^2}{2m^*}\nabla^2\Psi(\boldsymbol{r},\boldsymbol{k})+V(\boldsymbol{r})\Psi(\boldsymbol{r},\boldsymbol{k})=E(\boldsymbol{k})\Psi(\boldsymbol{r},\boldsymbol{k}) \tag{2.1}$$

where $\hbar$ is the reduced Planck's constant, m^* is the effective mass,$\Psi(\boldsymbol{r},\boldsymbol{k})$ is the wave function, $V(\boldsymbol{r})$ represents the periodic potential of the crystal. Local density approximation (LDA) [51], linear combination of atomic orbitals (LCAO) [52] and pseudopotential methods [50] are some of the methods to calculate energy band structure. The theoretical band structure of wurtzite GaN, calculated using pseudopotential method [50], is shown in Figure 2.2(b) [1]. Figure 2.2(b) shows that GaN has a direct wide band gap of 3.4 eV at Γ point, where the conduction band

[1] *Reprinted from Journal of Physics and Chemistry of Solids, 32(9), Bloom, S., Band structures of GaN and AlN, 2027-2032, Copyright (1971), with permission from Elsevier.*

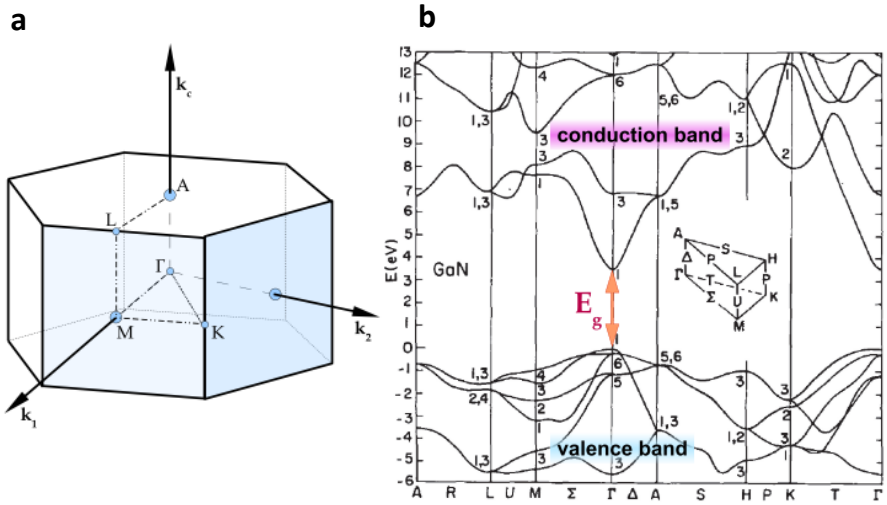

FIGURE 2.2. The first Brillouin zone of the wurtzite GaN and its band structure. (a) First Brillouin zone of a wurtzite crystal, Γ being the centre of the Brioullin zone. Figure adopted from [27]. (b) Theoretical band structure of wurtzite GaN calculated by the pseudopotential method. Figure adopted from [50].

minimum and valance band maximum are observed. The direct wide band gap of GaN makes that a favorable candidate for LED and high power device applications because electron transport from the valance to the conduction band does not require phonon assistance, which is required for the indirect band gap materials, such as Si, to conserve the energy and the momentum simultaneously. This means a higher luminous efficiency for LEDs and lower operating temperatures for high power device applications, translating into energy efficiency and high performance .

GaN can be alloyed to modulate its band gap for device applications. Unlike conventional devices where the channel is in the doped region of a bulk semiconductor, i.e. homojunction, heterojunctions can be formed by combining two materials with different compositions, with a narrower and a wider band gap, in order to increase the device performance by, for example, decreasing impurity scattering. Lattice match of the two materials forming the heterojunction is crucial in order to avoid dislocations which can result in surface states [53]. Modulating the band gap of the material with an acceptable lattice mismatch is possible by creating its ternary alloys. Figure 2.3 shows how the band gap changes with the lattice constant and composition for Group III-nitrides, along with some conventional semiconductor materials. The lattice mismatch of the materials forming the heterojunction, despite being reduced by forming its ternary alloys, results

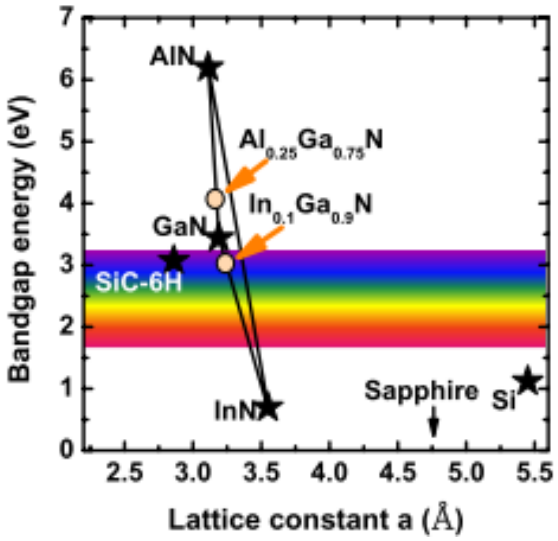

FIGURE 2.3. Band gap and lattice constant of nitrides with various alloying and comparison to common semiconductors. Figure adopted from [27].

in compressive or tensile stress, depending on the composition, when growing the ternary alloy epilayer on top of the base material, for example when growing $Al_xGa_{(1-x)}N$ on top of GaN. These stress effects have important implications on the device performance when the device channel is formed this way, which will be detailed in Section 2.1.2.

2.1.2 Phonons in wurtzite GaN

Vibrational energy states of the atoms described by quantized lattice vibrations, i.e. the quasi-particles called *phonons*, are also important to describe optical processes, such as *Raman scattering*, which was used in this work and will be detailed in Chapter 3, and various scattering mechanisms, for example, electron-phonon scattering, as well as heat transport in the crystal. Lattice vibration in a crystal can be modelled by considering the atoms as if connected to each other with springs, a treatment based on classical mechanics. Phonon frequency-wavevector (ω-$\boldsymbol{k}$) relation, a.k.a. *dispersion relations*, can be obtained from the harmonic oscillator model based on this treatment. For diatomic lattices, as in the case of GaN, phonons are characterised based on their dispersion relation as *optical* and *acoustic* phonons. The calculated phonon dispersion curve for GaN is shown in Figure 2.4 [2], where two branches and a gap in between are observed. The lower branch is the only branch present in monoatomic lattices. In diatomic lattices, the upper branch adds up due to the additional vibrational degrees of freedom contributed by the second atom [55]. Acoustic phonons are the phonons which have the lowest frequency at Γ point in the Brillouin zone. Optical phonons are named so as they can interact more efficiently with light because of their ability to create dipoles within the lattice with their high energies, allowing them to be observed by optical means, as in Raman scattering experiments to be explained in Chapter 3. Group theory predicts eight phonon modes at Γ point : $2A_1+2E_1+2B_1+2E_2$, in a wurtzite crystal [56]. Six of them, i.e. ($A_1+E_1+2B_1+2E_2$), are optical whereas two of them, i.e. (A_1+E_1) are acoustic phonon modes (denoted with green labels in Figure 2.4) [56, 57]. When the atomic vibrations are in the same direction with the translation of the atoms, then those phonon modes are called *longitudinal phonons*. When the vibrations are perpendicular to the translation, then those phonon modes are named as *transverse phonons*. Longitudinal and transverse acoustic/optical

[2] *Reprinted figure with permission from C. Bungaro, K. Rapcewicz, and J. Bernholc, Phys. Rev. B, 61(10), 6720-6725, 2000, doi:10.1103/PhysRevB.61.6720. Copyright (2000) by the American Physical Society.*

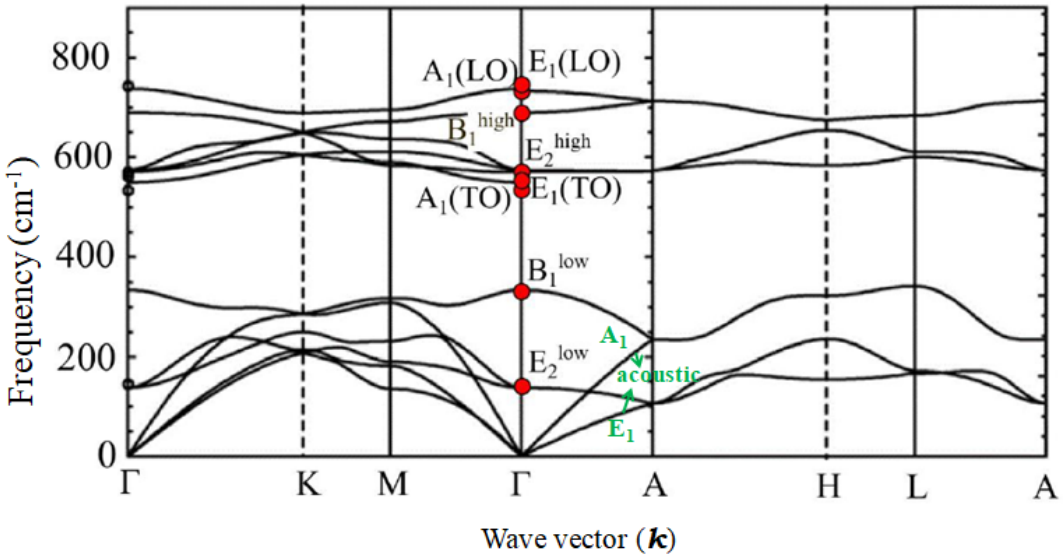

FIGURE 2.4. Phonon dispersion curve of the wurtzite GaN. Figure adopted from [20, 54]. Optical phonon modes are represented by red points on the figure. Acoustic phonon modes are denoted with green arrows and labels.

phonon modes are abbreviated as LA/LO and TA/TO, respectively. The categorisation of phonon modes is useful to predict the outcome of the light scattering experiments, which will be detailed in Chapter 3.

2.1.3 GaN based High Electron Mobility Transistor (HEMT)

A high electron mobility transistor (HEMT) is made of a heterojunction where a quantum well can be created at the interface of a wide band gap and a narrow band gap material forming the junction. GaAs was the first material which was explored to fabricate HEMTs, in the late 1970s [58], by forming the channel with an n-doped AlGaAs, which supplies electrons into the potential well created at the AlGaAs/GaAs interface. The inherent built-in polarisation of GaN, its high electron mobility and high breakdown field paved the way for GaN based high electron mobility transistor, which was first demonstrated in 1993 [10]. These properties and relatively high thermal conductivity of GaN compared to the available Si and GaAs technologies back then attracted attention for high power applications.

The developments in the Si processing technology have allowed Si material to approach its theoretical limits, in terms of voltage blocking capability (30 V/μm[14]) and heat transfer

Table 2.1: Bulk material properties at room temperature for selected semiconductors used for power devices.

	Band gap (eV)	Relative permittivity	Electron mobility ($cmV^{-1}s^{-1}$)	Saturation velocity ($x10^7 cm\ s^{-1}$)	Breakdown field ($MV\ cm^{-1}$)	Thermal conductivity ($Wm^{-1}K^{-1}$)	Substrate diameter (inch)
Si	1.1	11.8	1350	1.0	0.3	150	8-17.7
4H-SiC	3.26	10	700	2.0	3.0	330-450*	8
GaAs	1.42	13.1	8500	1.0	0.6	43	6
GaN	3.4	9.0	1200**	2.5	3.3	130	8
Diamond (C)	5.4	5.5	1900	2.7	5.6	2000	<1

*out of plane-in-plane values, respectively; **2DEG value: 2000 $cmV^{-1}s^{-1}$. Values are based on references [11], [61], [62].

efficiency (a thermal conductivity of 150 W/mK [11, 59]) [14], which are the critical parameters for power electronics applications [14, 59]. Yet, there is an ever growing interest in exploration of other new materials to operate the power conversion systems beyond the limits of Si based devices [14, 59, 60].

Properties of some common semiconductors for device applications are shown in Table 2.1. Table 2.1 hints that diamond is the best material for high power applications with its largest band gap ("ultra wide band gap" in the device terminology) as well as its highest mobility, saturation velocity, breakdown field and thermal conductivity, all of which make this material an attractive candidate for high voltage, high temperature and high frequency operations. However, diamond devices have not yet reached their potential due to fabrication challenges, which is presently the reason of the unacceptable levels of leakage currents [61]. It is also costly compared to competing GaN and SiC power device technologies at the moment [61]. This technology is still under early development phase as evident from the available substrate size (<1 inch) shown in Table 2.1. GaN and SiC technologies are relatively more mature for power applications compared to diamond technology. In fact, currently GaN and SiC are the competing wide band gap technologies [63] and they are now commercially available. The advantage of GaN over SiC is that it can form heterojunctions due to its inherent polarisation, which eliminates the need for doping.

Although several decades of GaN research have allowed this technology to be out of research labs and be in the market now, its thermal performance has not reached its full potential yet

for power applications [16] and thermal optimisation studies are still ongoing. In this work, the newly developed thermography techniques are, therefore, demonstrated on this technologically important material system. Possible thermal bottlenecks of GaN devices for power applications are also investigated in Chapter 6. A brief overview of the GaN HEMT technology, which was used as a platform and thermally investigated in this work, is given in the following sections of this sub-chapter.

2.1.3.1 A typical GaN power HEMT: Polarisation and 2DEG formation

The basis of high electron mobility transistors (HEMTs) is the confinement of electrons in a thin channel at the interface of two dissimilar materials forming the heterojunction due to the potential well formed there. These electrons are free to move parallel to the interface; yet, the motion perpendicular to the interface is restricted. The electrons confined there are named after this restricted motion: *two dimensional electron gas*, shortly 2DEG. As the charge carriers are confined in a thin region at the interface, they are free from electron scattering due to the impurities in the bulk material, increasing the mobility of charge carriers; hence the name "high electron mobility" transistor.

Lateral HEMT structures allow exploitation of inherent polarisation fields of GaN. A typical lateral HEMT structure is shown in Figure 2.5(a). The substrate is usually Si or SiC due to the high cost of bulk GaN substrates [64], which are also available only in small wafer diameters (8 inch) [61]. Most commercial power devices are on Si substrate for its low cost, taking advantage of the already established Si complementary metal-oxide-semiconductor (CMOS) technology. As there is a large lattice mismatch (17% [20]) between Si and GaN, a strain relief layer is grown on a nucleation layer before growing the GaN buffer, which is several microns thick depending on the application. SiC is usually preferred for applications operating at higher power densities, due to its higher thermal conductivity, where the cost is not the primary concern, such as defense applications. The lattice mismatch between SiC and GaN is smaller (3.6% [20]); therefore, a nucleation layer in between them is sufficient for an acceptable interface quality. There is also a growing interest in diamond substrates for better thermal management; yet, it is still an active area of research due to the technological challenges of diamond growth and its integration

as a substrate [65]. The growth of the single crystalline diamond is difficult, which poses a limitation in terms of exploiting its high thermal conductivity because the grain boundaries in the polycrystalline diamond reduce its thermal conductivity [66]. The large lattice mismatch of 11% between GaN and diamond [67] also makes the integration of two materials, without interface defects, challenging [65]. Typically a tens of nanometre thick ($\approx$ 20 nm) [68] AlGaN barrier is grown on top of a several microns thick GaN buffer to form the 2DEG channel. The device is usually passivated with a layer, Si_xN_y or SiO_2, in order to control surface leakage and protect the device from moisture [69]. Ohmic source and drain contacts are formed to allow electrical connection to 2DEG channel, where the electrons flow from the source to the drain. The source is the reference electrode and grounded while a positive voltage is applied to the drain electrode with respect to source (V_{ds}) to enhance the conduction in the channel. A Schottky contact is formed between the gate and the AlGaN barrier, in order to control the current in the channel by modulating the band bending below the gate, which requires a negative gate voltage with respect to source (V_{gs}) to deplete the channel for a normally-ON (*depletion mode: d-mode)* device. The minimum gate voltage required to deplete the channel and turn a d-mode device OFF is called as *threshold voltage*, V_{th}. Source and/or drain contacts can be extended over the channel by the metal plates known as *field plates*, as shown in Figure 2.5(a). The purpose is to shape the

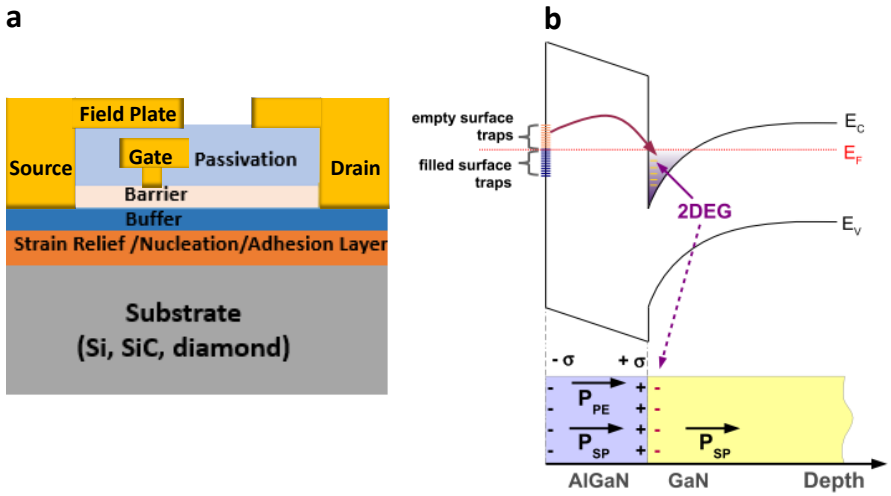

FIGURE 2.5. (a) A typical normally-ON (depletion mode) lateral (GaN) HEMT structure. (b) Band diagram and polarisation fields at the heterojunctions, showing the formation of 2DEG in the GaN and AlGaN interface. Figure adopted from [27].

electric field near the gate, where the peak electric field is observed without the field plates. This structure is useful to increase the breakdown voltage of the device. It also shapes the heating profile by distributing the electric field more uniformly, resulting in a more uniform temperature profile across the channel rather than a concentrated heating near the gate as in the case of its absence. On the other hand, its drawback is the additional capacitance it creates between the gate and the drain and/or gate and the source. This can be a limit for high frequency operations, as in RF. Hence, RF devices are usually designed without them. Field plates are mostly useful for power electronics applications where the breakdown voltage is a more critical parameter than the switching performance. In fact, its use can be considered as a standard for power devices with the current technology. The devices on the same wafer are isolated from each other either by ion implantation such that resistivity of the GaN layer is increased or by mesa etching where the built-in 2DEG is destroyed by etching AlGaN barrier [70].

Group III-nitrides are a special group of compound semiconductors due to their large intrinsic polarisation [68], which is due to the strong ionic bonds causing the displacement of anions and cations. The crystal structure of wurtzite AlN is also very similar to wurtzite GaN, with a larger band gap (6.1 eV), exhibiting even higher intrinsic, a.k.a. *spontaneous*, polarisation than that of GaN [71] in the $[000\bar{1}]$, i.e. towards the substrate. The spontaneous polarisation can build up an electric field of up to 3 MV/cm in III-nitrides [68]. When a tens of nanometre thin AlGaN layer is grown on a few microns thick GaN buffer, the lattice mismatch between these two materials (depending on Al concentration as shown in Figure 2.3) causes tensile stress in the thin AlGaN layer. In this case, GaN is in compression; yet, this compressive stress is usually considered effectively as zero because the thick GaN buffer can relax [72]. The mechanical stress in the AlGaN layer induces an extra polarisation charge in this material, known as *piezoelectric polarisation*. This additional piezoelectric charge can build up an electric field of up to 2 MV/cm [68] in the AlGaN barrier. The magnitude of the polarisation field, and thus the polarisation charge, depends on the lattice mismatch between the AlGaN and GaN layer, which is determined by the Al concentration as shown in Figure 2.3. The directions of both spontaneous and piezoelectric polarisation induced in a Ga-face AlGaN/GaN material system is shown in Figure 2.5(b), along with the band structure. The total polarisation ($\boldsymbol{P}$), which is the sum of both

spontaneous ($\boldsymbol{P_{SP}}$) and piezoelectric polarisation ($\boldsymbol{P_{PE}}$), changes abruptly at the interface as shown in Figure 2.5(b). This sudden polarisation change induces charge accumulation at the surface of the material, which is given for the AlGaN barrier as:

$$\begin{aligned} \sigma &= P_{top} - P_{bottom} \\ &= (P_{SP}(Al_xGa_{1-x}N) + P_{PE}(Al_xGa_{1-x}N)) - P_{SP}(GaN) \end{aligned} \tag{2.2}$$

where σ is the magnitude of the polarisation induced sheet charge density within AlGaN. The sign is +σ at the GaN side; -σ at the free surface of AlGaN. As pointed out before, piezoelectric polarisation in the GaN buffer is neglected due to strain relaxation there.

The charge components in an (undoped) AlGaN/GaN material system include the polarisation charge ($\pm\sigma$) within the AlGaN layer, 2DEG charge density (σ_{2DEG}), charge due to ionised surface states (σ_{surf}) at the AlGaN surface and buffer charge (σ_{buffer}) [73]. Ibbetson *et al.* [73] proposed that charge neutrality in this material system (for an undoped barrier layer) requires that:

$$+\sigma - \sigma - \sigma_{2DEG} + \sigma_{surf} + \sigma_{buffer} = 0 \tag{2.3}$$

Assuming σ_{buffer}=0, which is reasonable for a well-designed HEMT, Equation 2.3 reduces to:

$$+\sigma_{surf} - \sigma_{2DEG} = 0 \tag{2.4}$$

meaning that the ionised surface donors are the source of electrons in the 2DEG. This means that polarisation charge at the interface indirectly, rather than directly, supplies electrons into the channel by attracting electrons from the surface donors into the channel. These surface states are attributed to be due to oxygen impurities in AlGaN layer [74]. This mechanism is depicted in Figure 2.5(b). The energy levels of the surface states needs to reach Fermi level (E_F) to transfer electrons into the channel; if the donor energy is below (E_F), then they do not contribute to the 2DEG charge density. Donor energy can reach E_F if the barrier is thick enough, which enables transfer of electrons of from the surface states leaving behind a positive charge. The minimum barrier thickness for this mechanism is experimentally found to be 3.5 nm (for $Al_{0.35}Ga_{0.65}N$) [73]. It is also possible that there is no surface states due to surface treatment during growth but still 2DEG is present. This can be observed when the AlGaN barrier is thick enough such that the occupied states in the valence band of AlGaN reaches Fermi level and supplies electrons

from AlGaN to GaN [73]. 2DEG depth within the GaN layer is estimated to be 1.6 nm for a vertical electric field of 1 MV/cm in the GaN layer [64], considering the electrons are confined in a triangular potential well at the AlGaN/GaN interface.

2.1.3.2 Enhancement mode (normally-OFF) devices

So far, we have considered a typical normally-ON HEMT which conducts when V_{gs}=0 due to its built-in polarisation and hence the presence of 2DEG channel. Normally-ON HEMTs require a negative gate voltage to lift the conduction band minimum of AlGaN to deplete the channel so that the device is *pinched OFF*. A failure in the gate drivers accompanied by possible unwanted voltage swings on the drain might result in unexpected current flow and eventually circuit failure because, the channel is conductive even when there is no gate voltage in normally-ON devices. In order to minimise such risks, for a fail-safe operation, it is desirable to have normally-OFF (*enhancement mode: e-mode*) devices for power electronics applications, where the transistor is used as a switch, such that there is no conduction when the gate voltage is zero and starts conducting with a positive gate bias. Circuit designers also prefer applying the same sign of electrode voltages for the simplicity of the circuit [75]. These motivations have driven the research efforts for the development and commercialisation of normally-OFF GaN HEMTs since 2000s.

Several approaches have been proposed so far to fabricate normally-OFF GaN devices, such as (i) thinning AlGaN barrier under the gate so that the polarisation charge there is reduced, (ii) fluorine ion implementation below the gate so that negative ions supplied by fluorine depletes the channel (iii) cascode configuration implementation such that the gate of a normally-ON GaN HEMT is driven by the drain voltage of a low voltage normally-OFF Si MOSFET, which is connected in series (iv) p-GaN gate grown on the AlGaN barrier to lift the conduction band minimum [75–77]. Among those the fourth approach, p-GaN gate, is the most promising one due to its ease of fabrication and stability. For example, the precise control of the AlGaN thickness is technologically challenging and thinning AlGaN barrier limits applicable positive voltage [78], and flourine ion implementation was observed to cause unstable threshold voltages [75]. p-GaN HEMTs are now commercially available by suppliers such as Infineon Technologies and Transphorm.

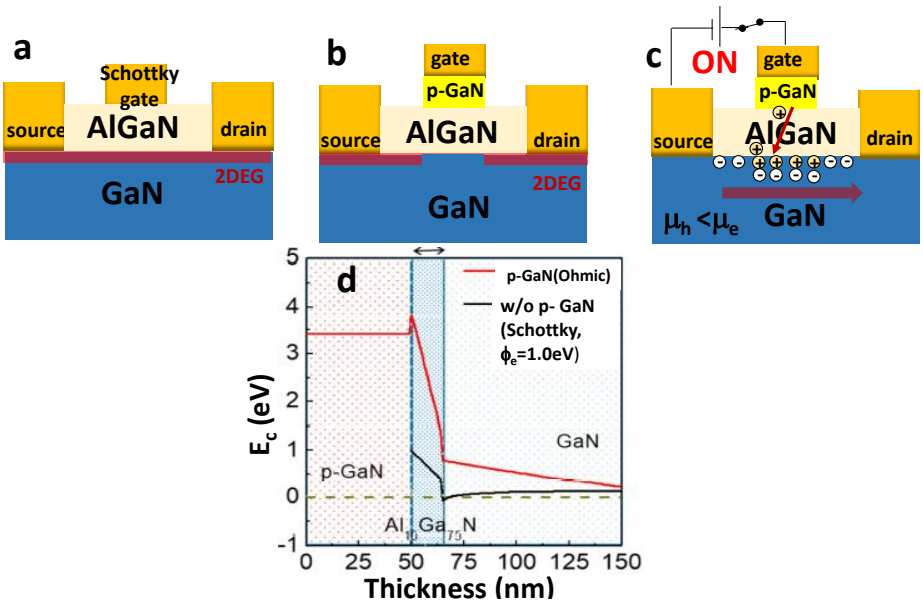

FIGURE 2.6. (a) Channel formation in a typical normally-ON (depletion mode: d-mode) lateral GaN HEMT structure. (b) Channel formation of a normally-OFF (enhancement mode: e-mode) p-GaN HEMT. (c) Operation of a normally-OFF p-GaN HEMT under forward gate bias. (d) Band structure of e-mode vs. d-mode HEMT (Adopted from [76].)

The schematics of a p-GaN gate device and a sample band structure is shown in Figure 2.6 along with a normally-ON HEMT. p-GaN layer lifts the conduction band minimum of AlGaN layer above the Fermi energy so that the channel beneath it is depleted even when no bias is applied on the gate. The depletion of the channel is determined by an interplay with the AlGaN barrier layer thickness and Al concentration as well as the doping concentration of p-GaN. Usually Mg is used for p-typed dopant for GaN [75]. The gate metal of a p-GaN gate can be either Schottky or ohmic, the former being preferred in current devices due to its low gate leakage and threshold voltage because of the higher barrier [76].

The working principle of a p-GaN type normally-OFF device is depicted in Figure 2.6(b)-2.6(c). When the gate bias is below the threshold voltage, the channel below the gate is depleted as shown in Figure 2.6(b). As the gate voltage is increased up to the threshold voltage, the channel starts conducting as the bands bend and the conduction band minimum of the barrier is lowered. We note that p-GaN forms a diode-like structure with the AlGaN barrier beneath it. Therefore, we can consider a forward voltage, which would initiate the injection of holes from p-GaN to the

channel. If the gate voltage is even further increased above the threshold voltage such that it reaches the forward voltage of this diode-like structure, the holes are injected from p-GaN to the channel as shown in Figure 2.6(c). As the charge neutrality needs to be satisfied, electrons are injected from the source. These electrons move to the drain under high drain bias. The holes stay around the gate as hole mobility is lower than the electron mobility. This mechanism enhances the output of the device. Normally-OFF operation based on this mechanism was first demonstrated in 2007 by Uemoto et al. [78]. They used p-AlGaN gate and named their structure as "gate injection transistor (GIT)" due to hole injection from the gate. The industry then adopted p-GaN approach described here due to better depletion [75], reducing power consumption and switching more efficiently. In this work, mainly p-GaN power HEMTs supplied by Infineon Technologies were used as the test structures.

2.1.3.3 Substrates and strain relief layer

We have briefly discussed in Section 2.1.3.1 that the lack of cost effective bulk GaN substrates led the device community to seek for alternative substrates, such as Si, SiC and recently diamond, which is, as discussed, not commercially available and early in the R&D phase. An ideal substrate should (i) be available in large wafer diameters so that the fabrication cost is reduced, (ii) have a small lattice and coefficient of thermal expansion (CTE) mismatch with the GaN buffer to reduce the dislocations at the interface due to strain, which might, otherwise, severely affect the electrical performance (such as causing leakage currents by punch-through effects and buffer trapping [79]), (iii) have high dielectric strength to prevent vertical breakdown, (iv) have high thermal conductivity for a better thermal management.

Application of the end-user is critical for the choice of the "ideal" substrate as there is no substrate which simultaneously satisfies all four criteria listed above; therefore, the trade-offs need to be considered depending on the application. The application range can be broadly categorised as RF vs. power electronics. RF devices are used for signal amplification for which a weak RF input signal applied to the gate, $v_{gs}(t)$, is amplified at the drain terminal which gives the output, $v_{ds}(t)$. RF operating range is usually in the GHz regime. On the other hand, HEMTs are used as a switch for power electronics applications. The switch is turned ON and

OFF by modulating the gate bias (OFF when $V_{gs} < V_{th}$, ON otherwise). Power devices usually operate in the MHz regime. This implies that RF and power devices differ in their design due to different frequency response requirements. For example, RF devices have shorter channel length ($\approx$ 1-2 μm) for high frequency response, meaning that they have a smaller footprint than power devices which have larger channel widths of $\approx$ 10s of μm and lengths up to $\approx$ mm such that it can withstand high powers. This means that GaN based RF devices operate at higher power densities (typically $\approx$ 5-10 W/mm) whereas those for power applications operate at high powers (less than 1 W/mm), which differentiates the thermal management requirements and thus the choice of the substrate for these two applications. The targetted end use for RF devices is defense or aerospace whereas GaN power HEMTs are projected to replace Si transistors in the customer market. Therefore, cost restrictions on the design are more stringent for power HEMTs and is the most critical factor for the substrate choice for power devices while the high performance is the determining factor for RF HEMTs. These considerations for RF and power applications determine the substrate choice.

During the early development phase of GaN HEMTs in the late 1990s and early 2000s, mostly sapphire substrates were used as it was inexpensive. Yet, there is a large lattice mismatch of 16% between sapphire and GaN [80], similar to that of Si (17%). It has a comparable dielectric strength with that of Si [80]; however, has a very low room temperature thermal conductivity of $\approx$30 W/mK [80], which is almost one third of Si thermal conductivity. This low thermal conductivity has limited its use as a substrate. Sapphire is now mostly used for early development phase in academic research labs. It does not have any use in the GaN market, neither for RF or power HEMTs.

Current devices in the market are grown on either SiC or Si substrates, diamond substrate being an active research topic currently far from commercialisation as discussed. As discussed in Section 2.1.3.1, SiC has excellent thermal conductivity and breakdown field (See Table 2.1), outperforming Si. It has also a better lattice match with GaN than that of Si. Yet, as pointed out previously, its high cost is a limitation, especially for power devices where the devices have large footprints and the market is cost competitive. It is mostly preferred for RF applications, where the power densities are high and the device sizes are small.

Si is the most attractive candidate for substrate material for customer market applications, despite its lower thermal conductivity and larger lattice mismatch with GaN. Si CMOS fabs are already well established and its integration with GaN-based technologies would be cost effective. Si wafers are also available in larger diameters (See Table 2.1), making the technology scalable. Yet, the challenge is its large lattice and CTE mismatch with GaN, making stress management between these two layers difficult. As in SiC substrates, typically an AlN layer is grown on the Si substrate for growth initiation [16] and to prevent the chemical reaction between Ga and Si, known as *melt-back* [81]. A strain relief layer (SRL) is grown on the AlN nucleation layer, which relaxes the tensile stress stress in GaN, which has a larger CTE than Si (CTE of GaN=5.5x10^{-6} K^{-1}; CTE of Si=2.6 x10^{-6} K^{-1} [82]). Two common successful solutions for SRL are the step-graded AlGaN layer, where the Al concentration is decreased towards the GaN channel, and an AlN/GaN superlattice, which consists of alternating thin layers (on the order of several nm) of AlN and GaN layers. The detailed structure of SRLs designed and grown by commercial manufacturers is usually confidential.

From thermal performance point of view, it is important to understand the effect of the SRL on the heat transport in the device. When the heat is transferred between dissimilar materials, the boundary in between them sets a barrier to heat transfer due to reflection of phonons at the interface, which originates from different densities and sound speeds at the different sides of the interface, known as *acoustic impedance mismatch* [83]. This phenomenon causes a *thermal boundary resistance (TBR)* at the interface and will be discussed in more detail in Chapter 2.3. TBR between GaN and substrate has been shown to be significant for RF devices [84]. Yet, this might or might not be applicable to power devices, where the device geometry is different. It is equally important to understand whether or when TBR of SRL is a significant factor for the heat transport in power devices. In Chapter 6, the effect of epitaxial layers on the thermal performance of large area power devices, including TBR, is investigated.

2.1.3.4 Device characteristics and operation

The output characteristics, I_{ds}-V_{ds} relation, of a normally-ON GaN HEMT are shown in Figure 2.7(a). When a positive drain voltage with respect to source is applied on the drain electrode, the

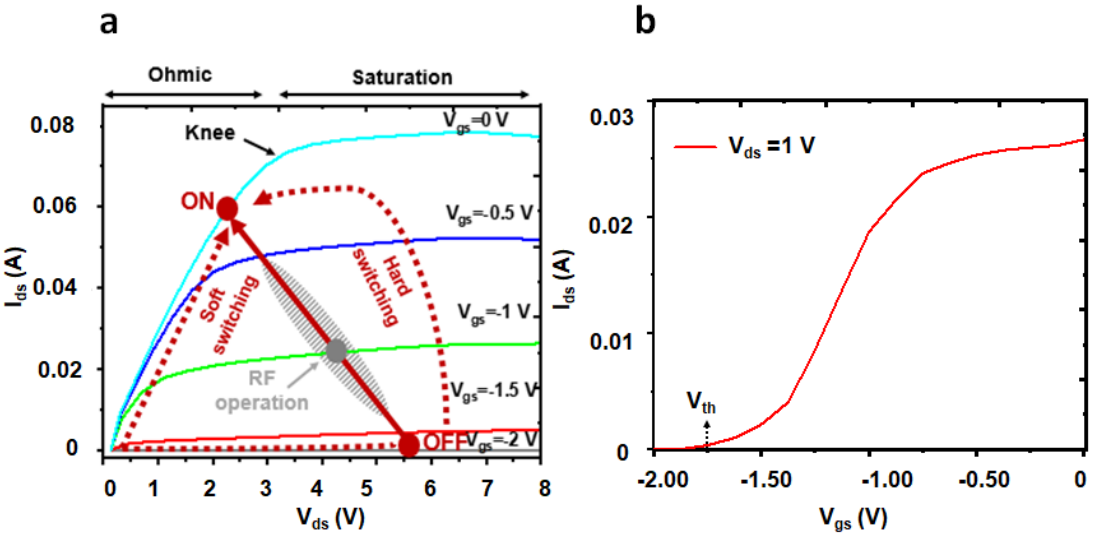

FIGURE 2.7. (a) Output characteristics of a normally-ON HEMT. Maroon lines show a typical operation of a power HEMT (dashed lines indicating the switching path); light gray shaded region shows RF operation point. Conversely, for a normally-OFF device, when V_{gs}=0, no current flows between the drain and source electrodes and a positive gate voltage with respect to the source electrode (V_{gs}>0) is applied to turn the device ON. (b) Transfer characteristics of a normally-ON HEMT.

current starts flowing from the source to the drain. There is a linear relationship between the drain bias, V_{ds}, and the current flowing from source to drain, I_{ds}, up to a certain drain voltage as depicted in Figure 2.7(a). The region where this relation holds is called *ohmic or linear region*, where V_{ds}<V_{knee}. In the ohmic region, the electron velocity, v, is linearly proportional to the electric field, E, between the drain and the source:

$$v = \mu E \tag{2.5}$$

where μ is the mobility of the electrons in the 2DEG and constant in the ohmic region. If the drain voltage is increased further, mobility starts decreasing due to self-heating, i.e. phonon population increases and the electron-phonon scattering becomes a significant factor. In the *knee region*, at V_{knee} , the linear relationship given in Equation 2.5 is no longer valid due to the decreased 2DEG mobility. If the drain bias is increased beyond V_{knee}, the current between the source and the drain stops increasing and reaches a plateau, which is called the *saturation region*.

The operating regimes for power and RF applications are shown in Figure 2.7(a). HEMTs for power switching applications are operated between the pinched-OFF point (negative V_{gs} for

d-mode (normally-ON) devices, V_{gs}=0 (or positive below V_{th}) for e-mode (normally-OFF) devices) and the ohmic region, as shown with the maroon line in Figure 2.7(a). The device can be turned ON in two ways: (i) through the high electric field and high current region, which is called *hard switching* or (ii) through the zero point, V_{ds}=0, which is known as *soft switching*. For RF applications, since the goal is to amplify the signal through the gate voltage, the device can be operated somewhere along the marroon line in Figure 2.7(a), which is called the *load line*. The region where the device operates along the load line defines the class of the operation. The shaded gray region in Figure 2.7(a), for example, shows the class A operation [27], which is in the middle of the load line and where the device always conducts. It can be operated at the pinched-OFF state shown in Figure 2.7(a) either, which is called the class B operation, where the DC bias on the gate is zero. Class B operation is more energy efficient due to negligible heating; however, the transistor conducts only during the half-wave of the sinusoidal signal imposed on it due to the absence of DC voltage.

Figure 2.7(b) shows the transfer, I_{ds}-V_{gs}, characteristics of a normally-ON GaN HEMT. The threshold voltage at which the channel starts conducting is also labeled on Figure 2.7(b). The derivative of this curve gives the transconductance:

$$g_m = \frac{dI_{ds}}{dV_{gs}} \tag{2.6}$$

which determines the effectiveness of the gate for depleting the channel. Transconductance is an important performance parameter for RF applications, the higher being the better.

2.1.4 Growth methods

Molecular Beam Epitaxy (MBE) and Metal Organic Chemical Vapor Deposition (MOCVD) are the two common methods to grow high quality GaN epitaxially. In MBE, elemental sources are evaporated and directed onto a heated (up to $\approx 700^o$C [64]) substrate on which it can react with other sources. MBE takes place in a ultra high vacuum (UHV) environment where the pressure in the chamber is reduced down to $\approx 10^{-9}$ Torr so that the evaporated beam in the chamber has long enough mean free paths and can form pure layers on the substrate. For GaN growth, elemental Ga source evaporated in a Knudsen cell is directed onto the substrate (after growing

AlN nucleation layer and SRL, considering Si substrate as discussed in Section 2.1.2.3) where it can react with a nitrogen source [20].

MOCVD makes use of metal-organic sources, instead of elemental ones [85]. Multiple organic sources are directed onto a heated substrate, temperature of which can reach up to 1000^oC, where they can react. MOCVD takes place in a moderate pressure environment, typically at 15 to 750 Torr [85]. These moderate pressure levels are to ensure the unintentional doping of GaN is as low as possible, for example due to the oxygen impurities. For the growth of GaN buffer, or GaN channel, tri-methyl-gallium ($Ga(CH_3)_3$) and ammonia (NH_3) sources are directed on the SRL (on Si) and forms GaN as a result of the reaction:

$$Ga(CH_3)_3 + NH_3 \rightarrow GaN + 3CH_4 \tag{2.7}$$

The byproduct methane, CH_4, is volatile and evaporates quickly [20].

The choice of the ideal growth technique depends on the production volume, material to be grown and overhead costs. The decision making criteria involve many parameters, from cost concerns to risk mitigation which is determined by the production volume [85]. Nevertheless, the industry seems to prefer MOCVD due to its higher growth rate and scalability.

2.2 Temperature dependent photoluminescence of quantum rods (QRs)

2.2.1 Size effects in low dimensional systems

Since the advances in monolayer fabrication techniques, such as MBE, in the late 1980s, the interest in low dimensional systems has increased [86]. Low dimensional systems refer to materials/material systems where the particle motion is restricted in one or more directions. For example, the quantum well at the AlGaN/GaN interface, which we discussed in Section 2.1, is also a low dimensional system as it restricts electron motion in the vertical direction and creates a 2DEG. Other low dimensional systems such as quantum wires restrict the motion in 2 dimensions and create a 1 dimensional (1-D) confinement; quantum dots restrict the motion in 3-D and create a 0-D system where the particles (electrons and holes in this context) are localized.

The dimensions of these structures are on the order of several nm. On this length scale, especially in the 3-D confinement regime, the optical properties of the materials diverge from their bulk values. This is due to the *quantum confinement effect*. Quantum confinement effects become dominant once the additional kinetic energy of the particle due to confinement is comparable or greater than its kinetic energy due to thermal motion [87]. If we consider a particle confined in a region along x axis with length Δx, the uncertainty in its momentum, Δp_x, given by Heisenberg uncertainty principle, is equal to:

$$\Delta p_x = \frac{\hbar}{\Delta x} \tag{2.8}$$

For a particle with mass m, the confinement in this direction adds that an additional energy of:

$$E_{confinement} = \frac{(\Delta p_x)^2}{2m} \sim \frac{\hbar}{2m(\Delta x)^2} \tag{2.9}$$

Confinement energy being greater than the thermal energy of the electron requires that:

$$E_{confinement} \sim \frac{\hbar}{2m(\Delta x)^2} > \frac{1}{2} k_B T \tag{2.10}$$

where k_B and T are the Boltzmann constant and temperature of the crystal, respectively. This means that the size effects are important if:

$$\Delta x \sim \sqrt{\frac{\hbar^2}{m k_B T}}\,. \tag{2.11}$$

In other words, Δx, the confinement dimension, needs to be on the same order with the de Broglie wavelength of λ_{deB}=p_x/h. For example, for GaN with an effective electron mass of m^*=0.20m_o, the quantum size effects are observed if Δx $\sim<$ 3.5 nm at room temperature.

Quantum dots, forming 0-D systems, are spherical nanoparticles with 2-10 nm diameters. Their elongated versions, quantum rods (QRs), are typically 1-100 nm in length and 1-10 nm in diameter. The energy states are quantized in 3D in these small structures. These energy states can be approximated by a potential well model which is confined in all three directions with infinite barriers, analogous to the standard "particle in a box" problem in quantum mechanics. The energy states can be obtained by solving the Schrödinger equation (Equation 2.1) in Cartesian coordinates. The boundary conditions for this potential well are then given as:

$$\begin{aligned} V &= 0, \qquad -d/2 < (x,y,z) < d/2 \\ V &= \infty, \qquad elsewhere \end{aligned} \tag{2.12}$$

considering (x, y, z)=(0,0,0) at the centre of the well, and d is the thickness of the rectangular quantum well. Solving Equation 2.1 subjected to the boundary conditions given by Equation 2.12 , the energy states that correspond to n^{th} level can be obtained as [87]:

$$E(n_x, n_y, n_z) = \frac{\pi^2 \hbar^2}{2m^*} \left(\frac{n_x^2}{d_x^2} + \frac{n_y^2}{d_y^2} + \frac{n_y^2}{d_y^2} \right) \tag{2.13}$$

where n_x, n_y, n_z represent the quantized levels in x, y, z directions, respectively. Similarly, quantum dot (or rod) dimensions in three dimension are given by d_x, d_y and d_z. Equation 2.13 indicates that the energy spectrum of quantum dots (or rods) is discrete, similar to that of atoms. This is why quantum dots (or rods) are also referred as *artificial atoms*. This equation also shows that the energy spectrum of these 0-D structures can be tuned by changing the particle size, unlike atoms. The tunability of the energy states makes these structures highly versatile for optical sensing and opto-electronic applications.

2.2.2 Fabrication techniques and morphology of quantum rods

Quantum rods (or dots) can be fabricated by lithographic techniques or grown by MBE or MOCVD [88, 89]. Their colloidal synthesis is also possible and was first demonstrated in 1993 by Murray et al. [90, 91]. Colloidal synthesis is more practical and scalable compared to complicated and expensive growth and lithographic techniques, and is capable of providing a size dispersion of down to 5% [90]. Colloidal quantum rods are also commercially available with various nanoparticle dimensions. Quantum rods/dots can be made of a single semiconductor or a combination of semiconductor materials, one encircling the other. The former is known as *core-type quantum dot*; the latter is named as *core-and-shell-type quantum dot*. The purpose of the core and shell structure is to improve the optical properties, for which these nanoparticles are attractive. The wider band gap shell surrounding the narrower band gap core improves the emission efficiency, by passivating the surface states [92, 93]. The shell can also be protective against the photooxidation of the core [94]. A schematic cross-section of a core-and shell-type quantum dot (top) and side view of a quantum rod (bottom) is shown in Figure 2.8, along with a schematic of the band structure showing quantized energy levels. Figure 2.8(a) shows ligands, which are organic compounds, attached to the outer surface of the quantum dots. Ligands determine the inter-particle distance

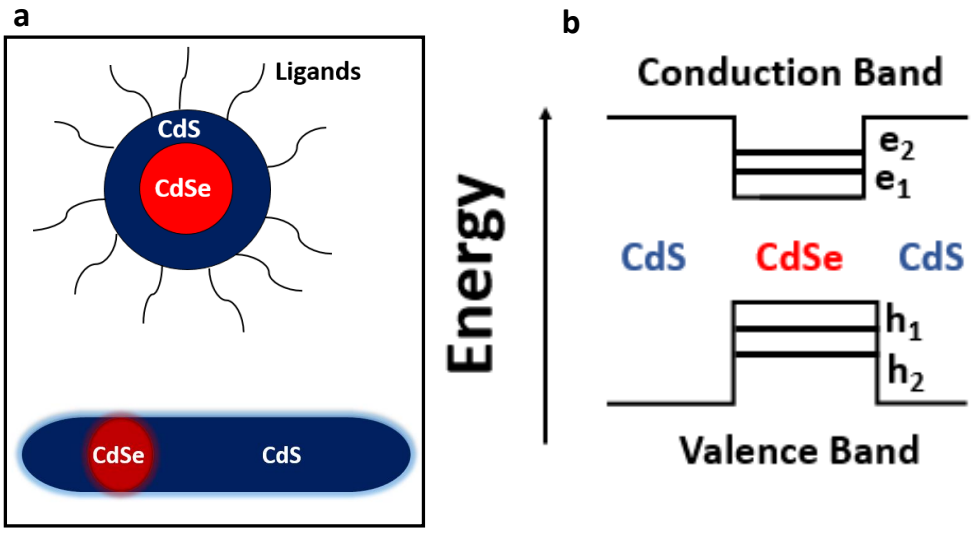

FIGURE 2.8. (a) Schematic of cross-section of a core (CdSe)-and-shell (CdS) quantum dot (top) and a side of a quantum rod. (b) Schematic of a quantized energy levels in a quantum dot/rod heterostructure.

in the colloidal solutions, which is an important aspect for its optical properties [95], for example in terms of determining ensemble sizes. In this work, commercial colloidal CdSe/CdS core-and-shell-type quantum rods in hexane solution was used as temperature sensors, due to their high quantum efficiency (QE), namely luminescent efficiency for low dimensional systems, of 60%.

2.2.3 Photoluminescence

Light absorption by a pure and defect-free semiconductor solid is only possible if the energy of the light with frequency ω_i is greater than the band gap energy of the material, E_g, that is $\hbar\omega_i > E_g$. Upon absorption, an electron in the valence band of the semiconductor is excited to the conduction band, leaving behind a hole, meaning that an *electron-hole pair* is created. Electron promoted to the excited state can relax back to the ground state either by (i) emitting a photon, i.e. *radiatively*, or (ii) transferring its energy to a phonon, thereby generating heat, or to impurities or defects called *traps*, i.e.*non-radiatively*. Re-emission of light after photon absorption, i.e. radiative relaxation, is called *photoluminescence*. Radiative transition rate from the excited state to the ground state depends on the electron population in the upper level, N at time t and is determined

by the Einstein coefficient A [87]:

$$\left(\frac{dN}{dt}\right)_{radiative} = -AN. \tag{2.14}$$

Solution of this differential equation for N gives:

$$\begin{aligned} N(t) &= N(0)exp(-At) \\ &= N(0)exp(-t/\tau_R) \end{aligned} \tag{2.15}$$

where τ_R=A^{-1} is the *radiative lifetime* of the electron-hole recombination. The materials with higher absorption coefficients have higher emission probabilities, and thus shorter radiation lifetimes. Electrons excited to the higher states of the conduction band first relax, by phonon emission, to the lowest levels of the conduction band where they form a thermal distribution such that their energy is within $\sim k_BT$ of the bottom of the conduction band [87]. The holes follow the similar process in the valence band. The light is emitted when these electron-hole pairs recombine radiatively; hence, the emitted light spectrum is dispersed by a narrow energy. This process is depicted in Figure 2.9, where the broadening of the emission spectrum around the peak emission energy, $\hbar\omega_R$, is labeled by Γ. We note that this broadening is not only due to thermal distribution of the carriers, but can be also instrument related, i.e. due to the spectral resolution of the measurement equipment. We also note that energy conservation requires that the energy of the emitted photon ($\hbar\omega_R$) in the form of photoluminescence is smaller than the incoming photon energy ($\hbar\omega_i$) due to the energy transfer to the lattice.

Non-radiative recombination process, with a relaxation rate of τ_{NR}, is also depicted in Figure 2.9. The luminescent efficiency of the relaxation process, η_R, can be calculated as [87]:

$$\left(\frac{dN}{dt}\right)_{total} = -A\left(\frac{1}{\tau_R} + \frac{1}{\tau_{NR}}\right) \tag{2.16}$$

As η_R is given by the ration of the radiative recombination rate to the total relaxation rate, i.e. ratio of the right hand side in Equation 2.14 to that of in in Equation 2.16, we can obtain:

$$\eta_R = \frac{1}{1+\tau_R\tau_{NR}} \tag{2.17}$$

, which indicates that high luminescent efficiency is obtained with shorter radiative lifetimes. Radiative lifetimes need to be considered for time resolved photoluminescence measurements (Chapter 5).

The basic mechanism of photoluminescence in low dimensional systems, i.e. quantum rods which are of interest in this work, is the same as in bulk solids which is discussed above. However, the selection rules for low dimensional systems require that the electron and hole be in the same energy levels [87], within their respective bands, for the transition to occur:

$$\Delta n = 0 \tag{2.18}$$

, which is depicted in the left hand side of Figure 2.9. For QRs, the minimum photon energy required to create an electron-hole pair is equal to:

$$\hbar\omega_{i,min} = E_g + E_{h1} + E_{e1} \tag{2.19}$$

where E_g is the band gap energy of the bulk material that the QR is made of, E_{h1} and E_{e1} are minimums of the quantized energy levels in the valence and conduction bands, respectively, as shown in Figure 2.9. This result also indicates that the optical absorption edge of the quantum

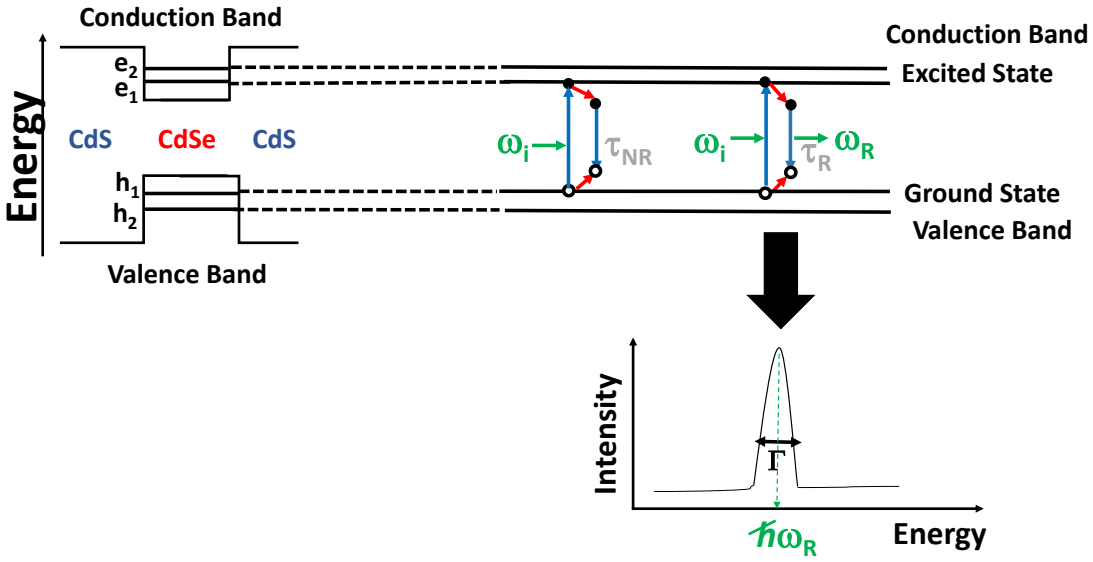

FIGURE 2.9. Schematics showing possible relaxation mechanisms of an electron-hole pair in quantum rods: Non-radiative (energy transferred to a phonon) vs. radiative (energy released as a photon: photoluminescence (PL)). Schematic of a sample PL spectrum shows the dispersion around the peak photon energy, $\hbar\,\omega_R$ due to thermal and instrumental broadening.

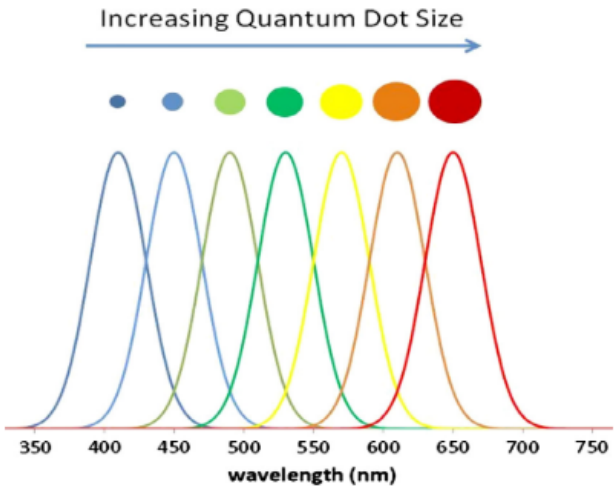

FIGURE 2.10. Red shift in the photoluminescence emission peak with the increase in quantum dot size. Figure from [96].

rods shifts to a higher value compared to its bulk value. By tuning the size of the quantum well, one can modify the optical absorption edge, and thus the peak energy of the photoluminescence spectrum. This is illustrated in Figure 2.10 [3], which shows a red shift in the emission wavelength (corresponding to lower photon energy and smaller band gap) with the increasing quantum dot size. Another advantage of quantum rods, other than tuneable optical properties, is the increased luminescent efficiencies, a.k.a quantum efficiency in this context, compared to its bulk values. This is because of the increased Coulomb attractions between electron-hole pairs, due to small dimensions of the QRs. Increased Coulomb attractions increase the emission probability and shorten radiative lifetimes. As the energy levels of the quantum rods are atom-like, i.e. discrete, the thermal broadening of the spectrum is also reduced. This translates into sharper emission lines and colour purity, which are desirable properties for optical sensing and lighting applications.

2.2.4 Quantum rods as temperature sensors

In this work, quantum rods are used as a thermal sensors, exploiting their useful optical properties such as high quantum efficiency and small sizes which allow probing the surface temperature

[3] *Reprinted from Journal of Alloys and Compounds, 636, Vasudevan, D. et al., Core–shell quantum dots: Properties and applications, 395-404, Copyright (2015), with permission from Elsevier.*

of the device on which they are deposited. Quantum rods, or dots, are available commercially with a 450-620 nm maximum emission wavelength. We probed their temperature dependent photoluminescence response to measure the temperature on the surface that they are deposited. Photoluminescence thermography measures the band gap change with temperature. An emprical equation relating the band gap and temperature was given by Varshni in 1967 [97]:

$$E_g(T) = E_0 + \frac{\alpha T^2}{(T+\beta)} \tag{2.20}$$

where E_0 is the band gap at 0 K, α and β are material dependent constants, which are determined experimentally. Although this equation is known to give inaccurate results at cyrogenic temperatures, it is still valid for temperature ranges above room temperature.

2.3 Heat conduction in solids

Heat conduction in solids is critical in the design and performance analysis of microelectronic devices. The primary heat carriers are phonons in semiconductors and insulators; electrons in metals. *Fourier heat diffusion law* describes the heat transfer in solids when:

• the time scales of interest are longer than the relaxation time (τ), which is the average time interval between successive collisions of the heat carriers and is on the order of 10^{-12}-10^{-10} s in many materials [98], and

• the characteristics length of the material is larger than the mean free path of the heat carriers (Λ), which is the average distance traveled between successive collisions of the heat carriers, on the order of ~ 10 nm [32].

The time scales, in the MHz operating regime, and characteristic dimensions of power devices, on the order of μm, considered in this work fall within the diffusion regime where Fourier law is valid. The general form of Fourier law is given by:

$$\rho C_p \frac{\partial T}{\partial t} - \nabla \cdot (k \nabla T) = \dot{q_v} \tag{2.21}$$

where ρ is the density, C_p is the specific heat at constant pressure, k is the thermal conductivity of the solid and $q_v^{\cdot}$ is the volumetric heat generation within the medium. Under steady state, the first term in Equation 2.21 drops and the temperature field of the medium is given by:

$$-\nabla \cdot (k \nabla T) = q_v^{\cdot} \tag{2.22}$$

The thermal conductivity term, k, in Equations 2.21-2.22 denotes how easy the phonon transport is within the solid when subjected to a temperature gradient. If phonons are thought to be moving randomly in space as a *phonon gas*, then the ideas from *kinetic theory of gases* can be applied to describe their motion [98, 99]. Adopting kinetic theory for phonon transport, thermal conductivity of a solid can be estimated as [98, 99]:

$$k = \frac{1}{3} C_v v \Lambda \tag{2.23}$$

where C_v and v are the specific heat per unit volume and average random velocity of heat carriers, which are primarily phonons for semiconductors, i.e. speed of sound, respectively. The scattering of phonons in the material determines the magnitude of mean free path, Λ, in Equation 2.23, which is material and temperature dependent. The phonon scattering mechanisms can include defect or impurity scattering, boundary (or interface) scattering and intrinsic scattering.

Defects or impurities cause phonon scattering by changing the local phonon velocity. The extend to which they affect the heat transport is proportional to their concentration and temperature. For example, impurity scattering, which can be considered for dopants in the GaN buffer in a HEMT structure, can be an important mechanism at high temperatures and reduce thermal conductivity [99].

Interface scattering mechanism represents itself as *thermal boundary resistance (TBR)* in the heat transport, as briefly introduced by the end of Section 2.1.3.3 and equals heat flux divided by the temperature difference across the interface. TBR is observed as a result of phonon reflection at the interface between two materials, which reduces the number of transmitted heat carriers. There are two models to predict phonon reflection and transmission at the interface: acoustic mismatch model (AMM) and diffuse mismatch model (DMM) [100, 101]. The former assumes no scattering, i.e. the incoming phonon is either specularly reflected or transmitted. The latter is considered when the surface roughness is comparable to (or larger than) phonon wavelength

and the incoming phonon is diffusely scattered. These two models set the upper and lower limits of the thermal boundary resistance values in real systems; yet, neither exactly fits with the experimental observations [83]. In practical systems, such as GaN-on-Si devices including a thin strain relief layer in between GaN and the substrate, TBR and the contribution of interlayer to the thermal resistance are lumped into a single parameter, known as *effective thermal boundary resistance,* TBR_{eff} [101], which simplifies the analysis of the heteroepitaxial systems.

The intrinsic scattering mechanism is observed even in a perfect crystal. This mechanism is also known as *phonon-phonon scattering*, which is due to the anharmonic interatomic potential between the atoms. This mechanism is known to be dominant at high temperatures [99]. This is because phonon densities are high at high temperatures, which increases the scattering rates. Phonon-phonon scattering occurs by, what is called as, *three-phonon scattering process* [98]. In three-phonon scattering mechanism either two phonons merge into a third phonon or a single phonon splits into two phonons. Considering the mechanism where two phonons merge into a single phonon, the total energy is conserved during this process; however, the momentum, which can be considered in terms of phonon wavevectors, may or may not be conserved. The process in which both phonon energy and momentum are conserved is known as *normal process (N-process)* whereas the one when momentum is not conserved is named as *umklapp process (U-process)*. N-process does not directly contribute to thermal conductivity of the crystal as the total phonon flow is seemingly unchanged. U-process is observed if the sum of wavevectors of the two incoming phonons falls outside the first Brillouin zone and the merged phonon is pushed back to the Brillouin zone, resulting in a momentum change. The direction change in phonon transport creates a resistance in the heat flow. This process is the main mechanism which decreases thermal conductivity at high temperatures as more phonons are excited near the Brillouin zone at high temperatures. Although N-process does not directly contribute to thermal conductivity, it can enhance U-process by creating a more strongly scattered phonon. Since phonon-phonon scattering is the dominant mechanism at high temperatures, thermal conductivity is inversely proportional to temperature:

$$k \propto \frac{1}{T^n} \tag{2.24}$$

where often n=1-1.5 [98].

We note that, in this work, nanostructures, namely quantum rods, forming a thin coating layer on the test sample are used as surface temperature sensors. For such cases, the validity of Fourier law might be questioned as the size of mean free path of phonons can be comparable or larger than the characteristic dimension of the nanoparticles and a local temperature gradient might not be established. However, as long as the domain of interest is larger than the characteristic length of the nanoparticles, Fourier law can still give a good approximation for heat transport when size dependent thermal conductivity values are implemented [102].

Thermal-only device modelling, based only on Fourier heat diffusion equation, requires the assumption of the shape of the heat generation region in the system. The heat generation in the device is due to the Joule heating in the device channel and an assumption is made for the shape of this Joule heating profile at the start of the analysis in the thermal-only modelling. Heat generation profile can be predicted in electro-thermal device modelling by solving drift-diffusion equations. However, electro-thermal models come with a computational cost. Therefore, a thermal-only model is usually more practical and sufficient when the heat generation region assumption can be validated by the experiments. Once the assumption of the heat generation profile is validated with the experiments, then the thermal-only model can be extrapolated for other scenarios of interest and further analysis of the device, for example to extract the peak channel temperature, which is of interest for the life time estimations as discussed in Chapter 1 and yet is not directly measurable with the available techniques. Therefore, it is critical that heat profile is estimated from the experiments to predict the temperature field of the device accurately when using thermal-only models for device simulations.

The boundary conditions imposed can be constant temperature (*Dirichlet*), constant heat flux (*Neumann*), mixed type (*Robin*, including convection terms) or periodic if the system is symmetric. The partial different equations given by Equation 2.21-2.22 are challenging to solve analytically for 3-D complex transistor structures. Therefore, the standard practice is to use commercial finite element based simulations to extract channel temperature from the simulations. The finite element method (FEM) is a numerical technique which can solve partial differential equations by discretising the space of interest by *meshes* which are connected to each other by *nodes*. The

partial differential equation reduces to algebraic equations, which are easier to solve, at each of these *finite elements*, which are bounded by the nodes of the meshes. The nodes of the adjacent meshes need to satisfy the same boundary condition for continuity.

The meshing is critical when using FEM because the unknown quantity estimated at the nodes are interpolated at the elements. If the nodes are closely spaced, then the accuracy of the solution is higher (less interpolation) at the cost of computational time, as the total number of equations to be solved increases. If the nodes are sparsely placed, then the accuracy might be sacrified. Therefore, it is crucial to perform mesh independency study when using FEM, by checking whether the solution changes with the mesh size. A sample meshing of the field plated transistor simulated in this work using commercial software ANSYS is shown in Figure 2.11. The heat generation is model as a sheet at the interface of AlGaN/GaN where the 2DEG is. The regions where a higher temperature gradient is expected is meshed with a higher mesh density whereas the mesh density is reduced elsewhere to reduce the computational burden. Figure 2.11 shows half of the device; if the geometry is symmetric along certain axes, then the device size can be reduced to decrease computational time.

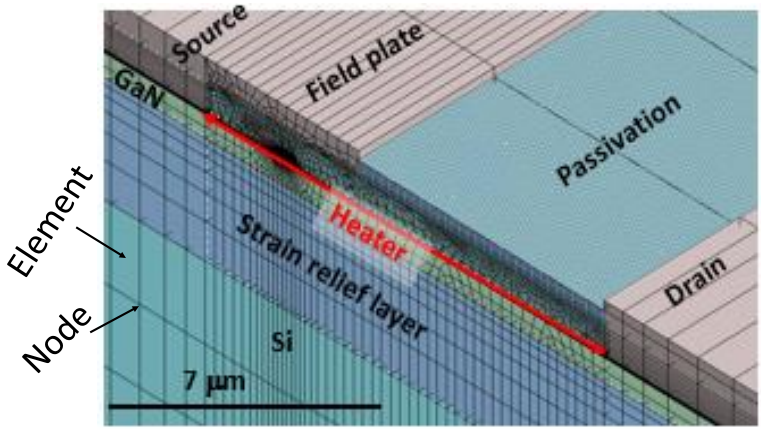

FIGURE 2.11. Sample mesh of a HEMT in ANSYS.

CHAPTER 3

COMPLEMENTARY EXPERIMENTAL METHODS

The purpose of this chapter is to introduce the details of the complementary experimental thermography techniques used in this work. The techniques explained in this chapter were mainly used to verify the results of the main thermal metrology developed in this work, HQTI (Chapter 4 and Chapter 5), in addition to the analysis of the thermal bottlenecks of multi-finger power devices (Chapter 6). In this chapter, the underlying theory and experimental configurations of the standard and nano-particle assisted steady-state and transient Raman thermography, IR thermography and transient thermoreflectance (TTR) techniques are explained in detail. Raman thermography was used to estimate the thermal conductivity of the strain relief layer of the devices used in this work (Chapter 4), along with the simulation, as well as for the analysis of the thermal bottlenecks of power devices (Chapter 6). Steady state and transient nano-particle assisted Raman thermography were used for the verification of the new technique developed in Chapter 4 and Chapter 5. IR thermography was used for screening of devices (Chapter 4 and Chapter 6). Transient thermoreflectance thermography was used for the verification of the new transient thermal metrology developed in Chapter 5.

3.1 Raman thermography

3.1.1 Basics of Raman scattering

Light interacts with matter in different ways and can scatter either *elastically* or *inelastically*. If the light elastically scatters from the atoms or molecules whose diameter is smaller than the incident wavelength, then this process is called as *Rayleigh scattering*. Time dependent inhomogeneities in the material result in inelastic scattering [103], where the frequency of the incident light changes. This inelastic scattering of the light from matter is called *Brillouin scattering* or *Raman scattering*, depending on the branch (acoustic vs. optical) of the lattice vibrations (phonons) that the light interacts with. In a diatomic crystal, the two atoms vibrate in phase with each other in the acoustic branch whereas they vibrate out of phase in the optical branch. In fact, the scattering of photons from matter can also be due to the interaction of the incident light with other types of quasi-particles in the material, such as plasmons (free carrier oscillations). Here we limit the discussion to only the scattering due to photon-phonon interactions since phonon modes were probed in this work. Brillouin scattering is the result of the incident light interacting with the acoustic phonons whereas Raman scattering is due to the interaction of light with the optical phonons. Both types of scattering can be exploited to measure the temperature of the material, which is the main purpose in this work. Yet, Brillouin scattering requires a more complicated equipment to observe as the frequency shift is much smaller than that of Raman scattering [87]. In this work, the frequency shift of the optical phonons is probed for temperature measurements. Therefore, the following explanations focus on Raman scattering from optical phonons.

Raman scattering was first predicted theoretically by Smekal in 1923. The first observation was realised by Raman and Krishnan, by focusing filtered sunlight on sixty different liquids [104]. This work, published in 1928, brought C.V.Raman the Nobel Prize in 1930. The fundamentals of Raman scattering can be explained under the framework of quantum mechanical and classical electromagnetic theory. The former provides a more quantitative basis (such as predicting scattering probabilities) whereas the latter gives a more simplistic and qualitative picture [105]. Both descriptions are explained briefly below with the given order.

From quantum mechanical point of view, Raman scattering from phonons involves creation or annihilation of a phonon upon the excitation of an electron to a virtual state by a photon. When the excited electron relaxes back to its ground state after a short period of time, a phonon is either created or destroyed. Phonon creation and annihilation processes are specifically named as *Stokes scattering* and *Anti-Stokes scattering*, respectively. The energy conservation principle requires the frequency change of the scattered photon during this energy transfer process between a photon and a phonon, which is given by:

$$\omega_s = \omega_i \mp \omega_p \tag{3.1}$$

where ω_s and ω_i are the frequencies of the scattered and the incident photon, respectively. ω_p is the frequency of the phonon involved in the scattering process. The frequency of the scattered light decreases if the energy is gained by a phonon (Stokes process); it increases if a phonon, which was already present, transfers its energy to a photon (Anti-Stokes process). The schematic describing the scattering processes is given in Figure 3.1.

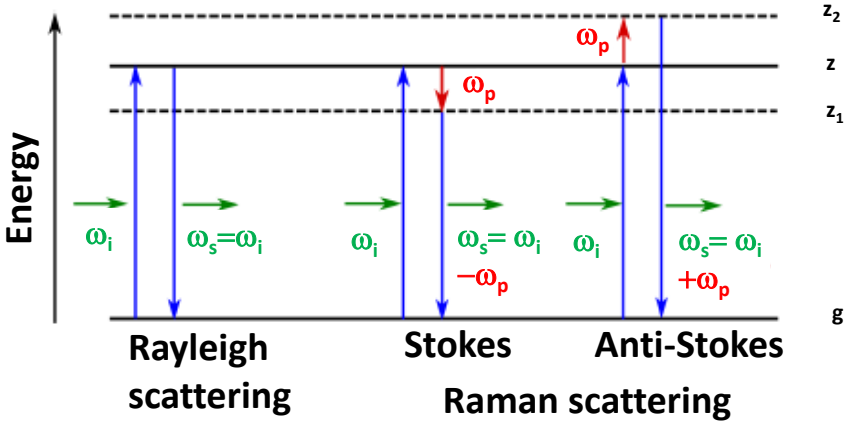

FIGURE 3.1. Schematic of quantum mechanical interpretation of scattering: The horizontal black lines represent electron virtual energy levels, and the green arrows represent photons with their frequency labelled. The dashed lines represent vibrational energy level which are accessed through electrons interacting with phonons, represented by the red arrows. Adopted from [65].

The full quantum mechanical treatment gives the intensity ratio of anti-Stokes to Stokes process as:

$$\frac{I_{anti-Stokes}}{I_{Stokes}} = exp(\frac{-\hbar\omega_p}{k_B T}) \tag{3.2}$$

where $\hbar$ is the reduced Planck constant, k_B is the Boltzmann constant and T is the temperature. According to Equation 3.2, the intensity of Anti-Stokes scattering, which requires phonons to be present in the crystal, decreases with decreasing temperature. This is because the probability of a phonon to be present in the crystal (so that it can participate in anti-Stokes process) decreases as the temperature decreases. This is formulated by Bose-Einstein statistics which governs phonon statistics and is given by:

$$n(\hbar\omega_p, T) = \frac{1}{exp(\frac{\hbar\omega_p}{k_B T}) - 1} \tag{3.3}$$

where n is the phonon population at a particular energy ($\hbar\omega_p$) and temperature T. On the contrary, the Stokes process, which does not require any phonon to be present, can be observed at any temperature. Generally, Stokes shift is used in Raman scattering experiments [27], as done in this work, due to its higher probability, and thus higher intensity, which makes its detection easier and faster.

From a classical electromagnetics point of view, the crystal needs to change its electronic polarisation state due to the vibration of quasi-particles (phonons in this context) in the lattice for the occurrence of Raman scattering. This can be mathematically expressed by considering the polarisation vector ($\boldsymbol{P}$) of the medium which interacts with the light with the electric field ($\boldsymbol{E}$), the real part of which is expressed as [105]:

$$\boldsymbol{E} = \boldsymbol{E_{amp}} cos(\omega_i t) \tag{3.4}$$

where $\boldsymbol{E_{amp}}$ is the amplitude of the time(t) varying sinusoidal electric field of the light with frequency ω_i. The response of the polarisation of the medium to the incident electric field is related by the equation:

$$\boldsymbol{P} = \epsilon_o \boldsymbol{\chi} \boldsymbol{E_{amp}} cos(\omega_i t) \tag{3.5}$$

where ϵ_o is the permittivity of free space, $\boldsymbol{\chi}$ is the volumetric electric susceptibility of the material. Electric susceptibility of the material is a function of crystal geometry, ω_i and lattice displacement

$\boldsymbol{Q}$, i.e. χ= f(ω_i,$\boldsymbol{Q}$) for a certain crystal. The function $\chi(\omega_i,\boldsymbol{Q})$ can be written as a Taylor expansion around $\boldsymbol{Q}$ while neglecting higher order terms:

$$\chi = \chi_o + (\frac{\partial \chi}{\partial \boldsymbol{Q}})\boldsymbol{Q} \tag{3.6}$$

The first term χ_o in Equation 3.6 is the electronic susceptibility of the material under no vibration. If the atomic displacement vector is modeled as a simple harmonic oscillator:

$$\boldsymbol{Q} = \boldsymbol{Q_{amp}} cos(\omega_p t) \tag{3.7}$$

where $\boldsymbol{Q_{amp}}$ is the amplitude of the time (t) varying sinusoidal displacement of the lattice, vibrating with frequency ω_p. Substituting Equation 3.7 into Equation 3.6 and combining the resulting expression with Equation 3.5 gives:

$$\boldsymbol{P} = \epsilon_o \chi_o \boldsymbol{E_{amp}} cos(\omega_i t) + \epsilon_o \boldsymbol{E_{amp}} cos(\omega_i t)(\frac{\partial \chi}{\partial \boldsymbol{Q}})\boldsymbol{Q_{amp}} cos(\omega_p t) \tag{3.8}$$

Using the trigonometric identity:

$$\cos(\omega_i t)\cos(\omega_p t) = \frac{1}{2}[cos(t(\omega_i + \omega_p)) + cos(t(\omega_i - \omega_p))] \tag{3.9}$$

and rewriting Equation 3.8 gives:

$$\boldsymbol{P} = \epsilon_o \chi_o \boldsymbol{E_{amp}} cos(\omega_i t) + \frac{1}{2}\epsilon_o \boldsymbol{E_{amp}}(\frac{\partial \chi}{\partial \boldsymbol{Q}})\boldsymbol{Q_{amp}}[cos(t(\omega_i + \omega_p)) + cos(t(\omega_i - \omega_p))] \tag{3.10}$$

The first term in Equation 3.10 is the dipoles oscillating with the same frequency with that of the incident light, ω_i. The second term is the polarisation induced by a phonon. The frequencies (ω_i-ω_p) and (ω_i+ω_p) represent the dipoles oscillating with the Stokes-shifted and anti-Stokes shifted frequencies, respectively. Oscillating dipoles with certain frequencies cause dipole radiation at the same frequency with their oscillation, i.e. light scattering, which is named as Rayleigh and Raman scattering (with Stokes and anti-Stokes shifted frequencies). As evident from Equation 3.10, in order to observe Raman scattering, a polarisation change ($\partial\chi/\partial\boldsymbol{Q}$) needs to be induced in the material. The polarisation change multiplied by the the unit vector in the direction of the atomic displacement ($\widehat{\boldsymbol{Q}}$=$\boldsymbol{Q}$/ $|\boldsymbol{Q}|$) is defined as *Raman tensor*:

$$\boldsymbol{R} = (\frac{\partial \chi}{\partial \boldsymbol{Q}})\widehat{\boldsymbol{Q}} \tag{3.11}$$

The Raman tensor of a crystal gives information about the intensity of Raman scattering at a particular crystal orientation under certain polarisation directions of the incident light. The intensity of the Raman scattered light and Raman tensor are related by [56]:

$$I_{Raman} \propto |\boldsymbol{e_i R e_s}| \tag{3.12}$$

where $\boldsymbol{e_i}$ and $\boldsymbol{e_s}$ are the polarisation directions of the incident and the scattered light, respectively.

As discussed in Chapter 2.1, group theory can predict phonon modes of a particular crystal structure and their unique Raman tensors. In this work, phonon modes of wurtzite GaN structure grown along its *c* plane and Si phonon modes along (111) direction were probed for the standard Raman thermography measurements. As a reiteration of the discussion in Chapter 2.1, for the wurtzite structure, group theory predicts eight sets of phonon modes at the centre of the Brillouin zone (at the Γ point): $2A_1$, $2E_1$, $2B_1$, $2E_2$ [56]. One set of A_1 and E_1 modes are acoustic, the rest are optical phonons [56]. Optical phonon modes of GaN are shown in Figure 3.2. However, not all optical phonons are Raman-active, which means that some of them may not appear in the Raman spectrum even if their frequency changes. For a phonon mode to be Raman-active, the polarisation direction of the incoming and the scattered light need to be selected such that its Raman tensor gives a non-zero intensity according to Equation 3.12. In this work, the measurements were performed at the backscattering configuration, meaning that the incident and the measured scattered light are along the same direction (antiparallel). The direction of the incident light is along the *c* axis of GaN, which can be considered as *z* direction. In this case, the sample is at *x*-*y* plane, perpendicular to its *c* axis. If we take the polarisation direction of the linearly polarised incident light (laser in this work) along *x* direction, then the geometry of the experiment can be described by Porto notation [106] : $i(jk)l$ as $z(x\text{-})\bar{z}$, where $i(=z)$ and $l(=\bar{z})$ describe the incident and scattering light directions, respectively (which are antiparallel as noted previously). $j(=x)$ and k(=-) describe the polarisation direction of the incident and scattered light, respectively. As the polarisation state of the scattered light is not analysed in this study, it is denoted as (=-) here. Raman-active modes in wurtzite GaN crystal, A_1(LO), E_2 and E_1, and their atomic displacement directions are indicated with red label in Figure 3.2. LO represents longitudinal direction, meaning that the atoms vibrate in the direction of the propagation. Raman tensors of

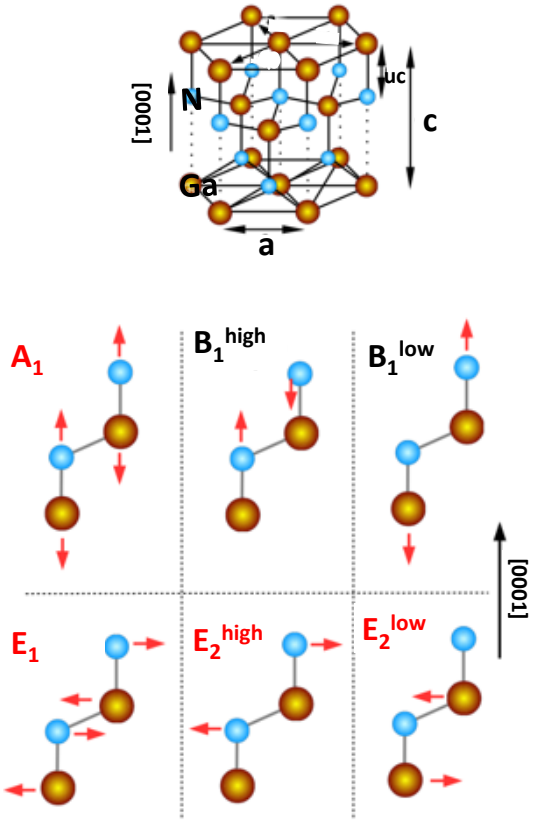

FIGURE 3.2. Schematic of GaN crystal and its optical phonon modes. Ga and N atoms are shown as brown and blue spheres, respectively. Raman-active phonon modes are labelled as red: B_1 mode is silent. High frequency mode: lighter atom (N) is displaced; low frequency mode: heavier atom (Ga) is displaced. Adopted from [27].

the Raman-active modes are given as [107]:

$$\boldsymbol{R}_{A_1} = \begin{bmatrix} a & 0 & 0 \\ 0 & a & 0 \\ 0 & 0 & b \end{bmatrix} \boldsymbol{R}_{E_1^{high}} = \begin{bmatrix} 0 & 0 & 0 \\ 0 & 0 & c \\ 0 & c & 0 \end{bmatrix} \boldsymbol{R}_{E_1^{low}} = \begin{bmatrix} 0 & 0 & -c \\ 0 & 0 & 0 \\ -c & 0 & 0 \end{bmatrix} \tag{3.13}$$

$$\boldsymbol{R}_{E_2^{high}} = \begin{bmatrix} 0 & d & 0 \\ d & 0 & 0 \\ 0 & 0 & 0 \end{bmatrix} \boldsymbol{R}_{E_2^{low}} = \begin{bmatrix} d & 0 & 0 \\ 0 & -d & 0 \\ 0 & 0 & 0 \end{bmatrix}$$

where a, b, c and d are the non-zero constants, which can be determined either by polarisation experiments for a known crystal structure [107, 108] once the polarisation directions of the

incident and scattered light are known, or by *ab initio* molecular orbit calculations, which solve for the force constants between the atoms, resulting normal modes of vibrations and the induced charge polarisation due to those vibrations [108]. It is evident from Equations 3.12-3.13 that only A_1(LO) and E_2 modes give a non-zero Raman scattering intensity in the $z(x\text{-})\bar{z}$ geometry selected in this work, meaning that these are the only Raman-active modes in this configuration.

As the devices used in this work are GaN-on-Si, phonon modes of Si from (111) plane were also probed simultaneously to estimate of strain relief layer thermal conductivity and to obtain extra information for thermal simulation calibration. Group theory predicts only one optical phonon mode at the centre of the Brioullin zone, F_{2g}, which can be observed in this back-scattering configuration [109]. F denotes that the phonon modes are in *x, y, z* directions, considering a cartesian coordinate system [20]. In this experimental configuration, Raman tensors of Si, are [109]:

$$\boldsymbol{R}_x = \begin{bmatrix} 0 & 0 & 0 \\ 0 & 0 & d \\ 0 & d & 0 \end{bmatrix} \boldsymbol{R}_y = \begin{bmatrix} 0 & 0 & d \\ 0 & 0 & 0 \\ d & 0 & 0 \end{bmatrix} \boldsymbol{R}_z = \begin{bmatrix} 0 & d & 0 \\ d & 0 & 0 \\ 0 & 0 & 0 \end{bmatrix} \tag{3.14}$$

3.1.2 Raman thermography

The frequency of lattice vibrations in the crystal is determined by the atomic masses and the bond length between the atoms. Any change in the crystal which results in stretching or contraction of the bond lengths will modulate the phonon frequency. Both temperature and stress can change the bond length by changing interatomic distance between the atoms, which in turn changes the phonon frequency. Raman thermography exploits this temperature dependency of the phonon frequency and was applied to measure the temperature of operating devices in this work. Phonon frequency and temperature can be related by the purely empirical equation first proposed by Cui [110], i.e. *Cui Equation*:

$$\omega(T) = \omega_o - \frac{A}{exp(\frac{B\hbar\omega_o}{k_B T}) - 1} \tag{3.15}$$

where ω_o is the phonon frequency at 0 K, A and B are material and phonon mode dependent empirical constants obtained from sample specific calibration. In spectroscopy, phonon frequency

is usually expressed in wavenumber (=$\frac{1}{\lambda}$), in the unit of cm^{-1}. The calibration is sample specific because for the samples that are grown on different substrates which have different lattice constants, a built-in stress is present.

Device thermography is performed by measuring the phonon frequency at a known temperature (room temperature of 25^{o}C in this work) and when the device is under bias at an unknown elevated temperature. As the temperature measurements are performed on biased devices, stress effects induced during device operation are also present, which couple with temperature induced phonon frequency change. The stress components during device operation, specifically GaN-on-Si devices in this work, are (i) thermo-mechanical stress, which is induced due to different temperature expansion coefficients of device layers, and (ii) inverse piezo-electric stress, which is induced due to the electric field in GaN buffer [111]. It is important to decouple these effects from the temperature induced phonon shift for an accurate temperature measurement. Thermo-mechanical stress effects can be partially decoupled by calibration; however, during device operation the substrate and the GaN buffer will not be at the same temperature due to heat transfer from hotter channel to the cooler heat sink, which is the thermal chuck on which the sample is placed in our measurements. It is possible to decouple thermo-mechanical stress effects from temperature measurements by probing two phonon modes of GaN, i.e. E_2^{high} and A_1(LO) simultaneously [29]; although not always practical due to low A_1(LO) intensity. A practical solution to decouple inverse piezo-electric stress is to take the pinched-off state as a reference state (no current, no heating but electric field present), rather than the off state (no current, no heating, no electric field)[17, 29, 111] since the electric field within the buffer can be considered identical between the pinched-off and on state, gate bias causing negligible $\Delta\vec{E}_z$, z representing the vertical electric field along c axis, between these two states.

In this work, only E_2^{high} mode is probed due to its high scattering intensity. Although this mode is more prone to thermo-mechanical stress effects [29], it yields sufficiently accurate results when thermo-mechanical stress is negligible, which is the case when the devices operate with a less than ≈25 W/mm power dissipation [29], as in this work. In this work, the calibration coefficients of $A_{E_2}^{high}$=20.57 cm^{-1}, $B_{E_2}^{high}$=1.33 and ω_{o,E_2}^{high}=568.03 cm^{-1}; $A_{F_{2g}}$=12.59 cm^{-1}, $B_{F_{2g}}$=0.66 and $\omega_{o,F_{2g}}$=523.3 cm^{-1} were used for GaN and Si, respectively, which were obtained from a former

PhD student in our group, Dr. Hangfeng Ji. For a more detailed discussion of Raman scattering based device thermograhy, Ref. [111] and Ref. [29], which are very comprehensive review articles, are suggested.

3.1.2.1 Renishaw inVia Spectrometer

Raman scattering is a very weak process, i.e. only 1 in ≈ 1-10 million photons are inelastically scattered [109]. Therefore, observation of this weak effect requires a very sensitive equipment, which includes an intense monochromatic light source, an efficient filtering for the reflected and Rayleigh scattered light, which has a much higher probability than Raman scattering, and a sensitive light detector. Since the advent of the laser in 1960s, lasers have being used as the standard light source for spectrometers [103] as they can emit light with very high intensity and with very low divergence, which make them easier to focus with low optical losses. In this work, Renishaw inVia spectrometers were used utilising two separate light sources: 488 nm Argon ion laser and 532 nm Nd:YAG (YAG: $Y_3Al_5O_{12}$) laser.

The Renishaw inVia spectrometer is integrated with a Leica microscope. The sample (device under test) is placed on a Prior *xyz* motorized stage, which has 3 axis of translation with 0.1 μm precision. Tungsten needle probes mounted on micropositioners were used to bias the device. The Renishaw system is placed in a box to prevent any ambient light from interfering with the measurement. The schematic of the Raman spectroscopy set-up is shown in Figure 3.3. An adjustable neutral density filter is placed after the laser source in order to control laser power. The laser is directed towards the beam expander with the right-hand mirror shown in Figure 3.3. The computer controlled beam expander, which consists of two lenses with the same focal point, adjusts the beam diameter such that it fills the back aperture of the microscope. After the beam expander, the beam remains collimated. The laser is focused on the sample by adjusting the beam expander. Beam expander adjustment ensures that the laser light to excite the sample and the white light image of the sample viewed from the camera on top of the microscope are on the same focal plane. A second adjustable left-hand mirror shown in Figure 3.3 directs the laser light towards the laser light rejection filters through another mirror located at the top of spectrometer. Laser light rejection filters, also called as "Rayleigh filters", can be either edge (long-pass) or

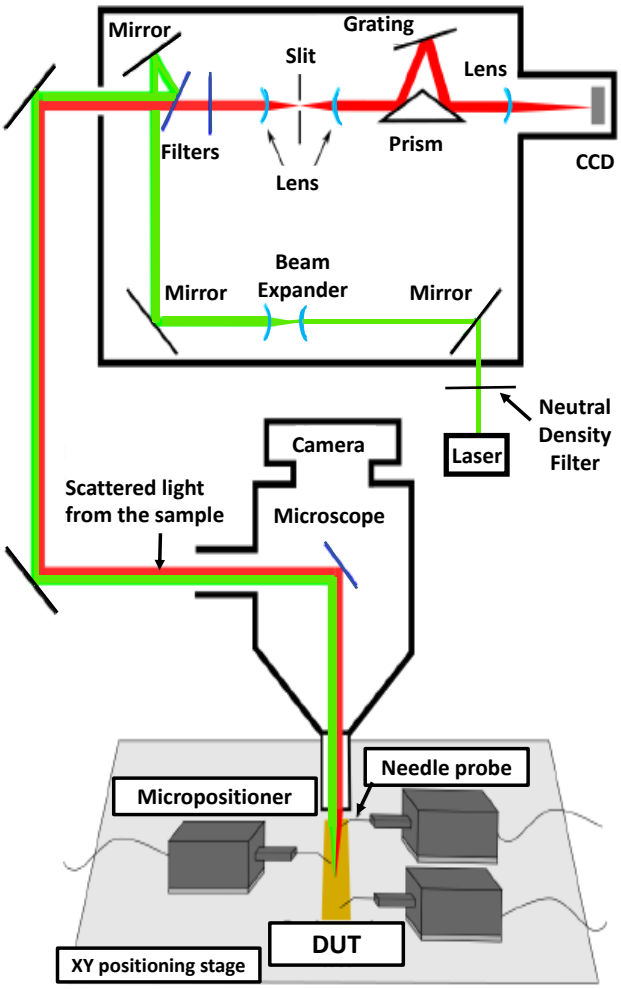

FIGURE 3.3. Schematic of Raman spectroscopy set-up. Adopted from [65].

notch (stop-band) filters. These filters reflect the laser light and transmit Raman scattered light. As the filters are not perfect reflectors, some of the laser light is transmitted. The transmission is reduced to $\approx 10^{-12}$-10^{-9} of the incoming light by using two filters [11]. After passing the filter, the laser light is sent to the microscope and focused on the sample with the objective lens. The camera on top of the microscope allows viewing the sample under white light illumination. This is achieved by switching the mirrors and beam splitters mounted on the microscope. Laser spot on the sample can also be viewed through this camera by switching the beamsplitters.

Raman scattering light enters the spectrometer through the filters, which block the Rayleigh

scattering light and transmit Raman scattering light, as explained previously. Raman scattering light is focused on the slit by a pre-slit lens. Slit width is adjusted depending on the desired lateral resolution. A narrow slit width blocks the divergent light, which is outside the focal point. There is a trade-off between the resolution and the signal-to-noise ratio (SNR). Depending on the sample, optical resolution might be compromised to obtain a measurable SNR. Slit width was set to 50 μm in our measurements. The magnification, M, between the sample and the slit was approximately M=10. The slit width can be adjusted between 0-100 μm. The beam is collimated with a post-slit lens after passing the slit and directed to the grating by a prism. Grating, which disperse the light, is the key element in terms of spectral resolution. The spectral resolution and spectral bandwidth are determined by the groove density (or number of lines per mm) of the grating. A grating with a groove density of 2400 lines/mm was used for the measurements performed in this work. Light divided into its spectral components is directed to a charged coupled detector (CCD). The CCD is comprised of 576x284 pixel array. Each pixel is a capacitor, on which charges are accumulated after photons hit the detector. It is cooled by a Peltier element down to -70^{o}C to increase SNR by decreasing thermal noise (free charge due to thermal excitation). Charge accumulation on the CCD starts when the shutter is opened for a certain time interval (exposure time). The number of charges that can be accumulated on a capacitor is limited and if this number is exceeded the CCD is "saturated", meaning that no more charge accumulation is recorded. In this case, the alternative is to decrease the exposure time and take "accumulated" measurements to reach a similar level of SNR with that of a single long exposure.

Before the measurements, the spectrometer is calibrated with a reference Si sample, ensuring that its peak position corresponds to 520 cm^{-1}. This calibration is done by adjusting the position of the grating motors. Raman thermography is a non-invasive technique; no special sample preparation is required. A sample spectrum of the GaN-on-Si device tested in this work at room temperature is shown in Figure 3.4. The spectrum shows that GaN A_1(LO) which is expected to be observed at $\approx$ 734 cm^{-1} [112] is not observed due to thin GaN layer (0.75 μm). The Raman spectroscopy system is controlled with *Wire 2.0* provided by Renishaw. This software controls the motors of *xyz* stage, beam expander and grating and has an analysis interface where peak fitting can be performed. Minimum resolvable wavenumber shift of this system is $\approx$ 0.1 cm^{-1}.

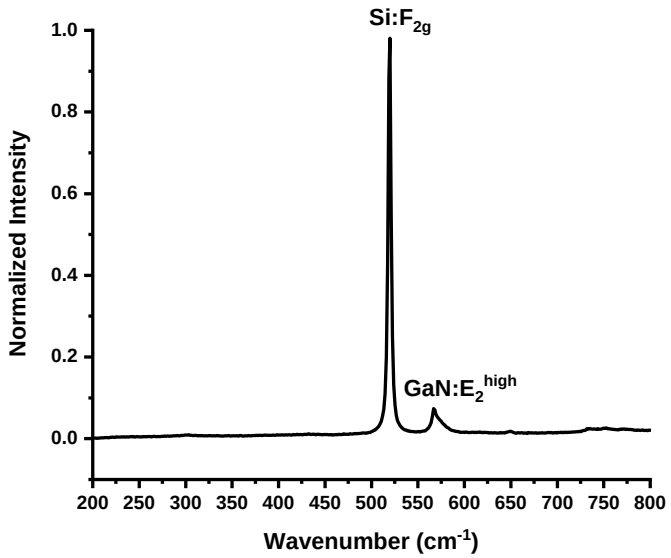

FIGURE 3.4. Sample Raman spectrum of the GaN-on-Si device at room temperature. Si F_{2g} mode and GaN E_2^{high} mode are observed in the spectrum. GaN A_1(LO) mode is not observed in the spectrum due to thin GaN layer.

It is important to consider the optical resolution of the system in order to accurately quantify temperature measurements. There exists several criteria to define the lateral optical resolution, namely Rayleigh, Sparrow or full-width-at-half-maximum (FWHM) criterion. Among which, the most conservative one is Rayleigh criterion, which defines the resolution on Airy disk as the distance between the centre of the Airy disk (brightest region) and the point where first minimum occurs (the inner circle of the first darkest ring). This corresponds to a lateral resolution of:

$$r_{lateral} = \frac{0.61\lambda}{NA} \tag{3.16}$$

where λ is the laser wavelength, which is 488 nm or 532 nm in this work and NA is the numerical aperture of the objective lens, which is 0.5 for a Leica 50x objective lens used in this work. This conservative criterion corresponds to a lateral resolution of ≈ 0.6 μm. The depth (axial) resolution also needs to considered. When the laser light energy is above the bandgap of the material, the depth resolution corresponds to the absorption depth. For instance, for temperature measurements of the Si substrate, the axial resolution equals an absorption depth of $\approx 1\mu$m. For materials which are transparent to the laser, the axial resolution corresponds to the transmission

depth of the laser if the sample is thicker than the transmission depth. The axial resolution is given by [29]:

$$r_{axial} = \frac{0.88\lambda}{n - \sqrt{n^2 - NA^2}} \tag{3.17}$$

where n is the refractive index of the focusing medium. As GaN is transparent under 488 nm and 532 nm laser, for n=2.4, the axial resolution corresponds to ≈ 8 μm for 0.5 NA objective lens. In GaN based devices, GaN layer is usually much thinner than this value (1-2 μm). Therefore, the depth resolution can be approximated as the thickness of GaN layer, which is 0.75 μm for the devices used in this work.

3.1.2.2 Nanoparticle assisted Raman thermography

Nanoparticle assisted Raman thermography allows direct surface temperature probing as the nanoparticles are deposited on the device surface. Their fast thermal equilibrium with the device surface (in ≈ μs range [30] depending on their size) due to their small heat capacity allows measurement of the "effective" surface temperature. This method is advantageous when the sample under test does not have Raman active modes or its Raman modes are too weak to be measurable. They are also free from stress effects discussed in Section 3.1.2.1. In this work, this method allowed direct validation of the HQTI technique (Chapter 4) as both measurements represent surface temperature. We also used this method to probe the field plate metal (Au) temperature , which is not Raman-active, in pulsed device operation (Chapter 5).

This method has been previously applied using diamond nanoparticles [30], silicon nanowires [113], hexagonal boron nitride (hBN) nanoparticles [114] and TiO_2 nanoparticles (anatase) [114, 115]. Here we used TiO_2 nanoparticles as it was proven to provide a higher SNR compared to hBN or diamond nanoparticles by more than an order of magnitude with similar temperature dependency [114]. Temperature dependency of E_g mode (≈ 143 cm^{-1}) of TiO_2 nanoparticles was used in this work due to its highest intensity [65] and found to be ≈0.02442 $cm^{-1}/^oC$ in a previous work in our group [116], which is in line with the values in [114]. Si nanowires, which have similar temperature dependency, were not preferred to be able to probe the temperature of the Silicon substrate simultaneously. We note that room temperature phonon frequency of

the nanoparticles can vary due to their varying intrinsic strain; however, their temperature dependence remains constant.

5 mg/ml of suspension in methanol with 30 nm diameter TiO_2 particles was sonicated and then drop casted onto the surface of the device. It is important to dilute the solution as in this work in order to prevent the agglomeration of the nanoparticles. Otherwise, this would affect the heat transfer by forming a thick layer on the device surface rather than leaving isolated nanoparticles upon evaporation of the solvent. The measurements were performed in the same configuration in Chapter 3.1.2.1 using 532 nm laser and Leica 0.5NA, 50x objective lens. A sample spectrum of the nanoparticle deposited device at room temperature was shown in Figure 3.5. We note that the spatial resolution (both lateral and axial) of this measurement corresponds to size of the nanoparticles, which is 30 nm.

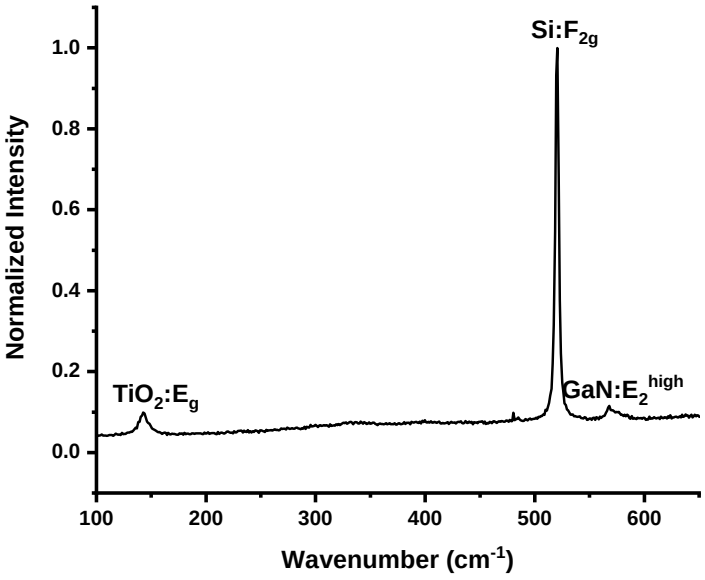

FIGURE 3.5. Sample Raman spectrum of the TiO_2 deposited GaN-on-Si device at room temperature.

3.1.2.3 Time resolved Raman thermography

Time resolution can be achieved by synchronizing the device (electrical) and laser pulses with an adjustable optical time delay, as shown in Figure 3.6(a) [117]. An observable temperature transient can be achieved by decreasing the optical pulse width, to, for example, 10% of the electrical pulse period. Decreasing the optical pulse width diminishes the Raman signal detected. Since Raman scattering is also a very weak effect as discussed in Chapter 3.1.2.1, measuring a single pulse is difficult when combined with decreased optical pulse widths. That is why time averaged signal (a.k.a. boxcar averaging, which will be discussed in more detail in Chapter 5) was measured after the device reaches quasi-steady state. Temperature transient of the device was probed by varying the time delay between the electrical and optical pulses as shown in Figure 3.6(b).

The schematic of the test set-up circuit is shown in Figure 3.6(c). Electrical pulses were generated by an Agilent A81114 pulse generator (slave), which was triggered by a Tabor 8500 pulse generator (master). Optical pulse was created by modulating a CW laser with an acousto-optic modulator (AOM) (Gooch Housego M200-4B/E-LD4), a.k.a. Bragg cell. The master pulse generator drives AOM driver (200 MHz Landwehr RF-driver (A341)) by providing digital output, which then generates optical pulses by turning the AOM on and off. The pulse duration can be adjusted from Tabor 8500 pulse generator. The resulting laser pulse was measured with a photo-diode which was connected to a Keysight DS09404A oscilloscope. An electrical signal was also monitored from the oscilloscope simultaneously. The advantage of AOM is that it allows higher time resolutions in the ns range with a cleaner pulse shape, as the laser is always on (CW), compared to direct electrical modulation which might undesirably change the shape of the pulse width due to longer rise/fall times. AOM is made of a piezoelectric acoustic transducer, an acoustic absorber and an acoustic crystal, as shown in Figure 3.7(a). Piezoelectric acoustic transducer converts electrical signal into mechanical vibrations, which propagate through the crystal medium and then reaches the absorber. The refractive index of the crystal changes, due to the density change caused by mechanical vibrations, such that it creates a periodically varying refractive index pattern, with a period of l. There is no time dependency of the refractive index change, allowing optical pulses with constant intensity. The periodic refractive index change

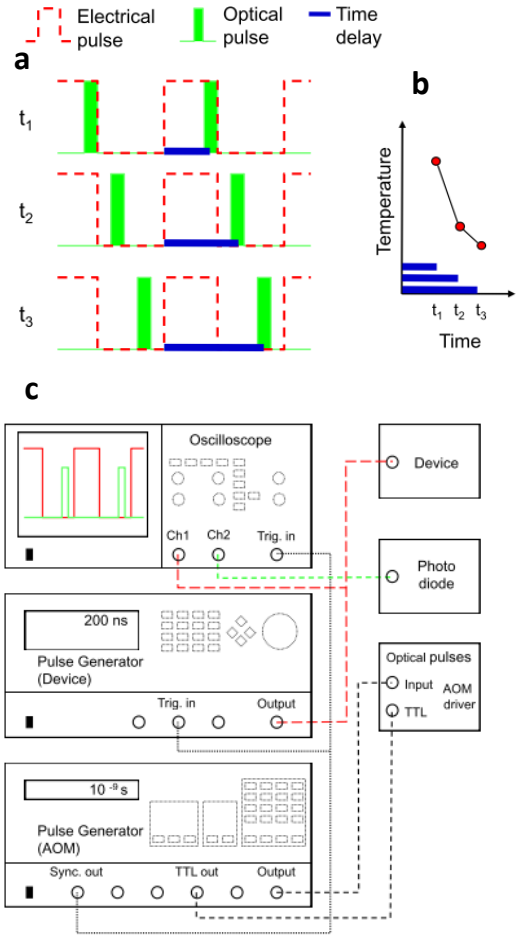

FIGURE 3.6. Working principle of time resolved Raman thermography [117].(a) Schematic showing the synchronization between optical and electrical pulses by adjusting the time delay. (b) Temperature evolution of the DUT with varying time delay, corresponding to different time windows of the electrical pulse. (c) Schematics of the circuit of the time resolved Raman thermography set-up.

scatters the incoming laser light such that it is diffracted following Bragg's law of diffraction [117]. This happens when the crystal thickness L is greater than l^2/λ, where λ is the wavelength of the incident light.

The diffracted light from the AOM is directed to the Renishaw Invia Raman system, which is identical to the one shown in Figure 3.3, with a beam splitter. The schematic of the optical set-up is shown in Figure 3.7(b). The time resolution of this system is $\approx$ 10 ns, which is the rise time of the AOM [117].

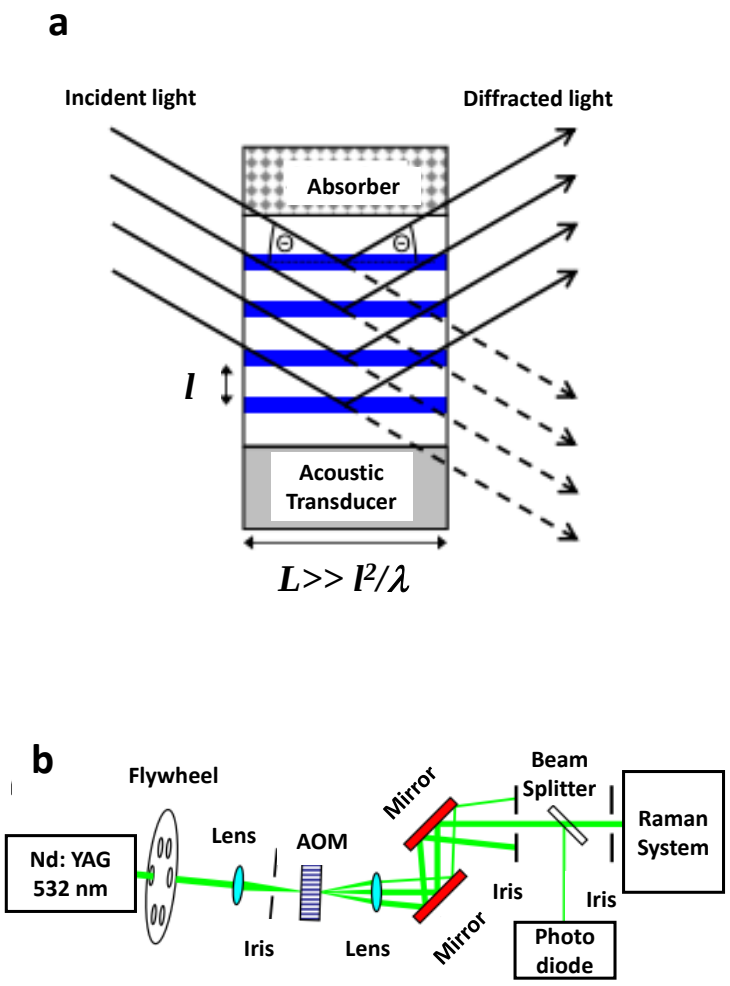

FIGURE 3.7. Optical configuration of time resolved Raman scattering set-up. (a) Schematic of the acousto-optic modulator (AOM) (b) Optical path of the laser. Adopted from [117].

3.2 Infrared (IR) Thermography

All matter emits thermal radiation, in the range of 700 nm-1000 μm, above 0 K. A material that is a perfect emitter and an absorber is called as *black body*. The spectral energy density of a black body is given by Planck's law:

$$u(\lambda, T) = \frac{8\pi hc}{\lambda^5} \frac{1}{exp(\frac{hc}{\lambda k_B T}) - 1} \tag{3.18}$$

where λ is the wavelength of the thermal radiation. However, not every material is a perfect emitter and absorber; emission can be accompanied by reflection and transmission. This is why the concept of *emissivity* (ϵ) is introduced, which is defined as the ratio of a particular material's emission to the black body emission. The total heat flux ($q^{"}$) emitted from a material is given by Stefan-Boltzmann law:

$$q" = \epsilon \sigma T^4 \tag{3.19}$$

where ϵ is the material emissivity ($0 < \epsilon \leq 1$), σ (=5.67x10^{-8} J/(m^{2}sK^4)) is the Stefan-Boltzmann constant. It is this heat flux measured in IR thermography at a certain wavelength range. Typical IR cameras are usually made of InSb detectors, which operate in the mid-IR range (≈3-10 μm).

3.2.1 Quantum Focus Instruments (QFI) Infrared System

In this work, Quantum Focus Instruments Infrascope system, which was integrated into a Leica DMLM microscope, as shown in Figure 3.8, was used. IR radiation emitted from the sample was detected by a 256x256 InSb detector. The detector was cooled with liquid nitrogen (LN_2) for thermal noise reduction. The total field of view using a 16 mm working distance SiGe 15x 0.5 NA objective lens is ≈ 410 x410 μm with 1.6 μm pixel resolution. The system is operated by *Infrascope* software.

Two calibrations were performed before performing device thermography. First, radiosity calibration was performed by focusing the camera on a black circle made on a metal sample, acting as a black body. The black body sample was mounted on top of a computer controlled thermal chuck with a thermal paste in order to ensure sample stability with a thermal contact resistance as low as possible. The camera response was calibrated by measuring the black body

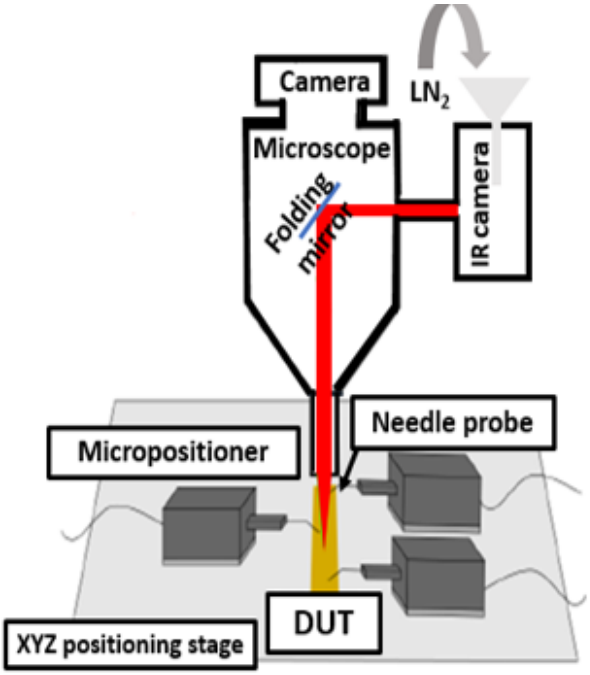

FIGURE 3.8. Schematic of QFI IR thermography set-up. Red line represents the IR radiation emitted from the sample. The schematic of the probe set-up was adopted from [65].

emission at varying chuck temperature from 30^{o}C to 120^{o}C, covering the intended temperature measurement range. This procedure ensures that any shift due to possible non-idealities in the system (such as irregularities in the objective lens or slight changes in the laboratory conditions), which might affect detector response, is corrected. The second calibration is the uniformity calibration. Every infrared detector has some sort of irregularities [118], which might cause what is called as "bad pixels". It is important to correct for these irregularities, especially to identify hot spots accurately. Uniformity calibration was performed with the same black body target at 40^{o}C and 80^{o}C chuck temperature, which were the pre-set temperatures by *Infrascope* software. The response of the defective pixels, which were out of the expected temperature, were offset to be in the pre-set temperature range. As IR emission increases with temperature as shown in Figure 3.9(a), the measurements were performed at an elevated temperature, i.e. 52^{o}C in this case, to improve SNR. As the device surface is complex, consisting of metals and passivation layers with different emissivities, a pixel-by-pixel emissivity map is required. This emissivity map was obtained at 52^{o}C for a GaN-on-Si device used in this work, as shown in Figure 3.10(b).

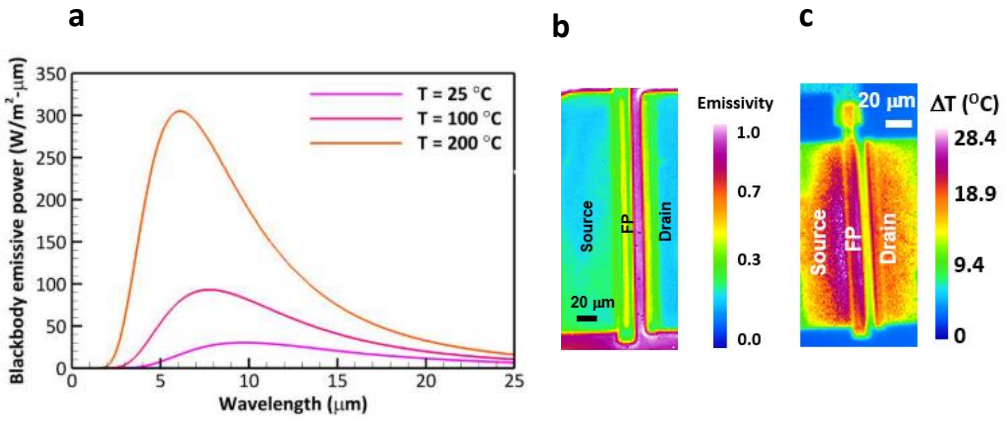

FIGURE 3.9. Response of the IR system. (a) Planck's law showing increasing IR emission with the temperature rise [119]. (b) Emissivity map of the GaN-on-Si single finger device tested in this work. (c) Sample temperature map of the same device shown in (b).

Figure 3.10(b) shows that emissivity of the metal contacts (gold), $\epsilon \approx 0.2$-0.3, is much lower than the passivated channel $\epsilon \approx 0.9$. This low emissivity of metals can lead to inaccurate temperature measurements due to low SNR, which is one of the drawbacks of IR device thermography. A sample thermal map of the same device is shown in Figure 3.9(c).

IR thermogprahy is a well-established wide field thermal imaging technique, which is powerful for qualitative inspection and has been being used since 1960s [25]. However, due to the long wavelength regime measured, the diffraction limited lateral resolution ($r_{lateral}$) is poor compared to visible range measurements. In this work, 16 mm working distance SiGe 15x 0.5 NA objective lens was used, which gives a lateral resolution of $\approx$ 3-6 μm. As GaN, Si substrate and passivation layer (usually Si_xN_y) are all transparent to IR radiation, the temperature measured in the channel represents a volumetric depth average through the device stack. This low spatial resolution, which can be even larger than the channel length, positions IR thermography as a qualitative inspection technique, which is another shortcoming of the technique.

3.3 Transient Thermoreflectance (TTR) Thermometry

Thermoreflectance thermometry exploits temperature dependent reflectivity change of materials. This temperature dependent reflectivity change can be explained classically by Drude-Lorentz model, which assumes that electrons are bound to nuclei by springs so that they behave like a harmonic oscillator. Although this model does not represent the actual atomic picture, it gives a good approximation considering the light-matter interaction. This model assumes that electrons bound to the nuclei vibrate with a natural resonant frequency of ω_o. The electrons are also subjected to collisions due to electron-electron and electron-phonon interactions, which can be lumped into a damping term in the equation of motion with a damping coefficient, γ. Considering one dimensional motion along x-direction, when the medium interacts with the light with the time varying electric field along x-direction ($E(t)$), the equation of motion for a damped oscillator takes the form of:

$$m_e(\frac{\partial^2 x}{\partial t^2} + \gamma \frac{\partial x}{\partial t} + \omega_o^2 x) = qE(t) \tag{3.20}$$

where m_e is the electron mass and $E(t)$ can be expressed in terms of its phase and magnitude as:

$$E(t) = E_{amp,x} cos(\omega_i t) \tag{3.21}$$

where $E_{amp,x}$ is the amplitude of the electric field along x-direction and ω_i is the frequency of the incident light. Substituting Equation 3.21 into 3.20 and solving the partial differential equation for the motion along x-direction gives:

$$x = \frac{qE_{amp,x} cos(\omega_i t)}{m_e(\omega_o^2 - \omega_i^2 + i\gamma\omega_i)} \tag{3.22}$$

where q is the charge of the electron. Electrons oscillating around the nuclei create a dipole moment. The density of dipole moment, or electric polarisation, due to this motion is expressed by:

$$P = qxN \tag{3.23}$$

if there are N contributing electrons per unit volume. Substituting Equation 3.22 into Equation 3.23 gives:

$$P = \frac{q^2 N E_{amp,x} cos(\omega_i t)}{m_e(\omega_o^2 - \omega_i^2 + i\gamma\omega_i)} \tag{3.24}$$

Equation 3.24 considers only the electrons vibrating with natural frequency ω_o. We note that for crystals consisting of different atoms, electrons vibrate with different natural frequencies. In this case, the total polarisation is a sum of all the polarisations induced by the dipoles vibrating with different frequencies. Yet, we continue our discussion with the simplified analysis considering a single natural frequency. As explained in Section 3.1, polarisation induced by the electric field of the incident light can be expressed in terms of the electric susceptibility vector (See Equation 3.5). Combining Equation 3.5 and 3.24 for the one dimensional case, electric susceptibility of the material can be written as:

$$\chi = \frac{q^2 N}{m_e \epsilon_o (\omega_o^2 - \omega_i^2 + i\gamma\omega_i)} \tag{3.25}$$

The electric susceptibility of the material is directly linked to its optical properties. The optical properties of the material are best described by the refractive index, n, which represents how much the speed of light changes in the medium, and the absorption coefficient. Refractive index and electric susceptibility of the material are related by:

$$n^2 = 1 + \chi \tag{3.26}$$

Subsequently, the dispersion relation for the refractive index can be obtained as:

$$n^2(\omega_i) = 1 + \frac{q^2 N}{m_e \epsilon_o (\omega_o^2 - \omega_i^2 + i\gamma\omega_i)} \tag{3.27}$$

Equation 3.27 indicates that (i) refractive index is dependent on the wavelength of the incident light and (ii) it includes a complex term associated with the damping coefficient, which represents the dissipative effects. For conductors, such as metals, there are also free electrons contributing to the electric polarisation of the material. As free electrons are not bound to the nuclei, there is no restoring force, meaning that ω_o=0. For the case of metals, when only free electron contributions to the electric susceptibility is considered and when damping effects are neglected, we can obtain the relation:

$$n^2(\omega_i) = 1 - \frac{q^2 N}{m_e \epsilon_o (\omega_i^2)} \tag{3.28}$$

Here we can introduce the idea that free electrons and positive ions in a metal can be considered as plasma vibrating at a natural frequency of ω_p, which is termed as *plasma frequency* and is

given by:

$$\omega_p^2 = \frac{q^2 N}{m_e \epsilon_o} \tag{3.29}$$

This concept is important in terms of characterising the dissipative properties of the medium. When the incident light is below the plasma frequency, the complex part of the refractive index dominates and the energy is dissipated in the medium as heat. This complex part is called as *absorption* or *extinction coefficient*, k. The complex refractive index of the medium can, thus, be expressed as $n+ik$. As clearly seen from Equations 3.27-3.28, any change in the volume of the medium would change the number of the electrons per unit volume, N, which would change the refractive index. This is why stress and temperature can modulate the refractive index by changing the lattice spacing. Thermoreflectance is based on this refractive index modulation of the material due to temperature change. Reflectivity, R, is a directly measurable quantity and is given in terms of refractive index, by *Fresnel equations*, for a normal angle of incident when the medium between light and the material is air (n_{air}=1):

$$R(T,\omega_i) = \frac{(n(T,\omega_i)-1)^2 + k^2(T,\omega_i)}{(n(T,\omega_i)+1)^2 + k^2(T,\omega_i)} \tag{3.30}$$

For a lossless medium, which is transparent to the incident wavelength, k=0.

The temperature dependency of the reflectivity of a medium can be characterised by the thermoreflectance coefficient, C_{th}(= dR/dT) for a certain frequency of the incident wavelength. It is important to select the optimum wavelength such that C_{th} is maximum for higher SNR, resulting in higher accuracy and faster measurements. Reflectivity change with temperature is related by:

$$\frac{R - R_{ref}}{R_{ref}} = C_{th} \frac{T - T_{ref}}{T_{ref}} \tag{3.31}$$

where R_{ref} corresponds to reflectivity at a reference temperature, T_{ref}. C_{th} for metals is usually on the order of 10^{-6}-10^{-4} K^{-1} at room temperature [120]. In this work, the thermoreflectance technique was applied on pulsed devices and the reflectivity change due temperature rise during the device pulse was monitored simultaneously.

It is crucial to know where the reflection takes place to interpret temperature measurements accurately. In order to achieve high optical resolution with minimal surface heating, the

visible wavelength range can be preferred for thermoreflectance measurements. However, as the device layers, such as passivation, AlGaN and GaN, are transparent in the visible range, sub-surface reflections, a.k.a. *interference* effects occur. The refractive index of each layer and their temperature dependency are different. Reflectance is also a highly surface dependent property. Therefore, sample dependent calibration is required. Generic calibration is performed by heating the sample over a known temperature range and measuring the reflectivity change. As pointed out in Section 3.1, samples grown on different substrates exhibit built-in stress and are thermally stressed due to different thermal expansion coefficients. We have already pointed out that stress can also affect reflectivity of the material. During calibration, the effects of the built-in stress can be circumvented; yet, thermal stress effects cannot be eliminated because in actual device operation there is a temperature gradient within device layers unlike the homogeneous temperature distribution in calibration. Besides, the estimation of the depth of the reflected signal from the transparent device layers is challenging due to this temperature gradient and the corresponding temperature dependent refractive index change. This is the biggest limitation of thermoreflectance based thermography. Recently, a commercial developer reported a solution based on multi-wavelength incident light to circumvent SNR related challenges due to different thermoreflectance coefficient with varying wavelength [121]. This approach surely helps for higher SNR; however, how the interference effects driven by temperature dependent refractive index change at the visible wavelength are accounted for still remains as an unanswered question, which makes the interpretation of the temperature measurements challenging, and is, in fact, the motivation of the development of a new technique in this work.

In this work, we measured source connected field plate (gold) temperature using 532 nm laser, i.e. below the plasma frequency of gold, such that the laser light is absorbed by the gold near the surface ($\approx$ 16 nm [122]), eliminating interference effects while ensuring that laser heating is minimal not to cause a measurable temperature change. 532 nm wavelength incident light is reasonable for gold as it gives a high C_{th} as shown in Figure 3.10. The calibration of the thermoreflectance signal is performed by TiO_2 assisted Raman measurements, which is described in detail in Chapter 5, along with other calibration approaches.

The optical set-up integrated into Raman system is shown in Figure 3.11: 532 nm laser is

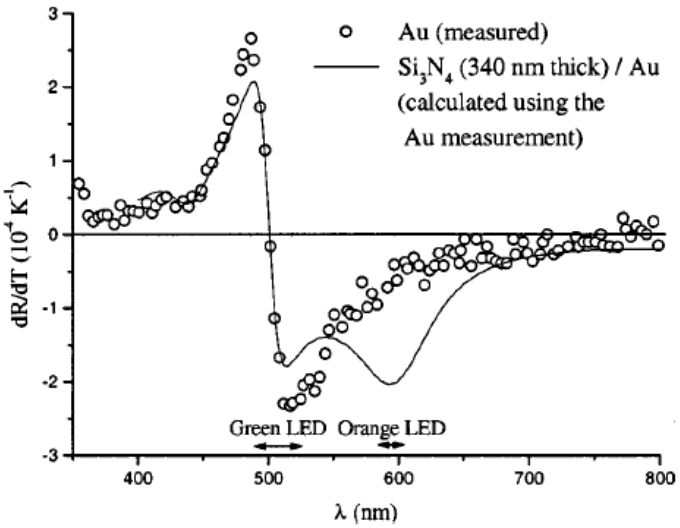

FIGURE 3.10. Spectrum of C_{th} measured in the case of bare gold (circles), and calculated in the case of Si_3N_4 coated gold (line). The arrows indicate the FWHM spectral width of two of the LEDs. Reproduced from [123], with the permission of AIP Publishing.

directed into the microscope through a polarising beam splitter, and the reflected light is directed to the photo-diode through the same beam splitter. The photo-diode was connected to an Agilent DSO-x 3034A, 350 MHz oscilloscope, from which the device pulse is monitored simultaneously.

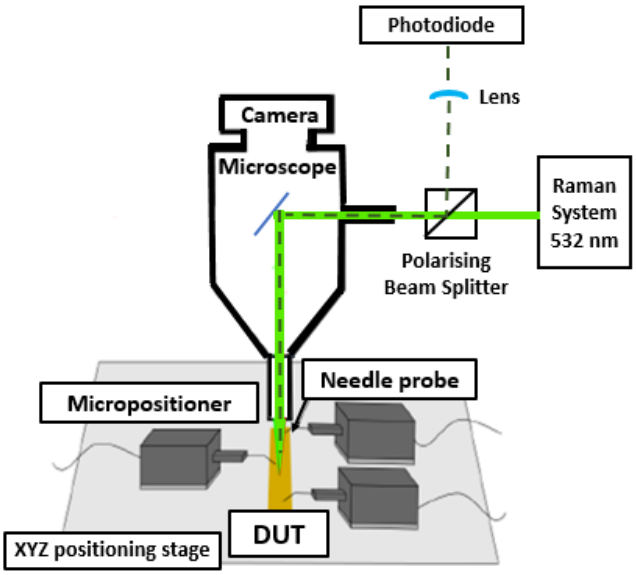

FIGURE 3.11. Schematic of TTR set-up. The schematic of the probe set-up was adopted from [65].

CHAPTER 4

HYPERSPECTRAL QUANTUM ROD THERMAL IMAGING (HQTI): DEMONSTRATED ON A GAN HEMT

This chapter describes the development and demonstration of a new thermography technique. The experimental set-up along with the data processing details are explained. As the current interest in semiconductor device development is on the wide or ultra wide band gap materials, the experimental technique was demonstrated on a GaN based device. The new technique was bench marked against the standard thermography techniques. The advantages and limitations of the new technique are discussed. This section includes a significant content from our recent publication, Ref. [124], albeit with more details[1].

4.1 The working principle of the technique

Hyperspectral quantum rod thermal imaging (HQTI) relies on measuring the temperature dependent band gap change of semiconductor nanoparticles, i.e. quantum rods (QRs) discussed in Chapter 2.2, which are deposited on the surface of a device under test (DUT), by accumulating the emitted photoluminescence (PL) light spectrum with a hyperspectral camera equipment.

[1] *A significant portion of the figures in this chapter were reprinted from our recent publication, in part with permission from ACS Appl. Electron. Mater. 2, 1, 93–102, Oner, B. et al., Submicrometer Resolution Hyperspectral Quantum Rod Thermal Imaging of Microelectronic Devices, Copyright (2020), American Chemical Society.*

As the nanoparticles have low heat capacity and negligible radiation loss owing to their small size,they reach thermal equilibrium with the surface of the DUT quite fast, i.e. for example, on the order of 10 μs as demonstrated for 1 μm size diamond nanoparticles [30]. Therefore, once the steady state condition is reached, measured temperature can be considered equivalent to the surface temperature that the nanoparticles are in contact with, as long as the nanoparticles are distributed individually or form a thin enough coating layer typically ≈a μm thick. The temperature dependent peak emission wavelength of the QRs on top of the DUT is measured at a reference condition (the device OFF or Pinched-OFF), and at the ON state of the device at a single shot across the whole field of view (FOV) of the imaging set-up. The emission images at various wavelengths are collected using a hyperspectral camera equipment, which consists of a liquid crystal tunable filter (LCTF) and a monochrome camera in our set-up.

Hyperspectral imaging means gathering the intensity information of an image at various wavelengths with a "single shot" [125, 126]. Here, "single shot" emphasizes that the technique does not rely on scanning but relies on the direct imaging of the region of interest (ROI). The spectral images correspond to three dimensional (3-D) data: two dimensions representing the spatial (x, y) and one dimension showing the spectral (λ) information, namely $I(x, y, \lambda)$.

Spectral imaging is classified specifically as "multispectral" or "hyperspectral", depending on the number of spectral bands, i.e. wavelength intervals, collected. The precise distinction is somewhat blurry in the literature and depends on the application area. Here, we use the word "hyperspectral" for n=29 bands because this is the preferred terminology in electronic applications [121, 127]. The advantage of hyperspectral imaging is that it reduces image acquisition times by not requiring point by point scanning unlike spectroscopy. For the novel technique developed here, utilising QRs as the sensors further decreases the acquisition times due to their high quantum efficiency (QE), which is discussed in Chapter 2.2.

The concept of spectral imaging has been explored for various applications, from art conservation [128] to pathology [129] and atmospheric imaging [130] to cathodoluminescence based defect characterisation in nitride based structures [127]. It is also possible to see commercial applications exploiting the natural IR emission from the surfaces above 0 K [131, 132]. In fact, the hyperspectral thermal imaging approach has been demonstrated for temperature measurements

for climate applications, such as measuring sea temperature, using infrared emission [133]. This approach can also be adopted for the device applications considered here. However, the benefit would be minimal due to three reasons: (1) the resolution would still be limited by the wavelength of the IR emission, making sub-micron resolution unachievable, (2) the weak IR signal would require expensive detectors and (3) the background radiation from the device layers would still be present, making the interpretation of the signal difficult. Considering visible wavelength emissions as done in this work improves the optical resolution. Another recent development in the field is hyperspectral thermoreflectance imaging [121], which utilizes multi-wavelength light source as briefly discussed in Chapter 3.3. This approach is more promising compared to measuring IR emission due the its higher spatial resolution in the visible wavelength range. Yet, the challenge of exhaustive calibration for each device structure and the interference effects due to temperature dependent thermoreflectance coefficient, making the interpretation of the temperature measurements challenging, are still present. Combining hyperspectral imaging approach with the QR sensors as done in this work eliminates both the optical resolution and device dependent calibration challenge, as will be explained and demonstrated in the following sub-chapters.

4.2 Experimental set-up

HQTI relies on probing the red shifted peak emission wavelength of QRs with the increase in temperature. This is due to the decrease in band gap. The band gap decreases due to the increase in inter-atomic distance with temperature and the corresponding decrease in the potential seen by the electrons. In order to excite the QRs, a light source, which is above the band gap of QRs, is used. One consideration during temperature measurements is that the device/material system under test needs to be unaffected by this light source due to the photo-current generation or optical heating due to absorption of the excitation light source. Therefore, the excitation light used in the set-up was selected to be below the band gap of wide band gap materials tested in this work, which is 3.4 eV for GaN, corresponding to an absorption wavelength of ~365 nm.

A Leica DMLM microscope was modified for the HQTI set-up as shown in Figure 4.1. The

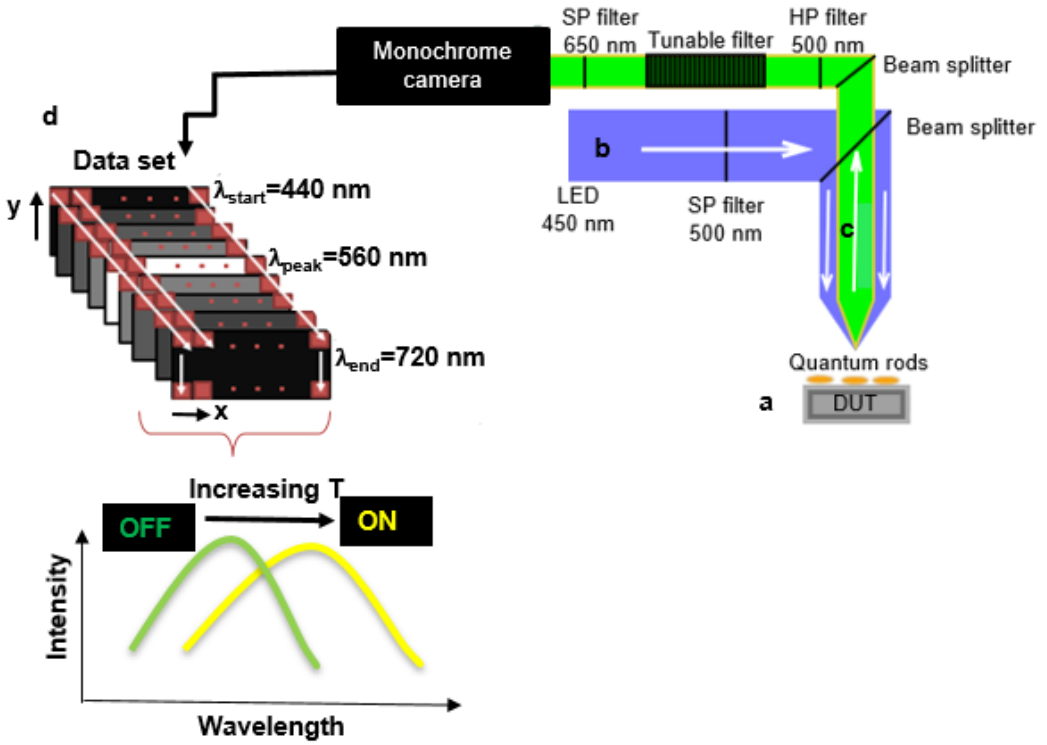

FIGURE 4.1. The schematic of the test set-up: (a) Quantum rods (QRs) are drop-casted on the device under test (DUT). (b) QRs are excited with the above band gap, 450 nm LED. (c) The photoluminescence (PL) spectrum of the QRs is obtained by sweeping the tunable filter.(d) The monochrome image at each particular wavelength, covering the PL spectrum, is collected for both ON and the reference (Pinched-OFF) state is collected.

original microscope light source was replaced by a multi-LED source, which consists of two high power LEDs, emitting in the white and the blue spectrum range for viewing the sample and for the excitation of the quantum rods (QRs), respectively. A white LED (Thorlabs MWWHL4) and a blue LED (Thorlabs M450LP1, 450±20 nm, 1850 mW) were mounted perpendicular to each other on the lower arm of the microscope. The light is directed to the optical path in the lower arm by a long-pass 490 nm cut on dichroic mirror (Thorlabs DMLP490R). The optical power of the blue LED reaching the sample surface, after the optical losses in the microscope, was measured as 25 mW, with a 1 mm diameter spot size. The emitted photoluminescent (PL) light was collected by a 16-bit monochrome CMOS camera (Thorlabs CS2100-M USB 3.0) mounted on the upper arm of the microscope. The field of view is ≈ 130 μm x175 μm with a Leica infinity corrected, 50x, 0.5NA objective lens, corresponding to a heat flux of 0.032 W/mm^2 on the sample.

Considering the worst-case scenario, assuming that all of the incident power is absorbed by the QR layer and not reflected or scattered, optical heating of the surface would be less than ≈ 0.013 W/mm^2. This is because for the QE of 60%, 40% of the absorbed light would be released as heat by the QRs due to non-radiative recombinations while 60% would be emitted as light. In fact, a large proportion of the incident light is either reflected from the metal or transmitted through transparent regions, resulting in less than ≈ 0.013 W/mm^2 optical heat absorption on the sample. Including this additional upper limit heat load in the thermal simulations for the worst scenario resulted in less than $\approx 1^o$C temperature rise, which is not measurable, i.e. below the precision of the test set-up, and therefore negligible for the material system tested in this work, including the calibration sample. The optical power can always be tuned depending on the sample under test, to ensure that it has a negligible effect on the temperature measurements.

A 500 nm cut-off short-pass filter (Thorlabs FESH0500) was placed between the LED and the sample to block the portion of the light which is emitted from the LED in the QR emission range so that it does not interfere with the QR emission spectrum. A 500 nm high-pass filter (Thorlabs FELH0500) was placed between the DUT and the liquid crystal tunable filter (Thorlabs KURIOS-VB1/M 420-730 nm), which is mounted on the upper arm of the microscope, to block the LED light reflecting off the surface or the sub-surfaces (i.e. interference effects) of the DUT. The liquid crystal tunable filter (LCTF), which enables spectral imaging, consists of liquid crystals placed in between two polarizers [134]. The liquid crystals, which are long cigar shaped molecules whose physical properties are in between solids and liquids [135], are birefringent materials, meaning that their optical properties are anisotropic. This anisotropy manifests itself as varying refractive indices along its different axes, depending on the orientation of the molecules. Due to different refractive indices along different axes, the incoming light passing through LCTF travels at different speeds along different axes, depending on the anisotropy of the crystals, and a phase shift is introduced between the light components along different axes. As a result, one component is retarded with respect to the other one. This manifests itself as a change in polarization for the output light. The birefringence of the liquid crystals, and the corresponding retardance, can be tuned by manipulating the rotation of the molecules either with the application of electric field or temperature change. Since the refractive index, and thus the retardance, is wavelength dependent,

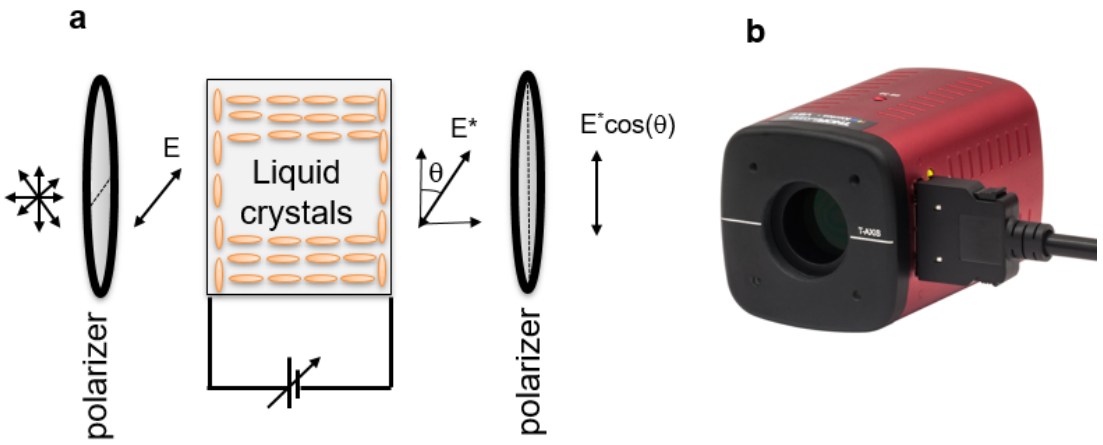

FIGURE 4.2. The schematic of the basic working principle and the image of the liquid crystal tunable filter used in this work: (a) The schematic of the basic working principle of a LCTF. Arrows represent the electric field, i.e. the polarization, of the input/output light. The dashed lines represent the transmission axis of the polarizers. (b) The image of the LCTF used in this work [134]

the wavelength of the transmitted light through the filter can be tuned with the application of the voltage. The second polarizer attenuates and rotates the incoming light, resulting in wavelength dependent intensity variation. A simplified schematic of a LCTF is shown in Figure 4.2 along with the image of the filter used in the experimental set-up. Depending on the application requirement, the design of the LCTF may include a series of the repeating configurations shown in Figure 4.2(a). The LCTF used in this work has three adjustable bandwidth settings: wide (≈ 15-50 nm), medium (≈ 10-25 nm) and narrow (≈ 5-10 nm). Narrow setting is useful for the applications where finer spectral resolution is required. In this work, wide setting is used due to its highest transmission ratio, improving the signal to noise ratio. The transmission properties of the band pass setting used in this work are shown in Figure 4.3. During the design of the set-up, it is important to consider that the intensity of the output light will always diminish as a LCTF configuration consists of polarization components, which absorb the out-of-axis portion of the incoming light.

It is critical that the probed signal in the experimental set-up solely originates from the temperature dependent emission of the QRs for a reliable and accurate measurement. In general, at the low excitation light intensity levels applied in this work, the optical processes and material

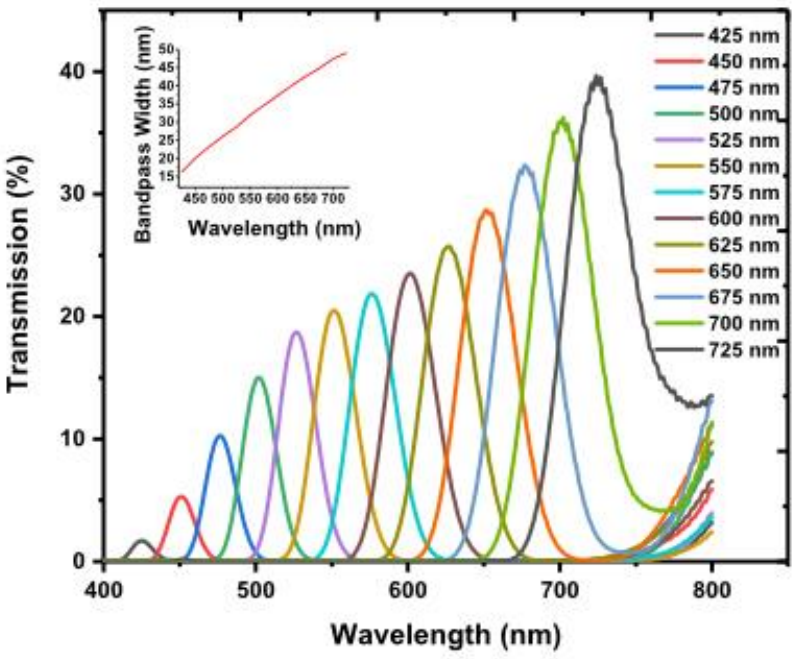

FIGURE 4.3. The transmission properties of the liquid crystal tunable filter(LCTF) used in this work (Re-generated from the data sheet). The LCTF consists of three settings with varying bandwidths: wide,medium,narrow. The inset shows the wide setting used in this work, due to its higher light throughput, increasing the signal to noise ratio (SNR).

interactions manifested in the measured signal could include : (1) Linear optical effects, including transmission, reflection and interference. (2) Absorption. (3) Inelastic scattering processes such as Raman scattering. (4) Luminescence. The effects of the first two processes on the measured signal were eliminated by implementing cut-off filters and minimizing the LED power reaching on the sample, respectively, as discussed previously. As explained in Chapter 3.1, the third process, Raman scattering, is a weak process and only $\approx 1/10^6$ of the incoming photons scatter inelastically [109]. Therefore, the implication of Raman effect on the spectrum will be negligible and manifests itself in the form of the noise in the baseline of the spectrum. The fourth process, luminescence, can be in the form of photoluminescence (PL) or electroluminescence (EL). As discussed previously, the band gap of the excitation power was selected to be below the band gap of the material system (AlGaN/GaN) tested in this work so that the PL signal other than the QR emission is eliminated. Electroluminescence (EL) is a phenomenon observed when the device is

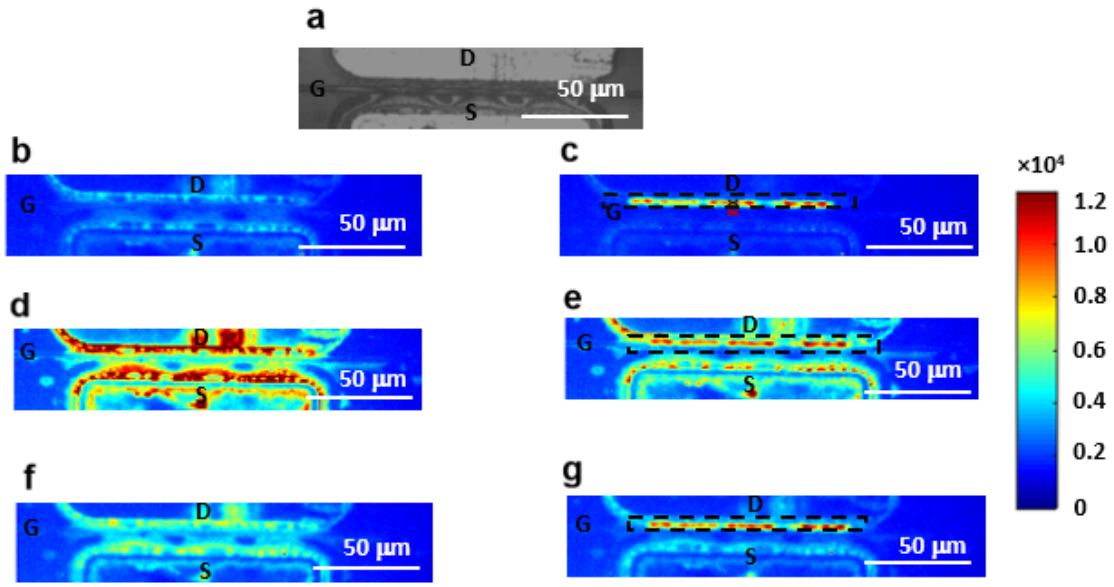

FIGURE 4.4. Emission images of the QR deposited test structure where electroluminescence is observed. (a) Optical image of the test structure. OFF state images at (b) 500 nm, (d) 560 nm,(f) 650 nm, ON state (V_{ds}=40V, I_{ds}=17.8 mA, V_{gs}=-2.3 V) images at (c) 500 nm, (e) 560 nm,(g) 650 nm.

operated under high voltage and high current, the origin of which on AlGaN/GaN devices was recently shown to be dominantly due to Bremsstrahlung (breaking radiation) mechanism [136]. The emission images of a QR deposited test structure under the blue excitation light at the ON (V_{ds}=40V, I_{ds}=17.8 mA, V_{gs}=-2.3 V) and OFF states are shown in Figure 4.4. The images on the left column show OFF state emission where those on the right column show the images at the ON state. The PL spectrum of CdSe/CdS quantum rods is expected to follow a Gaussian-like shape [137]. Figure 4.4. shows that the peak PL intensity is observed at the maximum emission wavelength of CdSe/CdS quantum rods for the OFF state images, as expected. On the other hand, there is a dominant emission near gate and drain, where the highest electric field is expected,at all spectral bandwidths for the ON state images. This indicates that the EL signal is dominant over the PL emission of QRs at higher bias. This EL signal needs to be decoupled from the QR photoluminescence to be able to probe temperature at those regions. The dominant EL emission wavelength needs to be known to decouple its effect from the total signal measured.

The EL emission spectrum at the visible wavelength range, which is of concern in this work, can simply be estimated for different material systems from the following equation:

$$I_{EL}(E_{h\nu}) \approx exp(\frac{-E_{h\nu}}{k_b(T_{el} - T_{latt})}) \tag{4.1}$$

once the electron and lattice temperature are known [138]. The lattice temperature can simply be estimated from thermal simulations by solving Fourier equation for the upper limit of the bias conditions. Electron temperature, which represents the average energy of the electron, can be approximated by solving hydrodynamic drift-diffusion equations under simplifying assumptions such as neglecting impact ionization or other energy decay mechanisms [139]. It is important to note that Equation 4.1 is not the Bremsstrahlung equation and that for the electron temperature extraction, the Bremsstrahlung equation would give a more accurate estimation [136]. However, for our purposes here, Equation 4.1 gives a reasonable estimation of the EL emission at the visible wavelength range. We also note that EL intensity scales up with the bias [136]. Before the design of the set-up, Eqn.4.1 can be used to estimate the EL spectrum for different material systems and appropriate filter can be selected accordingly to block EL emission reaching the detector so that only the temperature dependent QR signal is probed. However, it is more straightforward and sensible to measure the contribution of the EL spectrum to the QR emission spectrum on the test set-up and make the necessary corrections on the spectrum to ensure that the measured HQTI spectrum is solely due to QR emission. This verification can be done by simply turning the LED OFF when the device is biased and measuring the EL spectrum with the hyperspectral camera.

As shown before by Brazzini *et al.* (2016), the dominant EL emission for AlGaN/GaN material systems is observed in the near infrared region [136]. Therefore, a 650 nm short pass filter (Thorlabs FES0650) was placed in front of the detector to eliminate the EL signal interfering with the QR emission in our set-up.

PL emission curves of the QR coated device were obtained by sweeping the liquid crystal tunable filter from 440 to 720 nm with a 10 nm step. We note that the selection of the wavelength sampling requires consideration to avoid aliasing. Nyquist-Shannon sampling theorem, which forms the foundations of the digital signal processing, states that a signal can be perfectly reconstructed if the sampling frequency is at least twice as high as the maximum signal frequency [140]. Therefore, considering ≈ 20-50 nm bandwidth of the wide setting used for the measured

wavelength interval of 440-720 nm, a step size of 10 nm, which is equal to the half of the minimum bandwidth size, was selected following Nyquist-Shannon sampling theorem to avoid aliasing. 16-bit, 1040x1392 pixel, monochrome images were recorded to detect emission from the field of view at each measurement wavelength. A Leica, infinity corrected, 50x, 0.5NA objective lens was used to achieve sub-micron optical resolution and light throughput, which increases the signal-to-noise ratio (SNR). SNR is defined here as the ratio of the maximum emission intensity to the baseline of the spectrum at a particular pixel. In order to improve SNR further and reduce computational burden for image reconstruction, the images were binned by 2x2 using MATLAB built-in image resizing function, i.e. imresize, and image size reduced to 520x696 pixels. The pixel resolution for this configuration is approximately 180 nm, which also satisfies the sampling theorem requirements considering the diffration limited optical resolution of the test set-up.

The spatial resolution of the proposed technique is determined by the diffraction limit, unless individual quantum rods can be resolved. The theoretical optical resolution of the test set-up can be estimated by Sparrow criterion, which defines the resolution as the distance between the two incoherent point sources where the first and second derivative of their combined point spread function (PSF) is equal to zero [135, 141]. The Sparrow criterion is given by:

$$d = \frac{0.47\lambda}{NA} \tag{4.2}$$

where λ is the peak emission wavelength, which is approximately 600 nm over the measured the temperature range, and NA is the numerical aperture of the objective lens (=0.5 here). According to this criterion, the estimated theoretical resolution of the set-up is $\approx$ 600 nm. This theoretical resolution can be verified either by a well-established knife-edge technique or by measuring the PSF of a point light source, such as a quantum dot. In this work, the former approach was adopted by measuring line spread function (LSF) of the imaging system [142] due to its relative simplicity in terms of sample preparation.

A sample, with a sharp discontinuity from a reflective (metal coated) area to a transmissive (semiconductor) area, was imaged under white light illumination. This sample approximates a step function very well, with a much smaller transition length compared to the measurement wavelength, as illustrated in the AFM scan in Figure 4.5(a).

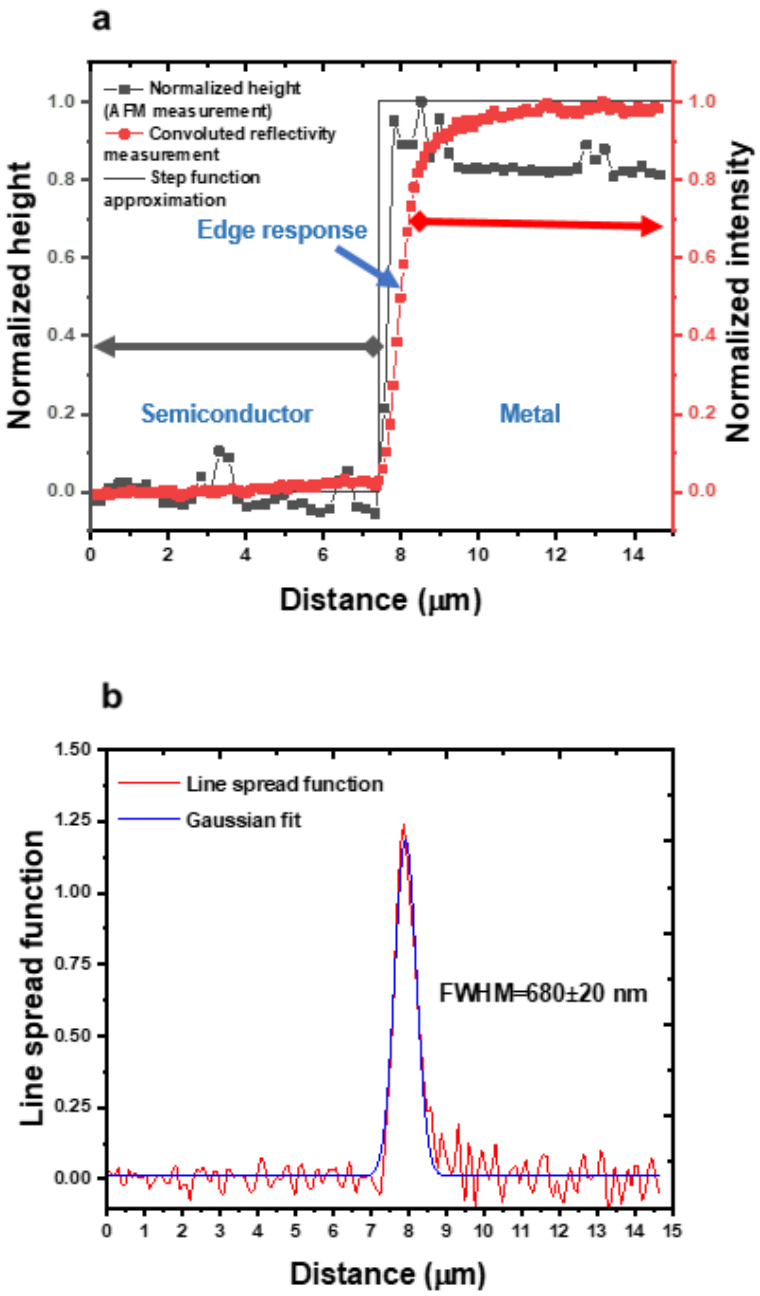

FIGURE 4.5. Optical resolution measurement: (a) The line step response measurement of the imaging set-up using knife edge technique. (b) The line spread function of the imaging set-up.

The liquid crystal tunable filter was set to the maximum emission wavelength of the quantum rods (560 nm). The measured response, shown as the red curve in Figure 4.5(a), is the convolution of the LSF and the actual object, which is mathematically given as [135]:

$$g(X) = \int_{-\infty}^{\infty} f(x)h(X-x)dx \tag{4.3}$$

where $g(X)$ is the measured image intensity, i.e.the convoluted response, $f(x)$ is the actual object, i.e. actual line profile, and $h(X-x)$ is the line spread function (LSF). When $f(x)$ is a step function, the first derivative of the measured intensity distribution, i.e. $g(X)$, gives the LSF profile as shown in Figure 4.5(b). The full width at the half maximum (FWHM) of the Gaussian function fitted to LSF with 0.94 R-square value, is 680 ± 20 nm. The measured optical resolution of the imaging system is therefore within 12% of the theoretical estimate of 600 nm. We note that the estimated optical resolution in this work does not correspond to the spatial thermal resolution as described by thermal imaging standards. ASTM defines a parameter called minimum resolvable temperature difference (MRTD) to compare the performance of different thermal imaging systems (mostly for IR thermal imaging systems) [143]. This standard requires a fabrication of a four bar target on a blackbody background, as shown in Figure 4.6. The temperature of the target is slowly decreased down to the background (ambient) temperature and the temperature difference just before the image of the bars disappears is stated as the MRTD. MRTD tests are performed by varying the spacing between the individual bars and this value is reported along with the spatial frequency of the bars. The smaller the reported value, the higher the spatial temperature resolution of the system. As this work is conducted within the academic setting on a proof-of-the-concept set-up, this parameter, which is of concern in the commercial setting, was not reported here. Yet, it is important to be aware of this standard to compare the technique with the existing technologies as this work is under consideration for commercialization, despite the fact that this standard is questionable in terms of the objectivity and reliability of the test as it requires an observer to assess temperature evolution of the images.

System calibration was performed by drop casting QRs onto a piece of silicon, which was mounted on a Linkam TMS600 cryostat. StremDots™ Series A Plus CdSe/CdS colloidal quantum rods suspended in hexane (size: dia.3-5 nm x length 15-20 nm) with the peak emission range

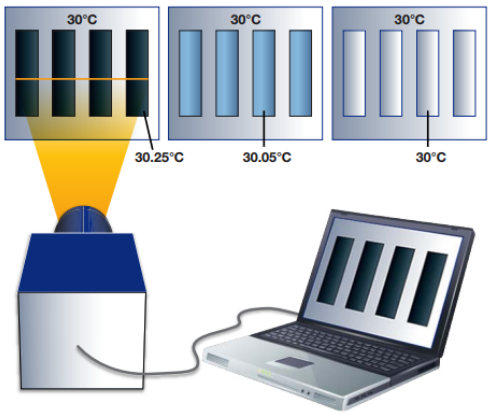

FIGURE 4.6. MRTD test set-up. Figure originally published in Ref [144].

of 560 ± 8 nm specified in the data sheet were used in this work. The concentration of 5 mg/ml was diluted to ~1.5 mg/ml and sonicated for one hour at the room temperature to prevent agglomeration of particles and achieve a distribution as uniform as possible first in the solution and eventually on the calibration sample (and the DUT). After cleaning the calibration sample with isopropyl alcohol (IPA) and acetone, the surface of the wafer was treated with Ar plasma (Diener Electronic Zepto) for 1 minute at 0.4 mbar to ensure the removal of the contaminants on the surface, if any, prior to QR coating.≈10 μl of solvent was drop cast onto the region of interest in the wafer placed on a hot plate heated above the boiling point of hexane at 100 ^{o}C. The emission images are shown in Figure 4.7. The QR peak emission wavelength was estimated by averaging the intensity across the full FOV at each bandwidth, over a range of temperatures from 25 ^{o}C to 155 ^{o}C .

Image drift due to thermal expansion and SNR are two important criteria for accurate sub-micron level optical temperature measurements for all thermography techniques, for two reasons: First, thermal gradients in the region of interest (ROI) might change significantly depending on the geometry and bias conditions of the DUT; therefore, the resulting image drift might lead to erroneous temperature estimations due to the change in reference and biased positions. In addition to this, the band gap of the nano particles might vary due to the variations of the size of QR batch deposited on the DUT [137]. Yet, the thermal response of the band gap shift is identical even when the size of the QRs, and the corresponding band gap, varies [137].

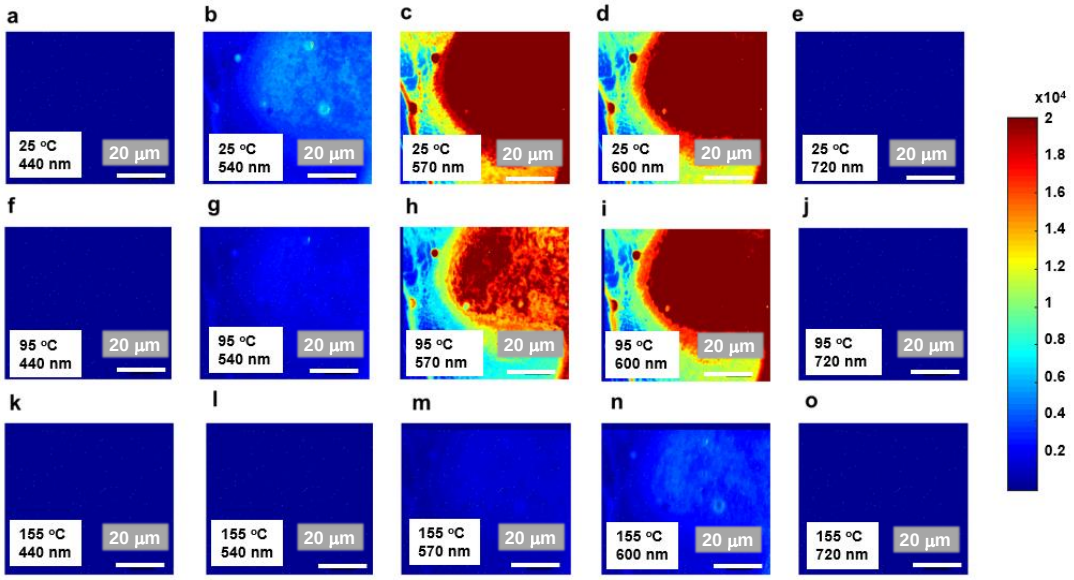

FIGURE 4.7. The emission images of the calibration sample (QRs drop casted on a Si piece) from 440-720 nm: (a)-(e) at 25^{o}C (f)-(j) at 95^{o}C (k)-(o) at 155^{o}C.

However, the image drift might result in measurement artefacts mostly resulting from the spatial variation in intensity measurements. Thermal expansion can cause axial and lateral drift of the sample. In order to correct for the focal plane change due to the axial drift and the lateral drift, especially during the calibration process where the thermal expansion of the hot stage is non-negligible, the sample position was automatically corrected in the *x-y* and *z* directions using a computer controlled *xyz* stage with 100 nm step precision and an in-house developed LabVIEW software, which was developed by a former postdoctoral research associate in our group, Dr. Mirko Bernardoni, and Dr. James W. Pomeroy. The software first corrects for the focal plane change by moving the sample stage in the *z* direction until the image intensity is the highest. Then, the *x-y* drift is corrected within 1 pixel by moving the stage so that the difference between the total intensity of a white light illuminated live image and the total intensity of a reference image previously recorded is minimized. This procedure was run each time after the hot stage temperature was changed, during the calibration. The sample drift was only found to be significant during the calibration rather than the actual device measurement, because the heated volume in the hot stage is much larger than that of the actual measured device during operation, which is mounted on a thermal vacuum chuck at a fixed temperature.

An image registration method, which is based on so-called "single-step discrete Fourier Transform (DFT)" [145], was also implemented after the calibration measurement to ensure the *x-y* drift correction and the accuracy of the calibration because the stage correction in the *x-y* direction was observed not to be always satisfactory if there are no distinct geometrical features in the field of view. The image reconstruction was performed by minimizing the metric defined as normalized root mean square error (NRMSE), E, between the drifted image, $g(x, y)$, and the reference image, $f(x, y)$. NRMSE is defined by [145]:

$$\begin{aligned} E^2 &= \min_{\alpha,x_0,y_0} \frac{\sum_{x,y} |\alpha g(x-x_0, y-y_0) - f(x,y)|^2}{\sum_{x,y} |f(x,y)|^2} \\ &= 1 - \frac{\max_{x_0,y_0} |r_{fg}(x_0,y_0)|^2}{\sum_{x,y} |f(x,y)|^2 \sum_{x,y} |g(x,y)|^2} \end{aligned} \tag{4.4}$$

where α is an arbitrary constant, x_0 and y_0 are the global coordinate transformations. The summations are taken over all image pixels (*x,y*). r_{fg} is the cross correlation of the drifted and the reference image, and is given by:

$$\begin{aligned} r_{fg}(x_0,y_0) &= \sum_{x,y} f(x,y) g^*(x-x_0, y-y_0) \\ &= \sum_{x,y} F(u,v) G^*(u,v) exp\left[i2\pi \left(\frac{ux_0}{M} \right) + \left(\frac{vy_0}{N} \right) \right] \end{aligned} \tag{4.5}$$

where N and M are the image dimensions and (*) denotes the complex conjugate pair. Uppercase letters represent DFT of the corresponding functions with the lowercase letters. DFT of the function $f(x,y)$ is given by:

$$F(u,v) = \sum_{x,y} \frac{f(x,y)}{\sqrt{MN}} exp\left[-i2\pi \left(\frac{ux}{M} \right) + \left(\frac{vy}{N} \right) \right] \tag{4.6}$$

The objective function given by Equation 4.4 is minimized with respect to α. This requires maximizing the cross correlation $r_{fg}(x,y)$. This is essentially an application of the non-linear optimization. The "single-step DFT" algorithm estimates the initial guess first by calculating $F(u, v)$ and $G^*(u, v)$ by Fast Fourier Transform (FFT) and then using this initial guess to fine-tune the pixel shift search. This fine tuning is achieved by looking for the maximum of the cross correlation

function in a 1.5x1.5 pixel neighborhood around the initial guess by calculating matrix multiplied DFT of $F(u, v)$ and $G^*(u, v)$. This fine tuning step using DFT decreases the computational cost compared to calculating conventional zero-padded FFT by decreasing the matrix size.

The algorithm found that the image drift, at temperatures below 125^{o}C, was in the range of 1-15 pixels for the raw image (unbinned image), for which 1 pixel corresponds to 90 nm, whereas at temperatures above 125^{o}C, the image shift was found to be up to 40-45 pixels. The effect of the x-y drift correction by image registration (which is within 1 pixel) on the calibration data is shown in Figure 4.8. It is clear that the x-y drift is significant only at higher temperatures due to higher thermal expansion and indicates that in-situ stage drift correction is satisfactory enough. However, image registration needs to be considered if the drift at higher temperatures exceeds 5 μm during the calibration.

The Varshni equation is a widely used empirical formula, which relates band gap change (or wavelength shift) of QRs to temperature as described in Chapter 2.2. At temperatures above 200 K , a linear relationship can be approximated between the wavelength shift and temperature according to Varshni equation. Figure 4.9(a) shows that the peak emission wavelength shift of QRs with respect to the temperature change is non-linear when measured using our test set-up. The error bars in the data represent standard error of the mean of peak position estimations (n=5

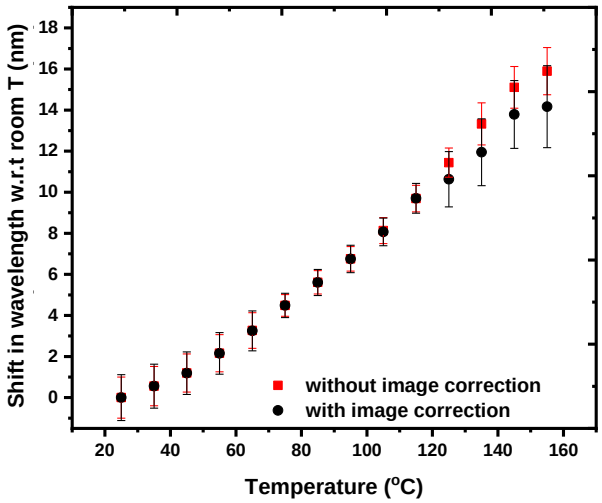

FIGURE 4.8. Temperature calibration function with and without image correction, indicating that x-y drift is more significant at higher temperatures due to thermal expansion.

successive measurements for the data presented), which are associated with the random errors in the measurement itself and also with the fitting errors in the peak position fitting (The discussion of the effect of the calibration-related uncertainties on the temperature measurements is given in Appendix A.). The non-linear dependence on the temperature is attributed to the QR emission being convoluted with the spectral response of the optical measurement system considering that the tunable liquid crystal filter transmission and camera sensitivity are wavelength dependent. The actual QR emission spectrum could be obtained by deconvoluting the measured spectrum from the optical response. Yet, for the sake of computational simplicity, a quadratic function, which includes the system response in the calibration, was fitted to the data here, with an R-square value of 0.999. The calibrated emission wavelength temperature dependence is ~1.15 nm shift per 10^oC at ambient temperature, where the fitting is a quadratic function:

$$\Delta\lambda_{cw} = \alpha T + \beta T^2 \tag{4.7}$$

where α=0.072±0.0036 nm/^oC, β=3.48x10-4 ±4.21 x 10-5 nm/(^oC)^2. Figure 4.9(a) illustrates that the measured QR emission wavelength temperature dependency is similar to reported values for small (2.2 nm) and medium sized (3.8x3.6 nm) QR cores up to 100^oC [137]. The slight discrepancy between the measured and reported wavelength shift at higher temperatures could be due to the response of the optical measurement system and the slight differences between the morphology of the quantum rods used in this work and in Ref. [137]. Once the QR band gap shift response for a particular optical set-up is known, any wide band gap device system can be tested without further calibration with this approach, only with small modifications in the system parameters (which could include LED power tuning to prevent heat absorption and implementation of the suitable EL cut-off filters, if required, depending on the device system tested and particular bias conditions). Therefore, one can clearly state that our approach requires only one-off calibration, which is independent of the particular device tested and is only equipment dependent. Once the calibration function is known, peak positions at the ON and pinched-OFF (reference) states of the DUT were related to temperature of the quantum rods, which represents "effective" surface temperature of the DUT.

Figure 4.9(b) shows emission curves for the ON and pinched-OFF state of a GaN HEMT

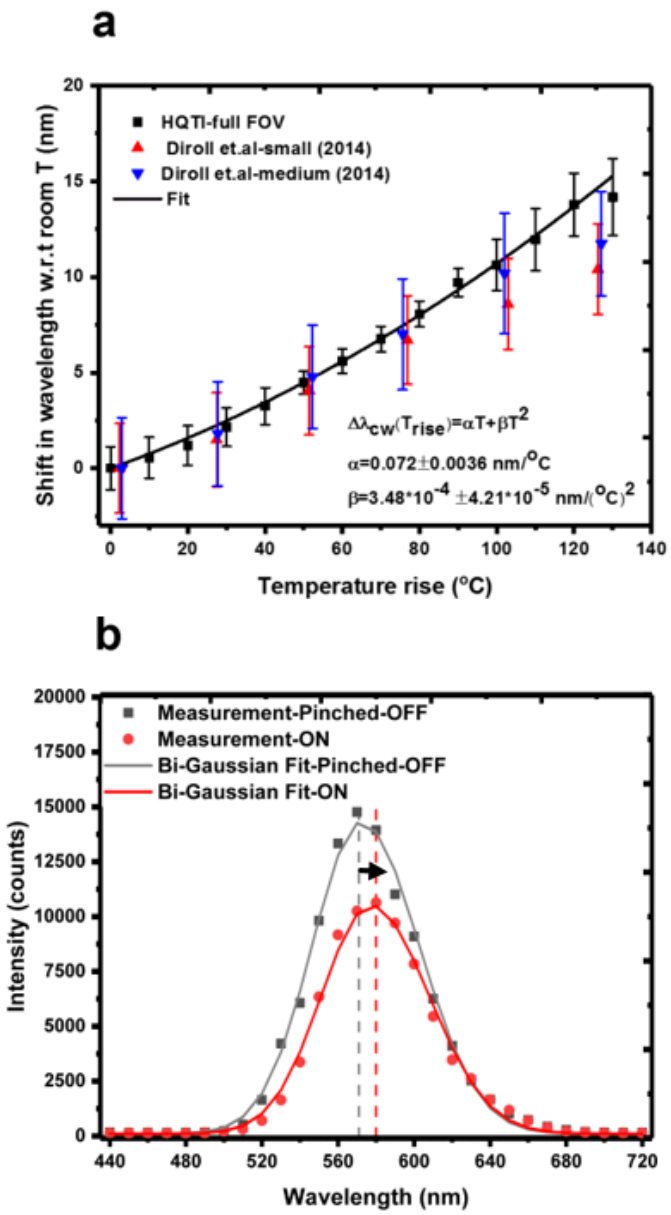

FIGURE 4.9. Temperature calibration of the QRs deposited on a Si piece and a sample spectrum when DUT is operated : (a) Centre (peak emission) wavelength vs. temperature relation. Literature data are overlaid for comparison. (b) Sample measured spectrum of the DUT at the ON and Pinched-OFF state fitted Bi-Gaussian function to extract the peak position. Arrow indicating the red shift of the QR response at higher temperatures.

and the corresponding emission peak centre fitting function. The emission spectrum follows a Bi-Gaussian shape. In the literature, this inhomogeneous broadening observed in the PL spectra of the ensemble of the semiconductor nanorods is attributed to the size [146–150] and morphology [148, 150] variations within the ensemble and, to some extent, the impurities and the surface charges [146]. In our system, the optical response of the tunable filter, the transmission ratio of which increases with the increasing wavelength, could also contribute to this spectral shape. While this inhomogenous broadening might be undesirable for opto-electronic device applications, where the colour purity is desired, this does not have remarkable implications for the technique presented here. An example of the Bi-Gaussian function fitted to a pixel spectrum to determine the peak emission wavelength was shown in Figure 4.9(b). A least squares iterative algorithm results in fits with an R-squared value >0.95, for the spectra with an adequate SNR. The fitting routine is based on a built-in LabVIEW function, i.e. Levenberg-Marquardt bounded algorithm with user-defined initial guesses. As Figure 4.9(b) shows, the spectrum follow the expected trend, i.e., increasing emission wavelength and decreasing intensity, as the temperature rises [151]. At this point, the question of whether any non-ideality/non-uniformity in the optical path or the spatial/size distribution of QRs might require a pixel-by-pixel calibration might arise. In order to answer this question and verify the validity of the full FOV calibration approach,the calibration

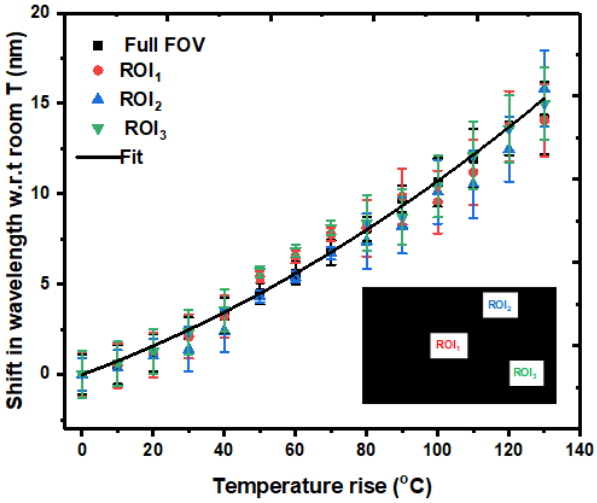

FIGURE 4.10. The verification of the full FOV calibration approach by investigating the calibration parameters across various ROIs by 50x50 pixel area. The inset shows the locations of the ROIs in the image.

function at various ROIs over an area of 50x50 pixels was extracted. The fit shown in Figure 4.10 is for the full FOV. The R-square value calculated for the 2nd order polynomial fits at each ROI is larger than 0.97, indicating that the emission wavelength shift with temperature is constant, within the measurement uncertainty, across the FOV. This confirms that the full FOV calibration is a valid approach and pixel by pixel correction is not required.

4.3 Device details and the effect of QR deposition on device performance

HQTI was demonstrated on a normally-OFF (enhancement mode) GaN-on-Si device on a six inch wafer supplied by Infineon Technologies. The devices are passivated with a 800 nm thick Si_xN_y and SiO_2 layer. A 80 nm thick AlGaN barrier was grown on a 750 nm GaN layer which is on top of a 3700 nm thick strain relief layer (SRL) and 700 μm thick Si substrate. The DUT is a single finger, field plated 200 μm wide device with 1.8 μm source-gate and 12 μm gate-drain distance. The gate foot to the field plate edge distance is 3 μm. The schematic of the device and its optical image is given in Figure 4.11.

StremDots™ Series A Plus CdSe/CdS colloidal quantum rods suspended in hexane (size:

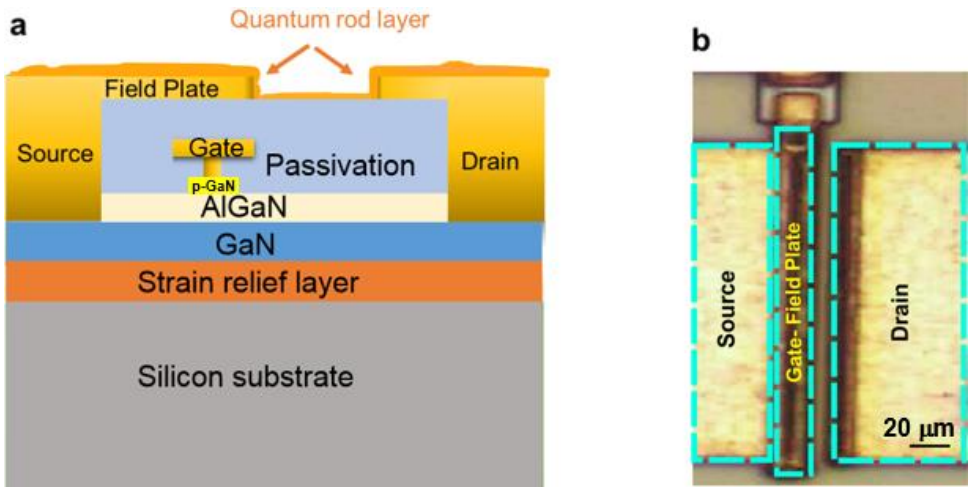

FIGURE 4.11. DUT details: (a) Schematic of the device cross-section (Not to scale.). (b) Optical image of the DUT.

dia.3-5 nm x length 15-20 nm) with the peak emission range of 560 ± 8 nm were used in this work. The concentration of 5 mg/ml was diluted to ~1. 5 mg/ml and sonicated for one hour at the room temperature to prevent agglomeration of particles and achieve a uniform distribution first in the solution and eventually on the DUT. After cleaning the wafer with isopropyl alcohol (IPA) and acetone, the surface of the wafer was treated with Ar plasma (Diener Electronic Zepto) for 1 minute at 0.4 mbar to ensure the removal of the contaminants on the surface, if any, prior to QR coating. ~10 μl of solvent was drop cast onto the region of interest in the wafer placed on a hot plate heated above the boiling point of hexane at 100 ^{o}C.

Figure 4.12 shows the SEM images of the QR distribution, which were taken with the help of Dr. Adel El-Turke. Unfortunately, the resolution was not high enough to observe single QRs. All that can be understood from SEM images is that the distribution is layer-like and there is no

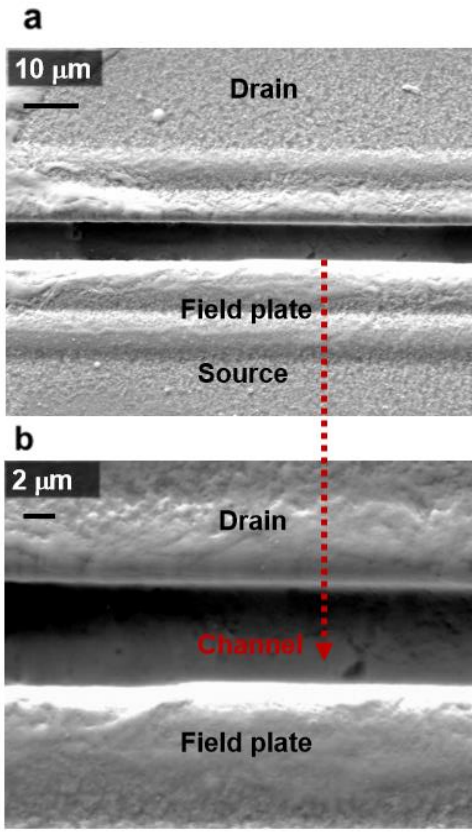

FIGURE 4.12. Sample SEM image of the QR deposited DUT. (a)Image showing the layer-like distribution on the device surface. (b) Magnified image showing that the clustering of the QRs is not observed in the channel with this resolution.

observable clustering with the available resolution.

The emission images obtained from the HQTI set-up shown in Figure 4.13 gives more insight in terms of QR distribution compared to SEM images. It is clear from the emission intensity maps that the distribution is non-uniform to some degree. This non-uniformity could have two implications on the temperature measurements: (1) The regions with the lower density of QRs give lower SNR, which might cause a difficulty for the signal reconstruction. (2) If it is too thick, it can affect the heat transfer, and therefore the "effective" value of the measured surface temperature. In terms of the thermal image reconstruction, this non-uniformity would not be detrimental if the signal to noise ratio remains above a threshold. The analysis shows that temperature values can be reconstructed at the all pixels in the ROI having a peak emission intensity higher than 350 counts per pixel.

It was shown that individual CdS nanowires have a low thermal conductivity, which is on the

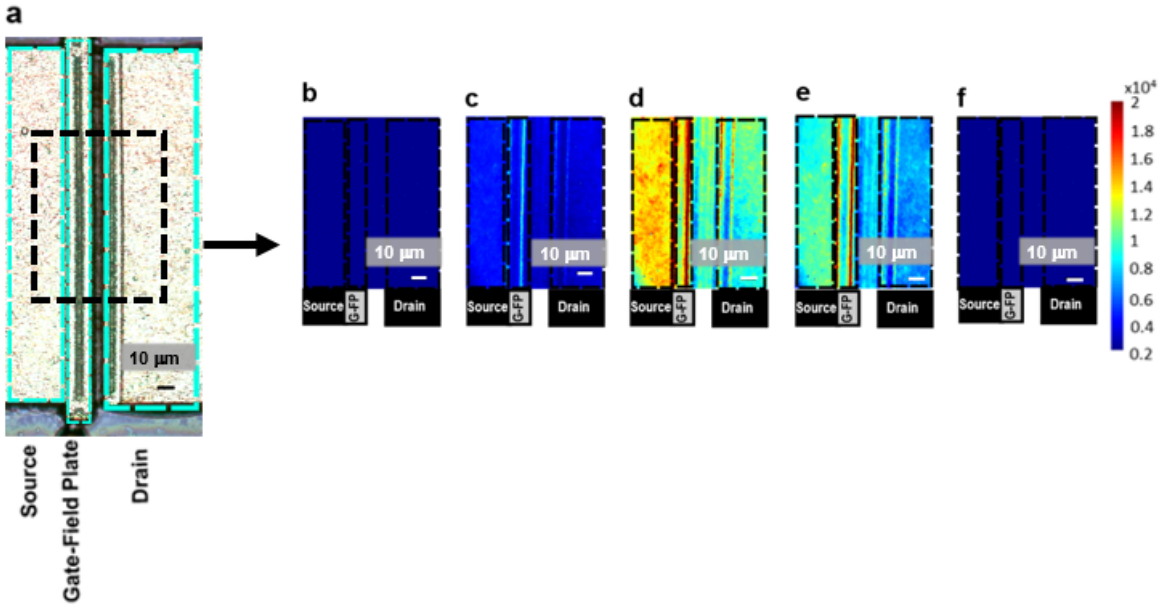

FIGURE 4.13. Sample emission intensity of QRs through the emission spectrum, at the region of interest (ROI) of the DUT. The images were recorded at the ON state with V_{ds}=10 V, I_{ds}=83.2 mA, P_{diss}=4.165 W/mm, $T_{backplate}$ =25^{o}C. (a) Optical image of the QR deposited DUT. The black dotted rectangle shows the ROI. The emission intensity of the monochrome images is shown at: (b) 440 nm (c) 540 nm (d) 570 nm (~ peak emission) (e) 600 nm (f) 720 nm. The integration time per image is 1200 ms.

order of < 10 W/mK [152], meaning that a too thick coating layer can decrease the heat flow from the channel. Besides, the increased heat capacity due to the coating thickness might increase the thermal time constant of the device. For these reasons, it is crucial to quantify the average thickness of the coating layer. In order to estimate the thickness of the QR layer on the heat transfer, AFM measurements were performed. The thickness of ~ 500 nm was measured at the edge of the deposition area, which is also called in the literature as "coffee ring edge" [153, 154], using an AFM as shown in Figure 4.14. This is the thickest region of the deposition where there is a visible accumulation of QRs and is the upper limit as the typical layer on the ROI is thinner. The effect of this on the heat transport for the steady state measurements was explored via thermal simulations and found to be negligible, i.e. below the precision of our measurements. The details are given in Chapter 4.5.

One obvious question is whether the deposition of QRs would alter the device characteristics. It is expected that properly passivated devices would be unaffected by the coating as the passivation layer isolates the channel from any outside charge flow. However, it is essential to ensure that the passivation layer is of good quality so that the device functions as designed. The output and transfer characteristics of the five sister devices, which were passivated, were tested before and after the deposition to verify that deposition of QRs is non-detrimental to the device characteristics, as shown in Figure 4.15. The linear region seems unaffected; however, ~ 0-7

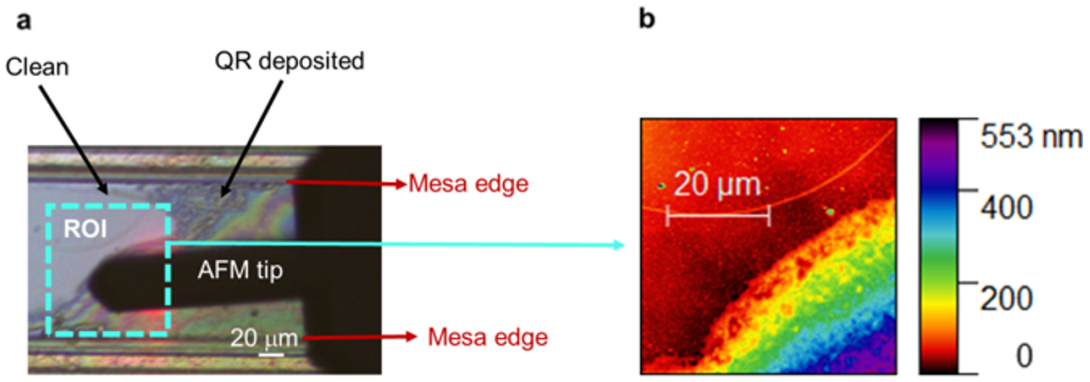

FIGURE 4.14. Thickness measurements with the AFM at the edge of the QR deposition.(a) Optical image of the ROI where the thickness of the deposition measured. (b) AFM thickness measurement of the ROI shown in (a),showing the maximum thickness of ~ 500 nm.

% variation in the output power in the saturation region at some gate biasing conditions were observed. This is less than the 10 % repeatability of the measurement. This confirms that the device characteristics was seemingly unaffected by the QR deposition.

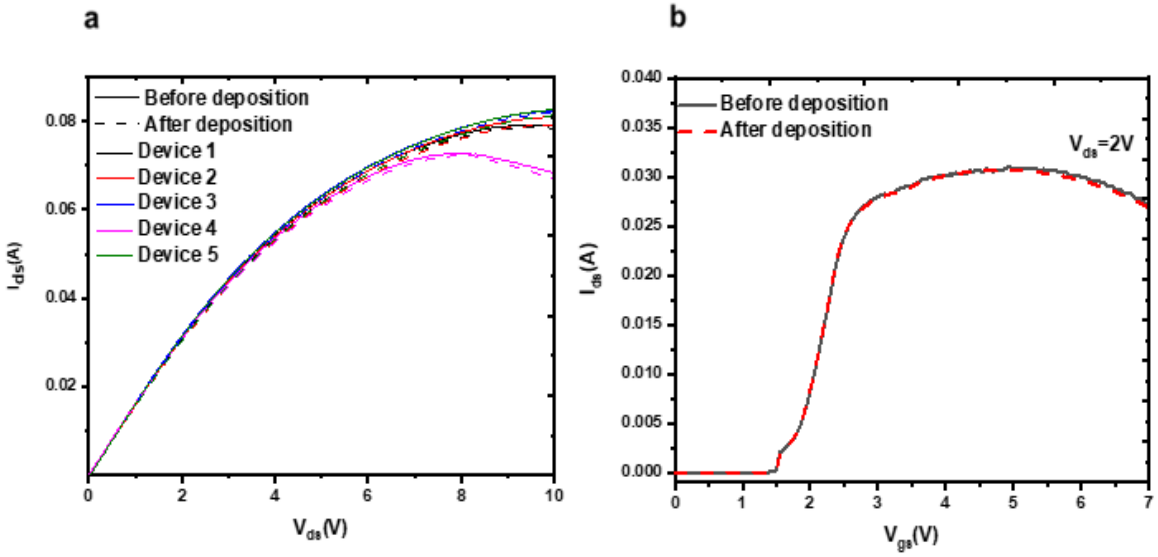

FIGURE 4.15. Transfer and output characteristics after quantum rod deposition. (a) Device output characteristics before/after measurements measured for the sister devices (single finger, field plated and passivated) on the same wafer supplied by Infineon Technologies, at V_{gs}=5 V. (b) Device transfer characteristics before/after deposition for the same devices in (a).

4.4 Image processing

The images were collected by automated LabVIEW software. The image processing algorithm flowchart is shown in Figure 4.16. The image processing software developed defines an intensity threshold of 500 counts and processes the pixels with the spectrum having the peak emission value larger than this threshold to ensure elimination of the noisy pixels and processing only the actual QR signal. This value was defined considering ~ 350 counts for the longest camera exposure time of 7765 ms at room temperature. The emission intensity distribution shown in Figure 4.13 illustrates that for the DUT, the signal is well above this threshold value. Hot pixels

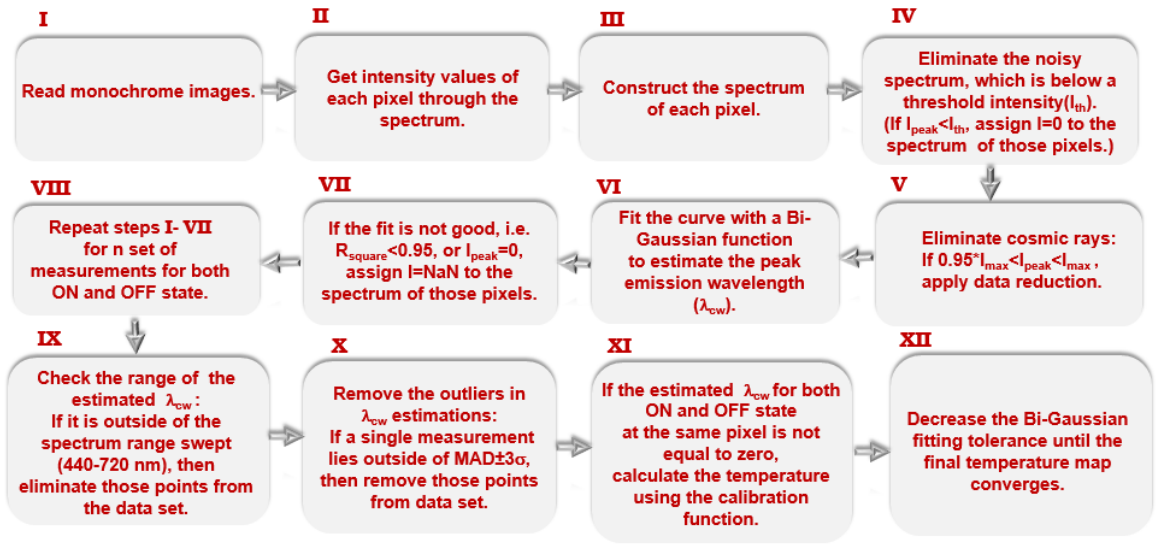

FIGURE 4.16. Image processing flowchart for temperature map reconstruction from emission images.

which could be observed due to cosmic rays or the imperfections of the detector such as leakage current were eliminated from each particular spectrum by defining a 95 % maximum intensity threshold, i.e. 0.95 of 2^{16} for the 16 bit camera used in this work. The resulting spectrum was fitted with a built-in nonlinear curve fitting function in LabVIEW with BiGaussian function. The tolerance of the fit was decreased until the temperature map converges numerically. This value is 10^{-2} here. The accuracy of the fitting was further confirmed with the Chi-squared test for each spectrum, giving R-square value of greater than 0.95. An additional condition was added to ensure the elimination of the inaccurate fittings by rejecting the peak position estimations falling outside the spectrum range swept, between 440-720 nm. This procedure was applied to each particular measurement at ON and the reference(pinched-OFF) state. Here it is applied for n=7 measurements. In order to increase the confidence on the estimated results and eliminate the random error in the measurements, the outliers in the successive measurements were removed by applying the mean absolute deviation (MAD) criterion [155], which is defined as:

$$MAD = bM_i(|\lambda_i - M_j(\lambda_j)|) \tag{4.8}$$

where λ_j represents n original wavelength estimations and M_j is the median of the wavelength estimations. The constant b is equal to 1.4826 for a Gaussian distribution assumption. The centre wavelength estimations outside the $M \pm 3MAD$ interval were eliminated from the data set. The MAD criterion is more effective than the mean$\pm 3\sigma$ criterion as the latter is also affected by outliers, which could be problematic for small sample sets.

The pixels identified as an outlier were assigned a zero value. Temperature is calculated at the pixels where the peak position was estimated as non-zero for both ON and the reference state using the calibration function. Otherwise, the temperature was assigned NaN there. Temperature precision was quantified by the standard error of the mean of successive measurements, which is highly dependent on the fitting accuracy. The system was tested by measuring a device held at 25^{o}C, without heating. The histogram of the estimated temperature map over the whole FOV for n=3 measurements is shown in Figure 4.17. Kernel distribution fitted to the histogram gives 20$\pm$8^{o}C population mean temperature, covering the fixed temperature of 25^{o}C and indicating the reliability of the system developed. More details on the error analysis are given in Appendix A.

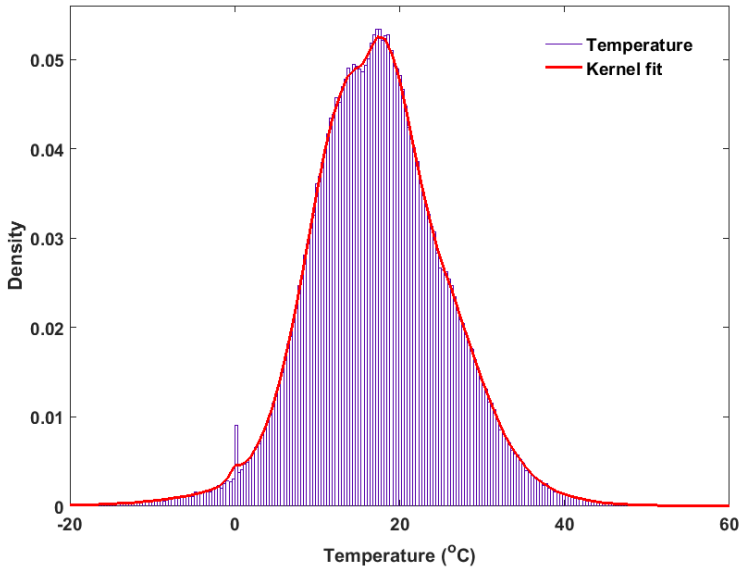

FIGURE 4.17. Kernel fit to the reconstructed temperature map on a DUT held at 25^{o}C. The density on the y axis represents the ratio of the number of the pixels showing a particular temperature with respect to the total number in a single 520x696 pixel image.

4.5 Results and Discussion

The enhancement mode single finger GaN HEMT measured on a wafer was fixed on a thermoelectric vacuum chuck and tested at three different bias conditions to demonstrate the feasibility of the HQTI technique. The chuck temperature was set to 25^{o}C and the total power dissipation was varied from 0 to 0.83 W, by changing drain bias at a constant gate bias of V_{gs}=5 V while I_{gs}=0.01 A.The pinch-OFF condition was used as a reference measurement, by applying V_{gs}=0 V at the same drain bias with the ON state, so that no drain current flows and the device is at the ambient chuck temperature. Figure 4.18(b)-(d) shows HQTI temperature maps at varying power dissipation levels. The results, which represent the mean of n=7 measurements (Please see Appendix A for sample images obtained by a single acquisition.), are as expected qualitatively: The channel region, where Joule heating is generated, is hotter than the surrounding contacts, where the heat diffuses. HQTI temperature measurements also increase with power dissipation in the expected way. The measurements show no hot spots and no steep temperature gradients, giving a fairly uniform temperature distribution in the channel. The measurements also suggest that the source contact has slightly higher resistance than that of the drain contact, which manifests itself as a higher temperature rise.

IR measurements were performed on the same device and at the same power dissipation levels as those of HQTI measurements to verify HQTI results. As the thermal radiation increases with temperature following Planck's law, the back plate temperature was set to 52^{o}C to increase SNR. The drain bias was increased to compensate for the drain current reduction at the higher ambient temperature, keeping gate bias the same as HQTI measurements. A 15x, 0.5NA lens was used for IR thermography measurements, giving ≈3-6 μm lateral optical resolution according to Sparrow criterion. IR thermography measurements shown in Figure 4.18 (e)-(f) also reveals the uniformity between the gate and the drain contacts. The source contact temperature is also found to be higher than that of the drain contact, as in HQTI measurements. IR thermography is a useful technique for the qualitative assessment of any irregularities in the device such as hot spots. However, it needs to be interpreted carefully when compared to the HQTI temperature map. IR thermography underestimates temperature rise in the active region of the device by up to ~50% because of

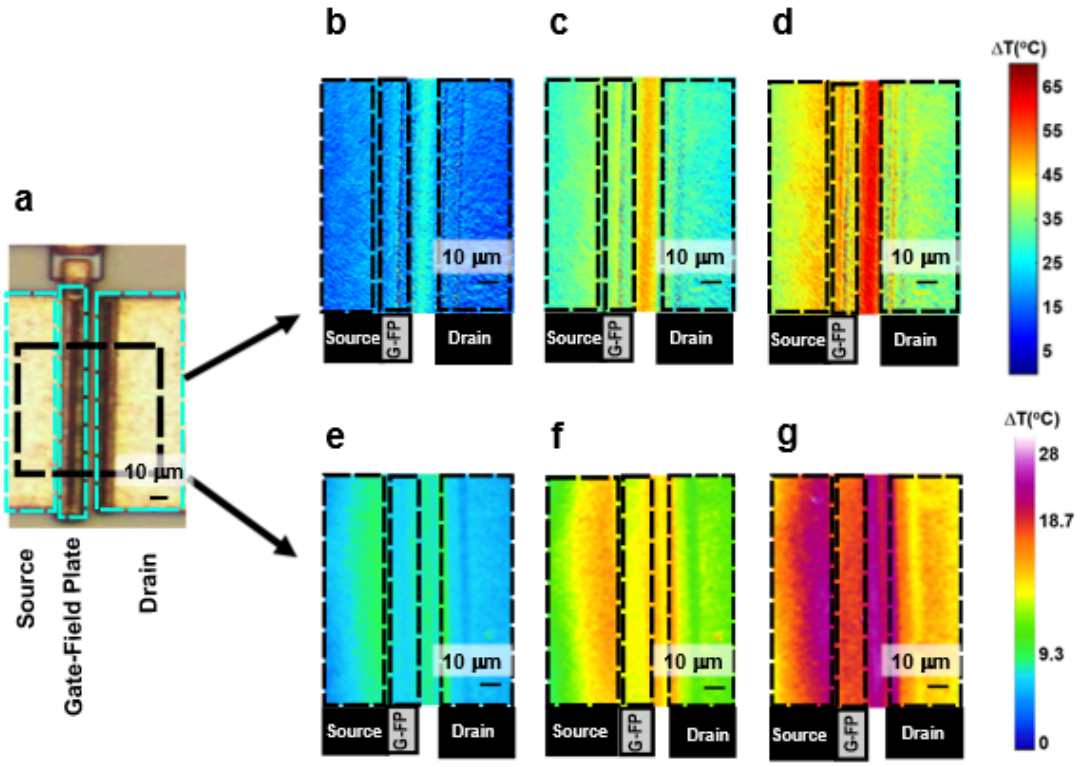

FIGURE 4.18. Temperature rise vs P_{diss} maps in the ROI. (a) Optical image of the DUT. Black rectangle shows the ROI. Temperature maps of the ROI with HQTI at 25^{o}C back plate temperature: at (b)V_{ds}=5 V, I_{ds}=62.5 mA, P_{diss}=1.56 W/mm (c) V_{ds}=8 V, I_{ds}=78.6 mA, P_{diss}=3.145 W/mm (d) V_{ds}=10 V, I_{ds}=83.2 mA, P_{diss}=4.165 W/mm; with a lower spatial resolution IR thermography at 52^{o}C back plate temperature (e)V_{ds}=5.7 V, I_{ds}=55.2 mA, P_{diss}=1.57 W/mm (f)V_{ds}=8.9 V, I_{ds}=69.5 mA, P_{diss}=3.1 W/mm(g) V_{ds}=11.3 V, I_{ds}=73.8 mA, P_{diss}=4.17 W/mm.

lateral (due to IR wavelength diffraction limit) and axial (due to semiconductor IR transparency and reflections from the interfaces) spatial averaging [156, 157]. This underestimation, which is more than 50%, is also evident in our findings shown in Figure 4.18.

While IR thermography results are useful for a first assesment, a more accurate method is required to ensure the reliability of the HQTI results. In order to evaluate the accuracy of the new technique, a finite element method (FEM) device thermal model was built using realistic material properties. Thermal properties of the device layers to be used in the simulations, such as GaN, Si and passivation layers are fairly well-established, considering almost two decades of extensive GaN research. The most processing dependent parameter is the strain relief layer (SRL), the recipe of which can vary depending on the supplier. Usually, step-graded AlGaN or

superlattice of AlN/GaN is grown to compensate for the lattice mismatch of Si and GaN layers [16] and has a thermal conductivity on the order of tens of W/mK [158]. The thermal conductivity of the SRL was determined by a combination of Raman thermometry and thermal simulations, adopting a similar approach described in [159]. An ungated structure, i.e. transmission line method (TLM) structure, with 90 μm channel width and 7 μm channel length on the same wafer was used for Raman measurements. This structure is ideal as it generates vertical temperature gradient due to the constant electric field between two electrodes resulting in a constant in-plane heat profile, i.e. no ΔT in the in-plane direction. A power dissipation of 0.494 W was applied at 25^{o}C back-plate temperature to generate a large enough ΔT between GaN and Si layers, the temperature of which were both probed by Raman thermometry with a 488 nm laser and 50x, 0.5NA objective lens, corresponding to a spot size of ~0.5μm. E_2 phonon mode was used to probe GaN temperature as the less stress dependent A_1(LO)[160] signal was too low to perform a temperature analysis due to the thin GaN layer (750 nm thick). The calibration coefficients, which were previously estimated by a former PhD student in our group, Dr. Hangfeng Ji as discussed in Chapter 3.1, were used to estimate GaN and Si temperatures. As GaN is transparent at the measured wavelength, the measured temperature corresponds to the spatial average across the GaN thickness. For the sake of simplicity, thermally insulating passivation layer, thin AlGaN layer and metal contacts, which have negligible effect on the heat transfer, were omitted from the TLM thermal simulations and only half of the structure was considered due to its mirror symmetry. The simplified device structure includes 750 nm thick GaN, 3.7 μm thick SRL and 700 μm thick Si layers. Only GaN thermal conductivity, which is fairly well-established, was set as $160\times(300/T)^{1.4}$ W/mK. Even though Si thermal conductivity is also well-established, dopants added might lead to deviations from the pure Si thermal conductivity. Therefore, the simulation, which was shown in Figure 4.19(a) was used to estimate both Si and SRL thermal conductivities. The applied power dissipation resulted in a 70^{o}C of ΔT between GaN and Si as shown in Figure 4.19(b), which is high enough to estimate SRL thermal conductivity. Si and SRL thermal conductivities were varied such that the simulated temperature values match the Raman measurements shown in Figure 4.19(b), which resulted in the estimated thermal conductivity values of $(134\pm15)\times(300/T)^{1.3}$ W/mK and 24$\pm$4 W/mK for Si and SRL, respectively.

The estimated values are in line with the reported values in the literature [18, 158, 161]. The uncertainties in the fitted values of the thermal conductivities were estimated considering the standard error of the mean of Raman temperature measurements, which was on the order of ±3-15 ^{o}C in the channel and up to 100 μm away from the centre of the channel, as shown in Figure 4.19(b). The uncertainties in the Raman measurements are mainly associated with the SNR of the phonon modes and the peak position fitting associated with the SNR; higher SNR aids fitting the peak position more accurately, and hence results in more accurate temperature estimations. The higher errors in the average GaN temperature, compared to that of Si, shown in Figure 4.19(b), are due to the more than 10% lower SNR of the GaN:E_2 phonon mode compared to Si:F_{2g} mode (See Figure 3.5). The error bars in Figure 4.19(b) represent the standard error of the mean for n=5 successive Raman measurements, taking the errors associated with the peak fitting and the random errors into account.

The average values of the estimated simulation parameters were fed into the thermal simulation of GaN HEMT, where half of the device was considered as done in the TLM simulation due to the symmetry of the geometry and the boundary conditions. The device simulation is constructed considering all the layers present and the metal contacts to be able to represent the real case scenario as much as possible. The temperature rise occurs due to Joule heating ($\boldsymbol{J}\cdot\boldsymbol{E}$) in the 2DEG channel formed on the GaN side of AlGaN and GaN layers. A simplified 3 nm thick uniform heat source is used in the model to represent Joule heating between the source and drain opening, approximating the channel as a simple resistor [18]. As the device measurements were performed on a thermal chuck, a thermal contact resistance is present between the chuck and the wafer, which would contribute to the device temperature rise. This contact resistance can be estimated by measuring the temperature far away from the device where the device heating would negligible effect. The thermal contact resistance between the device and the chuck was found to be 5x10^{11}W/m^{2}K by matching the measured substrate (Si) temperature by Raman thermography 225 μm away from the edge of the device to the simulation. The thermal conductivities of metal contacts (gold), AlGaN and passivation were set as 310 W/mK, 25 W/mK and 1.1 W/mK [18, 156]. The back plate temperature was set to 25^{o}C while the rest of the boundary conditions were set as adiabatic due to negligible radiation and convection losses. This assumption was

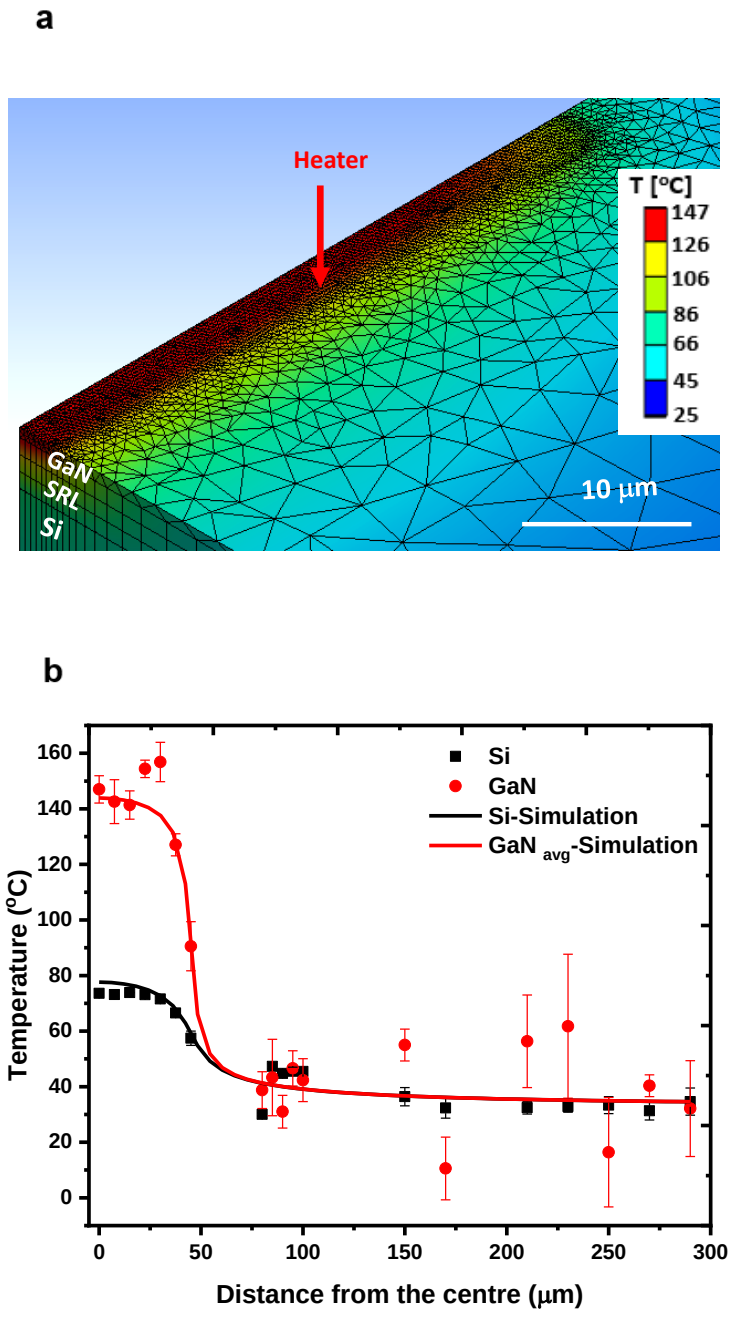

FIGURE 4.19. Thermal conductivity estimation of the strain relief layer (SRL) using a combination of Raman thermography and thermal FEM simulations. (a) Thermal FEM model showing the heat input and mesh details of a TLM (un-gated) structure. (b) Raman thermography measurements overlaid with the fitted simulation temperature profile, for which k_{SRL}=24 W/mK and k_{Si}=134 $\times(300/T)^{1.3}$ W/mK.

confirmed by comparing the simulated temperature with and without radiation and convection losses. It was found that these losses causes only less than 0.01^{o}C temperature rise even with the blackbody assumption (ϵ=1) and h_{conv}=20 W/m^{2}K. The mesh independency of the solution was assured by refining the meshing until the convergence was achieved. The simulation for the maximum measured power dissipation (P_{diss}=4.165 W/mm) is shown in Figure 4.20(a) along with the corresponding meshing in Figure 4.20(b). The surface temperature was extracted for a direct comparison with HQTI measurements.

One question that might arise is that how much the coated QR layer would affect the heat transfer and thus the measured temperature values. In order to assess the impact of the thermal resistance due to QR layer, a thermal conductivity of k_{max}=6.2 W/mK [152] with the maximum measured thickness of 0.5 μm deposition thickness for the QR layer was simulated. This resulted in only ~ 0.1 ^{o}C of ΔT between the passivation surface and the top of the QR layer, as shown in Figure 4.21, which led to the conclusion that measured HQTI values corresponds to "effective" surface temperature due to the negligible thermal resistance of the coating layer.

Figure 4.22 shows the comparison of the HQTI measurements with the thermal simulation, along with the IR measurements, for P_{diss}=4.165 W/mm. The thermal simulation reproduces the peak temperature and main features seen in the HQTI thermal image. The source field plate is connected to the source metal and thermally insulated from the channel heat source as can be seen from the device schematics in Figure 4.11. The thermal simulation predicts a

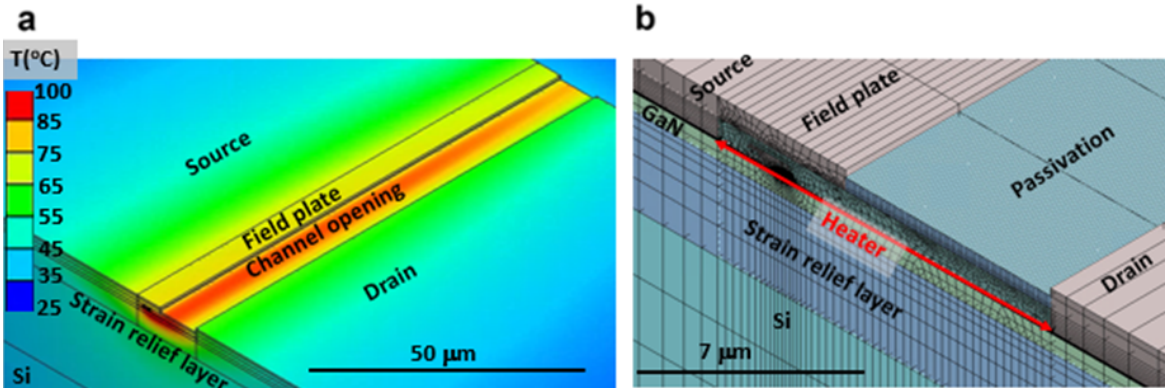

FIGURE 4.20. Thermal FEM simulation of the GaN HEMT, P_{diss}=4.165 W/mm.(a) Simulated temperature profile. (b) Meshing details and heating profile inputted.

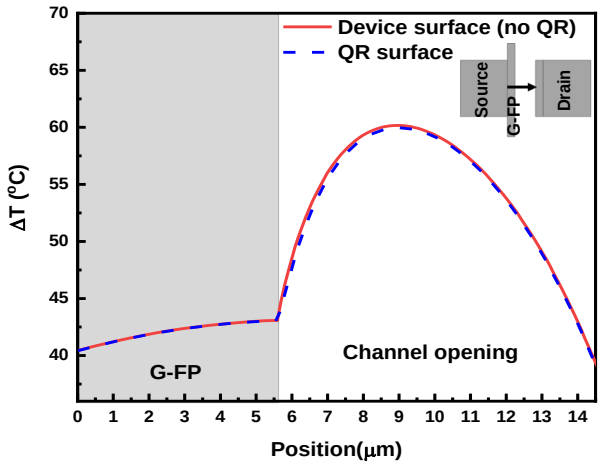

FIGURE 4.21. Simulated effect of the QR thermal resistance on the measured temperature, considering P_{diss}=4.165 W/mm.

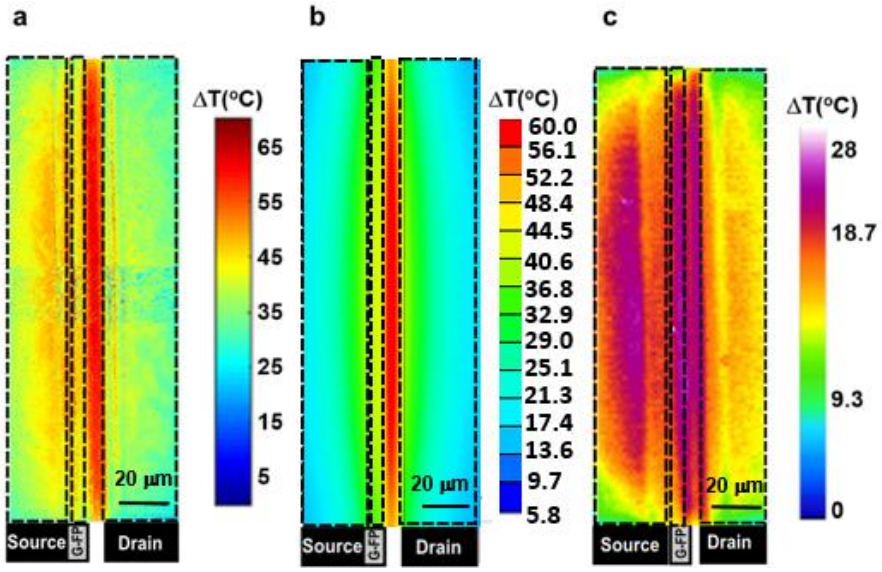

FIGURE 4.22. Temperature rise (ΔT) maps of GaN on Si single finger device: (a) HQTI image under V_{ds}=10 V, I_{ds}=83.2 mA, V_{gs}=5 V, P_{diss}=4.165 W/mm W, $T_{backplate}$=25^{o}C. As the channel width is bigger than FOV, the full image was acquired in three successive acquisitions and patched into a single image. The measured temperature is equivalent to top surface temperature of the device, i.e., in this case surface of passivation layer and metal contacts. (b) Top view of thermal FEM of the device simulating Case (a). As half of the device was modelled, vertically mirrored view was added to the figure to show the full device for comparison. (c) A lower spatial resolution IR thermography image at the same power dissipation in (a), with $T_{backplate}$=52 ^{o}C and V_{ds}=11.3 V, I_{ds}=73.8 mA, P_{diss}=4.165 W/mm.

step in temperature at this location, which can be also observed in the HQTI temperature line profile at the centre of the device, as illustrated in Figure 4.23(a). Fine features such as this are only resolvable when using a sub-micron optical spatial resolution technique such as HQTI. In comparison, the temperature profile measured by lower spatial resolution IR thermography in the same region is remarkably flat, with the maximum temperature rise of ~27^{o}C, which is ~60% less than the maximum HQTI measured value at P_{diss}=0.83 W. The IR temperature measurement underestimation is due to the limited spatial resolution as discussed previously and is similar to the finding reported in [156]. The thermal simulation is similar to the measured temperature profile shown in Figure 4.22(a), with a maximum deviation of ~8^{o}C from the measured value. The simplified thermal model provides a reasonable agreement with the HQTI measurements, without having any free parameters while the only the assumption is the heating profile. The channel temperature profile calculated from the thermal model, representing the temperature rise at the AlGaN/GaN interface from source to drain contact, was also overlaid with the HQTI measurement, indicating that HQTI measurements can simply be approximated as the maximum channel temperature, which is the most relevant parameter for the device lifetime predictions. Estimated precision of the HQTI temperature measurement is ~4^{o}C, which is the standard error of the mean of 7 temperature acquisitions. In the simulation, the temperature variation in the middle of the gate-drain channel region (~2^{o}C, which is within the precision of the technique) over the central 100 μm portion of the gate width (200 μm width) is negligible. Therefore, reported HQTI values in Figure 4.23 are the average over this central area to reduce noise (Please see Appendix A for the line profile drawn using a single pixel without any averaging.).

IR measurements and the thermal simulation with reasonable/reliable thermal properties increase the confidence on the HQTI results. Nevertheless, a further verification effort was pursued using nanoparticle assisted Raman thermography technique, which is described in Chapter 3.1. This technique is more accurate than the standard Raman thermography, which allows probing the temperature within the depth of GaN layer and, in turn, increases the uncertainty in the temperature measurements. While this would not be a concern for a thin (750 nm) GaN layer as in our case, the main challenge was to probe A_1(LO) and E_1(high) phonon modes of GaN simultaneously to decouple stress related effects due to low SNR of A_1(LO) peak

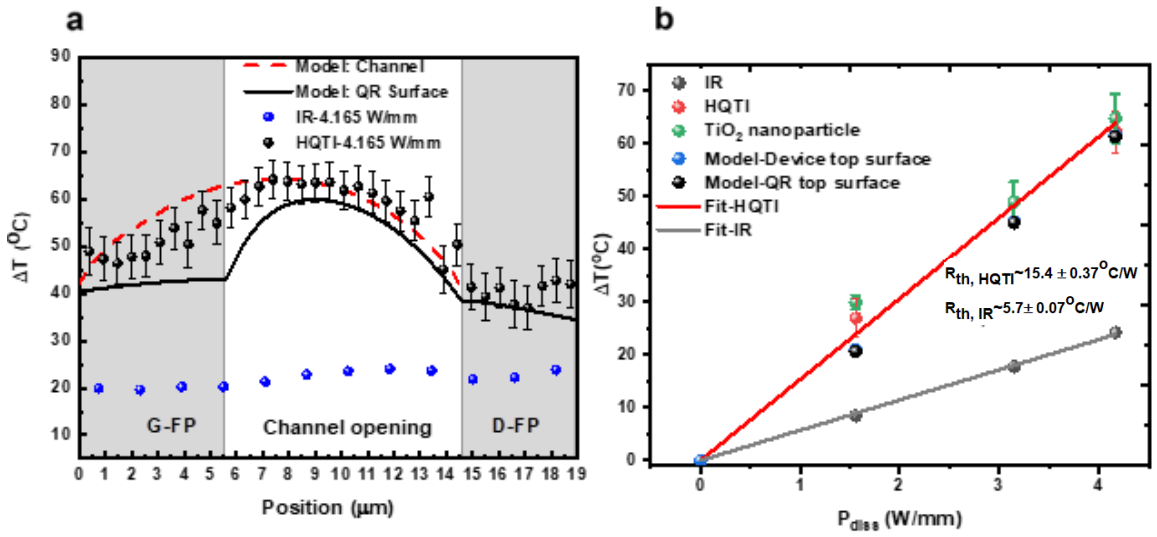

FIGURE 4.23. Temperature line profile and temperature rise (ΔT) vs power dissipation (a) Temperature rise (ΔT) and its gradient across the field plate metal, channel opening and drain metal. The HQTI data represents a lateral temperature average over the diffraction limited optical resolution (680±20 nm) (b) Maximum surface temperature rise vs power dissipation for the thermal resistance estimation of the device. The temperature measured using TiO_2 nanoparticle Raman thermometry at the same location is shown for comparison.

as GaN layer was thin (750 nm), as mentioned previously. ~ 30 nm-size-TiO_2 nanoparticles in 99.98% purity suspension were sonicated and then drop casted on an identical single finger device on the same wafer for a direct comparison with HQTI measurements. The nanoparticles did not form a continuous layer unlike QR deposition, due to highly diluted solution. As there is no continuous layer, this measurement is also useful to understand the effect of thermal resistance due to coating as TiO_2 nanoparticles would have lower thermal resistance. The temperature calibration function, which was already determined in a previous work in our group [116] was used to relate the lowest frequency phonon mode (E_g, 143 cm^{-1}) shift to temperature change. The excitation light source is 532 nm laser focused with a 50x0.5NA infinity corrected objective lens. The measured particle is in the middle of the channel opening and 41 μm along the gate width. Four measurements were performed at each and every power dissipation with an error of $\pm 5^o$C.

Si temperature which represents 1 μm depth with a 532 nm laser was also probed simultaneously to double-check the accuracy of the FEM and found to support the FEM results. Figure 4.23(b) shows the TiO_2 assisted Raman thermography measurements along with the HQTI, IR and simulation results.

Thermal resistance is an important parameter for the thermal reliability benchmarking of microelectronic devices and is defined as:

$$R_{th} = \frac{\Delta T}{P_{diss}} \tag{4.9}$$

Figure 4.23(b) illustrates that estimating thermal resistance based on IR thermography measurements results in an 0.4× underestimation, which might lead to insufficient thermal management during the design stage and eventually early failure if the effect of depth and lateral averaging in the experimental results is not taken into account. This illustrates the advantage of HQTI over IR thermal imaging in the sense that HQTI provides the feature of both large area mapping and accurate surface temperature probing with a more straight-forward data analysis approach than that of IR imaging (requiring surface emissivity calibration). In addition, the lateral spatial resolution of HQTI is much higher (~0.6 μm, illustrated here with 50x, 0.5NA) than the fundamental limit of IR imaging spatial resolution, ~3-5 μm. Temperatures measured by Raman nanoparticle thermometry match the HQTI temperature and the thermal simulation results at the centre of the DUT, within the experimental precision, as shown in Figure 4.23(b). This correlation confirms that the QR deposition has no measurable effect on the DUT surface temperature or thermal resistance.

4.6 Additional considerations

While the accuracy of the calibration and the stability of the focal plane are the main concerns for accurate temperature measurements, other factors due to the intrinsic properties of the sensors, i.e. QRs in this work, are worth consideration for improved accuracy and/or measurement efficiency. These factors could be due to (1) absorption properties of the QRs, (2) their photo-bleaching and (3) electro-optic response of the QRs.

One obvious but crucial aspect to consider is the optical absorption of the LED power by the QRs, which would affect the accuracy of the measurements if overlooked. It was already mentioned that for the illumination power applied in this work, the heating of the sample is negligible. It is also important to consider the heating of the nanorods themselves to reduce the potential measurement errors. In order to quantify this effect, QR response was measured by varying LED power. Figure 4.24(a) shows that the PL intensity increases with the increasing

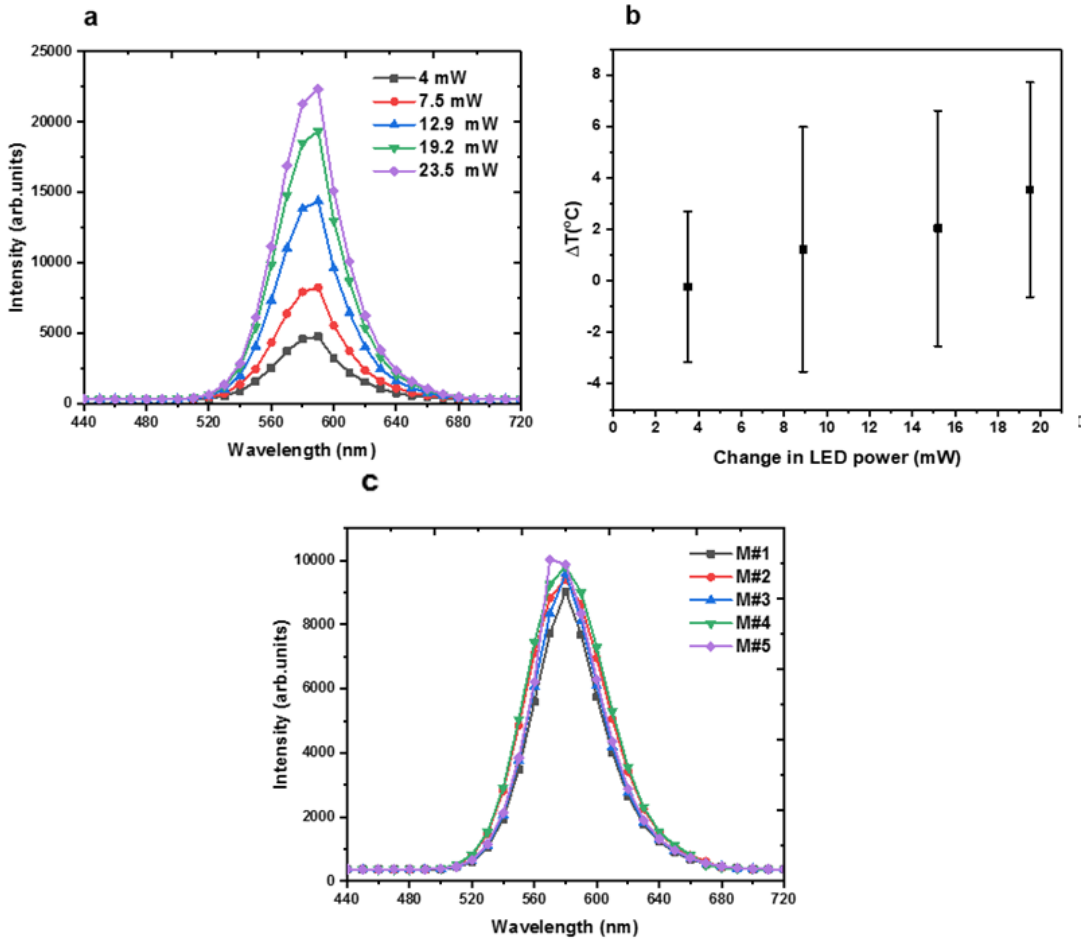

FIGURE 4.24. QR heating and stability due to optical absorption. (a) PL spectrum of QRs measured with the HQTI set-up with varying LED power. (b) Temperature rise of the full FOV of the DUT held at 25^{o}C with varying LED power. (c) Emission stability of QRs observed via successive measurements at 23.5 mW optical power. M♯ represents the measurement order.Note that one measurement cycle for the data represented takes ~20 mins. Peak position is estimated as 577.072±1.18 nm, error corresponding to ~10 ^{o}C precision.

optical power, meaning that more electron-hole pairs are generated while the optical heating, which would result in photoblinking, is negligible.

The optical heating was also verified to be negligible by varying the LED power while the device was held at 25^{o}C as shown in Figure 4.24(b). It is evident from Figure 4.24(b) that temperature rise of QRs themselves due to optical heating, ΔT_{avg}=3±4^{o}C,is negligible even at the maximum LED power (~25 mW). The QRs we use also show good emission stability over the continuous illumination at the maximum LED power applied in our experiments (at room temperature, tested on the calibration sample), i.e. 23.5 mW across the full FOV, as shown in Figure 4.24(c).

A good sensor would ideally yield high SNR, making the measurement more accurate and decreasing the acquisition time. While QRs are good sensors due to their high quantum efficiency, they are, at the same time, susceptible to reversible bleaching at high temperatures due to increasing non-radiative recombination. This results in decreasing SNR at high temperatures and increases the acquisition times. It is a well known relation from digital signal processing that SNR is proportional to the image acquisition time (t) following the relation:

$$SNR \propto \sqrt{t} \tag{4.10}$$

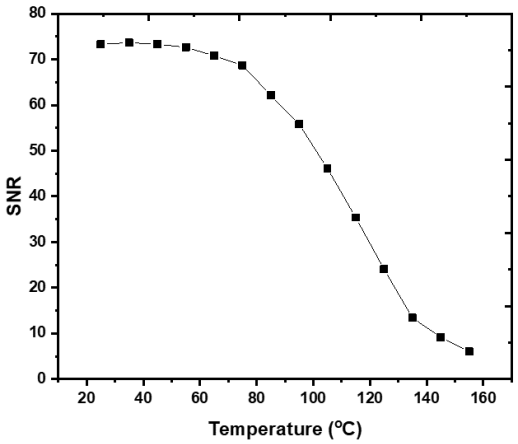

FIGURE 4.25. SNR change with temperature to estimate acquisition time. The data shown is from the calibration.

Figure 4.25 shows that at 155^{o}C, SNR decreases to its 10% value at the room temperature. In order to gain the same amount of room temperature signal at 155 ^{o}C (while not always necessary because SNR> ~7 is usually sufficient for a measurable temperature difference), the integration time should be 100x. Other practical methods, such as a cooled camera, and modifications in the optical path could be considered to significantly improve the SNR.

Electro-optic response of the quantum nanoparticles, which is known as quantum confined Stark effect (QCSE), might also affect the accuracy of the HQTI measurements as the devices are tested under bias. QCSE phenomenon on quantum dots, to be specific on CdSe quantum dots, was observed nearly two decades ago [162]. The shift in the wavelength of the emission spectrum of a quantum nanoparticle (a dot or a rod) under the presence of the external electric field can be theoretically estimated by quantum mechanical calculations. Once the internal electric field within the nanoparticle induced by the application of the voltage is estimated by solving the Poisson equation, electron and hole wave functions and their corresponding energies under this electrostatic potential can be obtained by solving the Schrödinger equation. Subsequently, the Stark shift as a function of the external voltage can be estimated [163, 164]. The magnitude and the sign of the Stark shift (blue vs red shift) depend on the geometry, composition and the orientation of the nanoparticle with respect to the external field [163–165]. It has been calculated and demonstrated that QCSE for the quantum dots exhibit a quadratic dependence on the electric field and a red shift is observed in the emission spectrum of the quantum dots, as the exciton's energy is always reduced [162, 164]. On the other hand, the Stark shift for the quantum rods changes linearly with the external electric field and can be both blue and red shifted, depending on the orientation of the particle under the applied field, which is due to the direction of the induced dipole within these asymmetric particles [163, 164, 166]. For example, the electric field dependency of the peak emission wavelength of a CdSe/CdS core-and-shell quantum rod (with the size 29.0±2.1 nm in length and 4.0±0.4 nm in width, similar to the ones used in this work) was reported to be on the order of ~1 nm per 100 kV/cm [163]. However, the ensemble of randomly oriented nanorods was shown not to exhibits a measurable Stark shift, even for the ZnSe/CdS nanorods, which exhibit a 5x higher Stark shift than those of CdSe/CdS nanowires at similar external electric fields [166], i.e. a portion of the particles exhibited a red-shifted spectrum

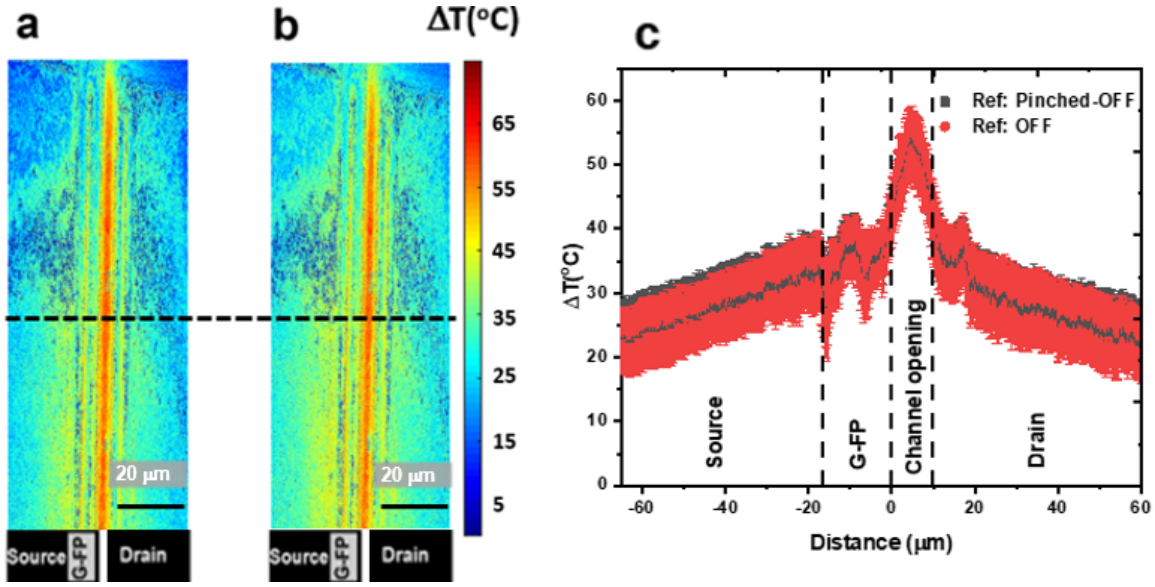

FIGURE 4.26. The effect of Quantum Confined Stark Effect on the HQTI measurements for the ON state: V_{ds}=10 V, V_{gs}=5 V, I_{ds}=83.2 mA. The reference condition (at room T) for this ON state is : (a) Pinched OFF reference: V_{gs}=0 V, I_{ds}=0 A (no heating but under the presence of the electric field at the reference state). (b) OFF state reference: V_{ds}=0 V, V_{gs}=0 V, I_{ds}=0 A (no heating, no electric field at the reference state). (c) Line profile across the middle of the image shown in (a) and (b). The images represent ~ 1/3 of the device which is within the FOV.

while the spectra blue-shifted for the rest, resulting in a non-detectable change in the emission spectrum of the ensemble. This is mainly attributed to the the dependence of the shifts on the orientation between the electric field and the nanorods [166]. Consequently, the spectrum is broadened but no measurable shift is observed. We expect to observe a similar effect on our device measurements as the quantum rods are randomly distributed on the device surface. In order to test whether the Stark shift of the ensemble of the nanorods has a negligible effect on our temperature measurements, HQTI measurements were performed on the above-mentioned DUT at two different reference conditions: (a) Pinched-OFF reference state at V_{ds}=10 V, V_{gs}=0 V, I_{ds}=0 A (no heating but under the presence of an electric field of ~10 kV/cm at this reference state) and (b) OFF reference state at V_{ds}=0 V, V_{gs}=0 V, I_{ds}=0 A (no heating, no electric field at this reference state). The ON state is the same for both tests, i.e. V_{ds}=10 V, V_{gs}=5 V, I_{ds}=83.2 mA. Figure 4.26(a) and Figure 4.26(b) show similar thermal images for the pinched-OFF and OFF

state reference cases, respectively. It can be seen from the line profile shown in Figure 4.26(c) that Stark shift of the ensemble of the nanorods on the DUT has no measurable effect for the results presented here. Yet, it is important to be aware of this phenomenon if the nanoparticles are aligned in the same direction of the DUT or quantum dots (rather than rods) are deposited as the sensor, especially for high voltage tests where the Stark shift can be detectable. In that case, the Stark effect shift can be circumvented by selecting proper reference conditions for HQTI measurements.

In addition to the considerations in terms of accuracy, the question of whether the QR layer is removable might arise, such that the DUT is truly unaffected for any further processing. We sonicated the QR deposited DUT with a pure hexane solution and partially removed the QR layer. The QR layer emission intensity decreased by up to 90%, as shown in Figure 4.27. QR layer might be completely removed if sonicated with different solvents or alternatively with higher sonication powers which were not available for a benchtop sonicator we used.

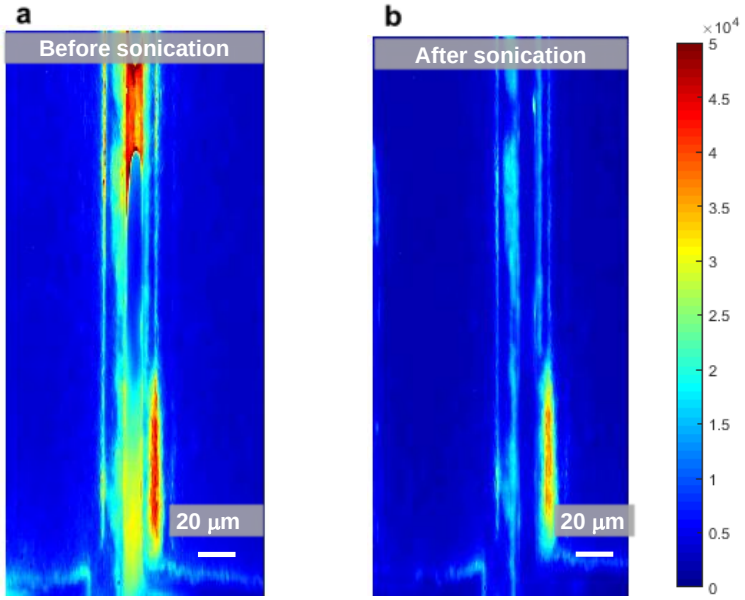

FIGURE 4.27. QR layer removal by sonication: (a) The emission intensity of a QR deposited device at 570 nm (Before sonication). (b) The emission intensity of the same device at 570 nm after sonicated with hexane.

4.7 Conclusion

A new wide field, sub-micron resolution thermography technique was developed and demonstrated on a GaN based HEMT. The technique was benchmarked against the standard IR thermography. IR thermography was found to underestimate the device temperature by ≈60% compared to HQTI measurements, due to lateral and depth averaging. HQTI measurements were verified by finite element thermal modelling and nano-particle assisted Raman thermometry measurements, increasing the confidence on the accuracy of the technique developed. The DC characteristics of the device was shown to be unaffected by the coating layer. It was also found that the coating layer does not have a measurable impact on the thermal performance of the DUT. The additional considerations due to intrinsic properties of the QRs which might affect the accuracy of the HQTI measurements were highlighted in case the devices are tested at different ambient and bias conditions than those presented here. The advantage of the technique is that it is generic and requires only one-off calibration unlike other thermal imaging techniques.

CHAPTER 5

TIME RESOLVED HYPERSPECTRAL QUANTUM ROD THERMAL IMAGING: TEMPERATURE TRANSIENTS IN A GAN HEMT

The steady state temperature measurements are useful for benchmarking different device designs whereas the transient thermal dynamics need to be understood to predict the device performance in actual operating conditions where the gate is under pulsed operation. Transient thermal characterisation is crucial from the reliability stand point because the evidence shows that temperature transients in space and time are far more important than the steady state temperature [167]. For example, in a recent study, the channel temperature of a GaN based device was predicted to be 9% higher in RF operation at high (drain) voltages (> 100 V), which may correspond to ≈ 10 years of reduction in the device life time [18]. Thermal dynamics during device operation is also known to drive fatigue related mechanical failure modes due to the mismatch in the thermal expansion coefficients in the electronic packages [168]. Apart from thermomechanical failure mechanisms, dynamic thermal effects were also reported to be an important parameter affecting linearity of GaN based power amplifiers by causing long term memory effects, which are observed as amplitude variations over time [169]. Therefore, a reliable transient thermal characterisation serves for an electro-thermo-mechanically reliable device (and system) operation.

This chapter describes the development of the time resolved hyperspectral quantum rod

thermal imaging (T-HQTI) technique, as an extension of the work presented in Chapter 4. The technique was demonstrated on a similar structure tested in Chapter 4 with 20 μs time resolution. The results were verified with transient thermoreflectance measurements which were calibrated with the transient TiO_2 assisted Raman thermograpy measurements. This chapter includes a significant content from our recent publication, Ref. [170] with permission from ©2020 IEEE, albeit with more details.

5.1 Experimental set-up and device details

The experimental set-up for the steady state measurements described in Chapter 4 was modified for the time resolved HQTI measurements by synchronising the excitation light source (LED) and the device (gate) pulse timing. Figure 5.1 shows the operating principle of T-HQTI. The device pulses and the LED pulses were generated by Tabor 8500, 50 MHz and Agilent 8114 A, 15 MHz pulse generators, respectively, while the camera operates in CW mode as illustrated in Figure

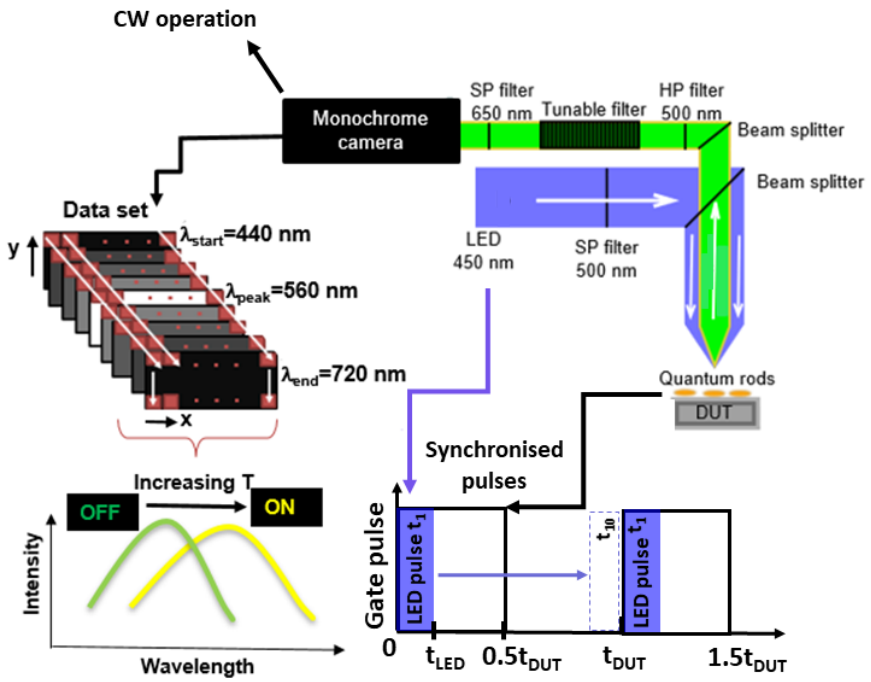

FIGURE 5.1. The schematic of the operating principle of the time resolved HQTI set-up. The gate pulse was synchronised with the LED pulse to achieve time resolution while the camera operates in the CW mode.©2020 IEEE.

5.1.

The time delay between the LED pulse and the device pulse was adjusted such that the LED is turned ON at a desired time interval, which determines the time window probed and the duration of the measurement, i.e. the time resolution is determined by the LED pulse length. For the measurements performed in this work, the device was pulsed with 50% duty cycle while the LED duty cycle was set to 10% to achieve sufficient time resolution to capture the temperature transient.

As the signal to noise ratio (SNR) would diminish with the duty cycle of the LED pulse compared to that of DC measurements, time resolved measurements were performed by using the boxcar integrator (a.k.a. boxcar averaging or gated integration) method in order to achieve sufficiently high SNR, similar to the time resolved Raman thermography measurements discussed in Chapter 3.1. The boxcar integrator technique was first experimentally demonstrated in 1955 to improve SNR in nuclear magnetic resonance measurements [171] and has been successfully applied for light measurements since then [172, 173]. The boxcar integration relies on integration of the periodic signal in a specific time window that is gated. In other words, in order to apply boxcar integration, the signal must be repetitive and the sampling signal should be selected for a selected time interval during the signal train. *SNR* for a digital camera is given as :

$$SNR \approx \frac{S}{\sigma_{eff}} \tag{5.1}$$

where S is the signal and σ_{eff} is the effective noise, which are given in Equation 5.2 and 5.3, respectively as :

$$S = (QE)Nt \tag{5.2}$$

where QE is the quantum efficiency of the camera, N is the number of photons hitting the camera sensor per second and t is the light exposure time, i.e. the duration during which the LED is ON for our application.

$$\sigma_{eff} \approx \sqrt{\sigma_D^2 + \sigma_R^2 + \sigma_S^2} \approx \sqrt{I_D t_{total} + \sigma_R^2 + (\sqrt{(QE)Nt})^2} \tag{5.3}$$

where σ_D is the dark noise due to thermal excitation of electrons from valence band to conduction band, which is independent of the signal level, σ_R is the read noise due to analog to digital

conversion (ADC), which only depends on the design of the sensor (independent of the signal level or temperature of the camera), and σ_S (=$\sqrt{(QE)Nt}$) is the photon shot noise due to the statistical nature of photon counting [174]. σ_D is equal to $\sqrt{I_D t_{total}}$, where I_D is the dark current and t_{total} is the total exposure time of the camera when it operates in the CW mode. Total exposure time of the camera, t_{total}, in CW operation increased by 10^6 (for a camera exposure time of 7-8 s for the measurements in this work) when the boxcar technique was implemented compared to single pulse operation. Considering Equations 5.1-5.3, this would increase the SNR by more than 1000 times compared to an identical set-up and operating conditions with single pulse operation. The experimental set-up shown in Figure 5.2. was realised such that it works based on the boxcar averaging principle. We emphasize that the resulting temperature measurements would be the "pseudo-step" response to the periodic device pulses, rather than the "step" response as the measurements include the heat accumulation from the previous pulses due to the implementation of boxcar integration technique. This pseudo-step response is a result of the successive $\approx 10^6$ power dissipation pulses.

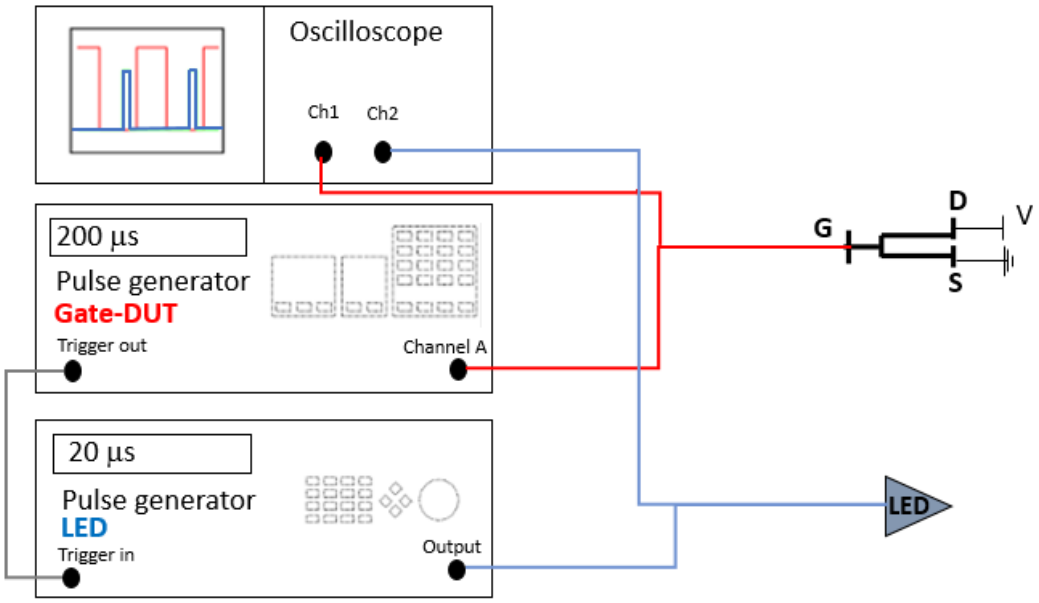

FIGURE 5.2. Experimental set-up for the T-HQTI measurements. The gate is pulsed with 50% duty cycle with T=200 μs while the drain is under DC bias.The LED pulse width is 20 μs with a 10% duty cycle. The figure was adopted from [117].

The same type of devices described in Chapter 4, i.e. single finger field plated GaN on Si HEMTs, were tested for the demonstration of T-HQTI. The gate electrode was continuously pulsed with a period of T=200 µs with 50% duty cycle, between the ON and the OFF state, with the OFF state at V_{gs}= 5 V and the ON state at V_{gs}= 0 V, while V_{ds} was kept constant at 11 V I_{ds}=84 mA; Joule heating of 4.62 W/mm). The optical heating due to the incident LED light can be again neglected (<10 mW/mm^2) and is below the GaN band gap so as not to generate photo current in the DUT. Temperature measurements were performed on a six inch wafer mounted on a thermoelectric vacuum chuck set at 25^{o}C, as in the case in Chapter 4. All temperature measurements were taken with the device in quasi-equilibrium, i.e., waiting for a sufficiently long time until the device warms up. The total data acquisition time for a single monochrome image at a particular wavelength is 7-8 s for this optical configuration, which can vary depending on the signal to noise ratio. The temperature was related to the centre wavelength of the PL emission as described in Chapter 4.2.

5.2 Results and Discussion

The resulting maps of the temperature transients at the above mentioned conditions are shown in Figure 5.3. The thermal images, which represent the "effective" surface temperature, show the expected trend qualitatively: a rising temperature transient when the device is ON and a falling transient when the device is pinched-OFF, the channel being the hottest region due to its highest resistance. The temperature line profile along the dashed line A-A' shown in the optical image shows this trend more clearly. Transient measurements also suggest that the source contact has slightly higher resistance than that of the drain contact, although it is less significant than that of the DC measurements shown in Chapter 4 due to the cooling cycle in the OFF state of the pulse train.

Whenever a new technique is introduced, it is imperative to verify the accuracy of the technique with a well-established technique. Transient Raman thermography and transient thermoreflectance measurements (TTR) are the two alternative techniques to verify T-HQTI measurements. As discussed in Chapter 4, the phonon modes of GaN gave a very low signal for

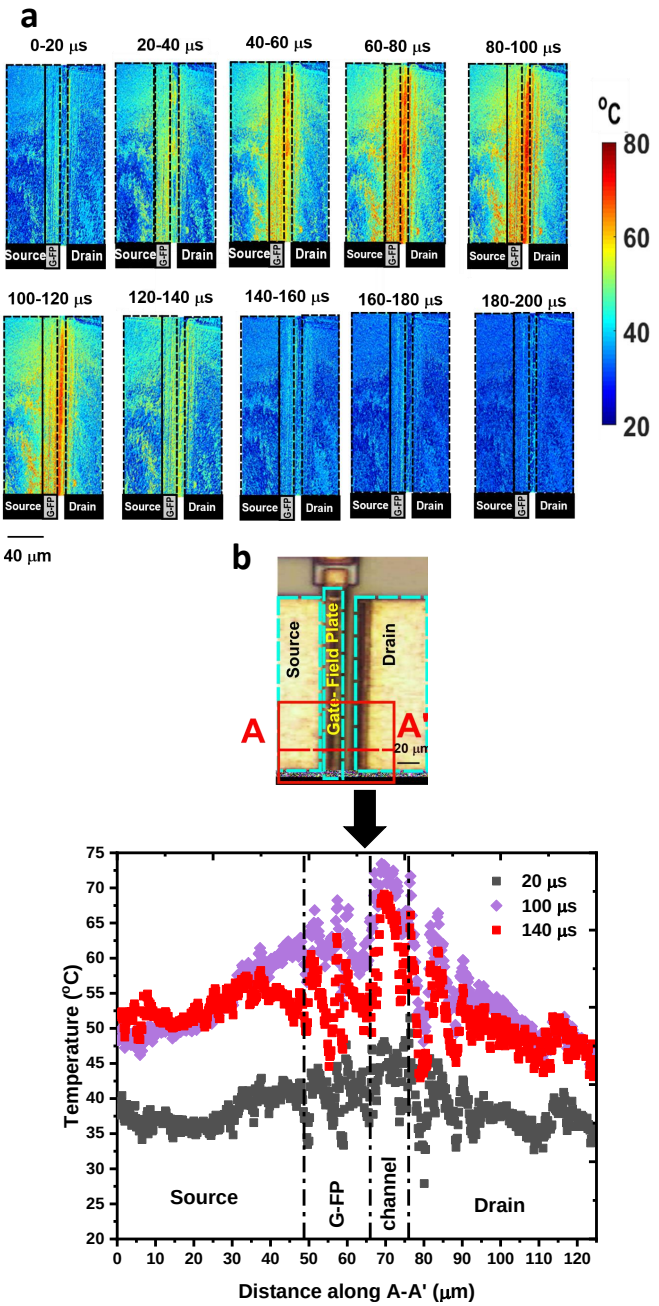

FIGURE 5.3. Temperature transients using T-HQTI: (a) Temperature transients (absolute) of the DUT during the device pulse period, measured with time resolved HQTI.©2020 IEEE. (b) The temperature line profiles, which represent the average of n=5 successive measurements, are along the dashed line A-A' shown in the optical image. In order to reduce the noise, the temperature data represent the average temperature over 70 pixels, corresponding to ~12.6 μm, along the gate width, where the temperature rise is expected to be equivalent.

the test sample even for the steady state Raman measurements due to its small thickness of 750 nm. Therefore, probing the phonon modes of GaN in transient operation would be prone to high errors and impractical. An alternative approach could be adopting nanoparticle assisted (TiO_2) transient Raman measurements. This would also be time consuming as it requires sweeping the whole time window as described in Chapter 3, considering that SNR also diminishes, which necessitates longer integration times on the order of 10s of minutes. On the other hand, TTR measurements can be performed in a relatively short time which is on the order of several seconds. The downside of TTR measurements is the complications in terms of the interpretation of the signal coming from semiconductor layers due to interference effects, as discussed in Chapter 3.3. This problem can be circumvented if the measurements are performed on the metal contacts, which are opaque under 532 nm and where the penetration depth of visible light is on the order of 10s of nanometers. Yet, the calibration of TTR measurement is still challenging due to thermal expansion effects during the calibration performed on a hot plate, as present in all other optical thermography techniques, which manifests itself as large error bars in the thermoreflectance coefficient, C_{th}. One way to perform a reliable TTR calibration is implementing a piezoelectric stage correction to account for the drift due to thermal expansion [175], similar to the approach adopted in Chapter 4.

In order to overcome the errors due to thermal expansion effects in a standard calibration, alternative approaches such as combining transient Raman thermography and thermal modelling to extract C_{th} at the gate foot on top of the AlGaN barrier were also suggested [176]. In the approach proposed in [176], a short time interval, on the order of 100-250 ns, in the OFF state of the pulse operation at which the average GaN and gate metal foot temperatures are equivalent was identified from thermal simulations for a GaN on SiC device. TTR measurements at 532 nm were performed at the backside of the device, unlike the standard practice, as SiC is transparent under this wavelength. Backside TTR approach minimizes the previously mentioned interference effects as the dominant reflection occurs at the gate foot metal due to the negligible refractive index difference between the device layers, which would result in negligible reflection from there according to Fresnel reflection equations. Backside TTR measurements at the pre-determined time interval were correlated to the average GaN temperature measured by transient Raman

thermography to extract C_{th}. As this approach requires a transparent substrate and a measurable GaN Raman signal, it is not applicable to our case where we tested a GaN on Si device with a very thin GaN layer which does not give a high enough Raman scattering signal. Besides, this approach would require extraction of the effective surface temperature, which we aimed to measure with T-HQTI, from the thermal simulations. Here we use an alternative but a similar approach for the thermoreflectance calibration: nanoparticle assisted transient Raman thermometry, using 30-nm-size TiO_2 nanoparticles, as in Chapter 4, to measure the surface temperature at precisely the same location as the TTR measurement. This approach is more time saving than that of sole transient Raman thermography as less time windows are required as the full transient profile is captured by the faster TTR measurements. All measurements, including T-HQTI, were performed with a 50x, 0.5 NA objective lens, as in Chapter 4.

Figure 5.4 shows the location on the DUT where these measurements were performed, along with the schematics which represent the corresponding depth resolutions. It is important to note that even though lateral spatial resolutions of two measurements are different, i.e. 30 nm vs ≈0.5 μm (for the 532 nm wavelength laser used here), the measured signals represent similar quantities because the temperature gradient on the field plate metal is expected to be negligible considering the measurement precision (±5-10^{o}C). The same idea applies to axial resolution. The axial resolution of the TTR measurement corresponds to the penetration depth of the 532 nm laser into the metal. This penetration depth can be approximated for the normal incidence of radiation using the relation:

$$t = \frac{\lambda}{4\pi k} \tag{5.4}$$

where the wavelength of the incident light λ=532 nm and the extinction coefficient (damping factor) $k \approx$ 2.5 for the gold films of a thickness of 25-175 nm [122], giving a penetration depth of $t \approx$ 16 nm, which can be simply approximated as the surface temperature. Hence, it is a fairly valid approximation to consider that TiO_2 assisted transient Raman and TTR measurements performed at the same location on the field plate metal represent identical quantities, as long as TiO_2 nanoparticles reach thermal quasi-equilibrium with the surface of the DUT at the given

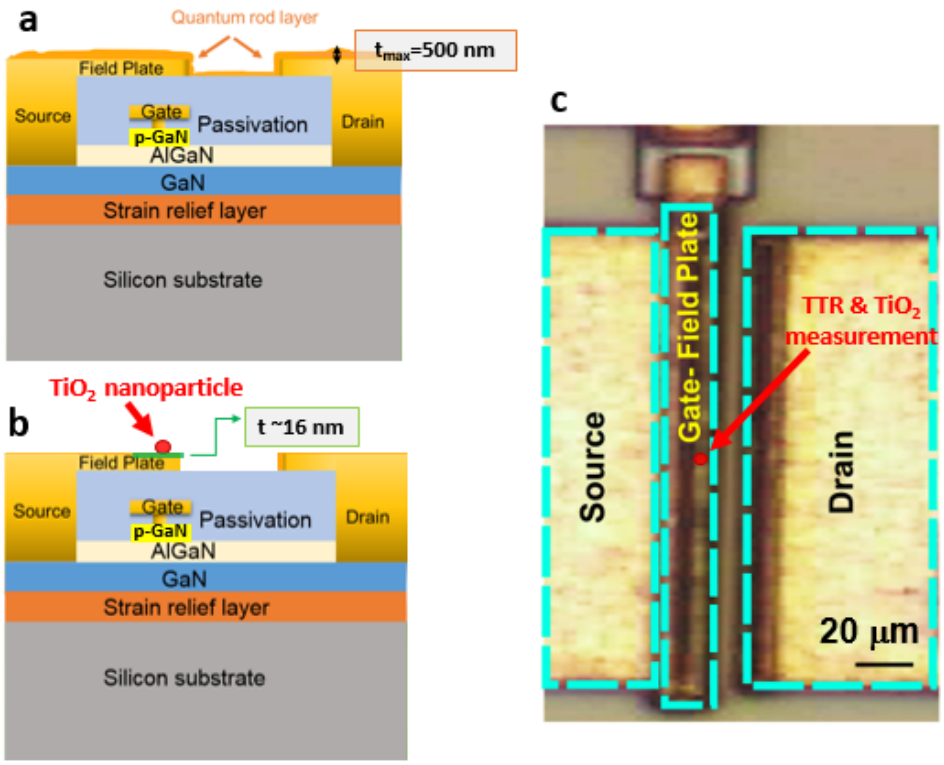

FIGURE 5.4. The schematics of the location of the temperature measurements and their corresponding depth resolution on the DUT. (a) Location and depth resolution of the T-HQTI measurements. (b) Location and depth resolution of the TTR and TiO_2 assisted transient Raman measurements. ©2020 IEEE. (c) Optical image of the DUT showing the location of the TTR and TiO_2 assisted transient Raman measurement on the DUT.

pulse conditions with negligible thermal contact resistance. The quasi-equilibrium condition with a negligible contact resistance is assured by measuring the TTR traces at the same location on a "clean" device, which is identical to the device on which T-HQTI was performed (a sister device on the same wafer) but where there is no nanoparticle deposition, and on a sister device on which the TiO_2 nanoparticle is deposited (on the same wafer with that of the device on which T-HQTI was demonstrated). Figure 5.5 shows that the heating and cooling traces, hence the thermal time constants, are similar for both the clean and TiO_2 deposited sister devices (which are both identical to the device on which T-HQTI was performed), indicating that the quasi-equilibrium condition is satisfied and the thermal contact resistance is negligible under these operating conditions (in the 100s of MHz range). TiO_2 assisted transient Raman measurements were performed at the time intervals shown in Figure 5.6 (a). The thermoreflectance relation given in

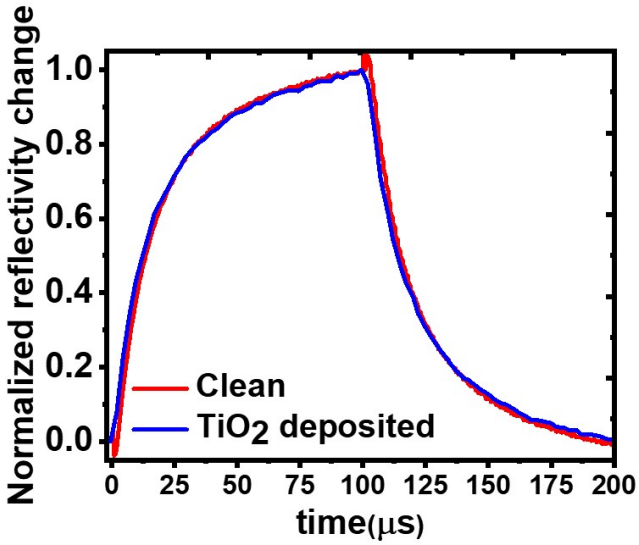

FIGURE 5.5. The effect of nanoparticle deposition on the transient dynamics of the single finger GaN-on-Si device, which is identical to the device on which T-HQTI was performed, to verify that the thermal time constant of the "clean" device is unaffected by TiO_2 nanoparticle deposition. The device used for T-HQTI measurements is identical to and on the same wafer with the "clean" and TiO_2 deposited devices.

Chapter 3.3 (Equation 3.31) is used to extract the thermoreflectance coefficient, C_{th}=4.25×10^{-2} ±2.97×10^{-3} $^{o}C^{-1}$. The thermoreflectance coefficient is typically in the 10^{-2}-10^{-5} $^{o}C^{-1}$ range, depending on the material, illumination wavelength, optical set-up and surface roughness [177]. In the literature, the thermoreflectance coefficient of gold is reported to be in the 10^{-3} [178, 179]-10^{-4} [177, 180, 181] $^{o}C^{-1}$ range for 530 nm excitation. Our one order of magnitude higher thermoreflectance estimation could be due to the highly rough metal surface, which is optically visible, and the optical set-up. This estimation also highlights the need for *in situ* calibration for each particular test structure for thermoreflectance based thermal imaging. Figure 5.7 shows the temperature estimated by the T-HQTI and TTR measurements at same location on the source connected field plate metal, at the point indicated in Figure 5.4(c). Maximum channel temperature is overlaid for comparison. The reasonable agreement between T-HQTI and TTR measurements suggests that 500 nm thick QR coating layer has negligible effect on the heat transport under the considered time scales. Therefore, at the 100s of MHz regimes considered in this work, T-HQTI

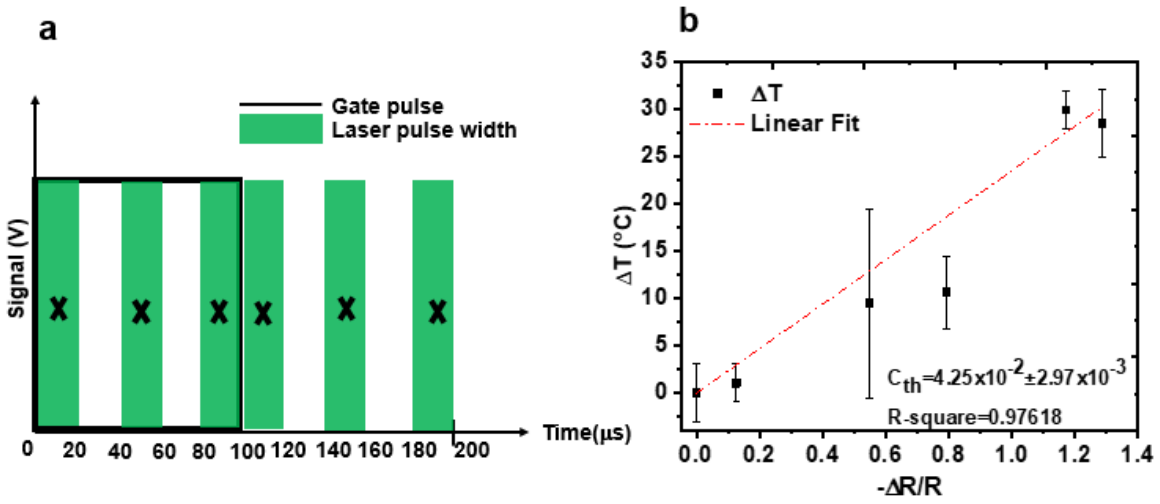

FIGURE 5.6. TTR calibration with TiO_2 assisted nanoparticle measurements performed at the same location on the source connected field plate metal of the DUT. (a) Time windows of the pulse train where TiO_2 assisted transient Raman measurements are performed, shown by green laser pulse blocks. (b) C_{th} calibration. ΔT is with respect to T_{ref} which is the TiO_2 temperature at Δt=190±10 μs. ©2020 IEEE.

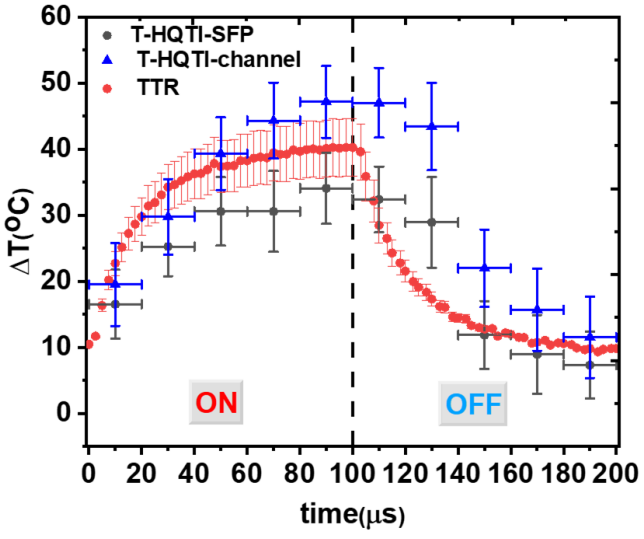

FIGURE 5.7. Comparison of TTR and T-HQTI measurements on the source connected field plate metal of the GaN HEMT device. TTR and T-HQI measurements were performed at the identical operating conditions. ΔT corresponds to temperature rise with respect to the OFF state. Maximum channel temperature transient was overlaid for comparison with the field plate transient.©2020 IEEE.

measurements can be considered as “effective surface” temperature and can be input as such for the thermal/electro-thermal simulations. However, thermal contact resistance between the device surface and the coating layer can affect the time for the nanoparticles reach the equilibrium with the device top surface for shorter time scales, as demonstrated in Ref. [30] by depositing diamond particles of ~ a μm size on a single finger GaN HEMT and measuring the transient temperature using time-resolved Raman thermography, with the aid of thermal simulations. A thermal contact resistance of ~10^{-6}m^{2}K/W was found to exist between the surface of the device and the diamond nanoparticles, leading to several μs of delay in the thermal response time between the device surface and the nanoparticle, as revealed with the aid of thermal simulations [30]. The nanoparticles were found to be in thermal equilibrium with the device surface after 10μs [30]. Similar time scales can be imposed as a limit on our system, as well, in terms of the validity of the "effective surface temperature approximation" approach. In that instance, temperature measurements can be complimented with thermal modelling to extract the thermal resistance between the coating layer and the surface of the DUT. Figure 5.7 also shows that the thermal time constant of the channel is higher than that of the field plate metal, which is expected as the temperature drops at the metal contacts when the heat diffuses from the channel.

The ultimate time resolution achievable with the T-HQTI measurements is limited by the radiative life-time (relaxation time) of the QRs, which is strongly dependent on the morphology and synthesis conditions [137]. Synthesis conditions have a direct impact on the material quality and the defects in the material create trapping sites, reducing the relaxation times. We demonstrated here 20 μs time resolution due to the limitations of the rise time of the pulse generator used for the LED pulsing in our test set-up. However, time resolution of this technique can be extended down to 10 ns for the QRs considered here [151] with small modifications in the test set-up, such as using a higher power LED or a CCD with a higher quantum efficiency. It is, in fact, possible to decrease the time resolution below the radiative recombination limit of the QRs, depending on the application, using time-gated scientific cameras, which are currently commercially available down to the frame rates on the order of 10^9 fps [182], corresponding to ps gating, rather than CW operation. However, considering the operation range of the GaN based power devices, such time resolutions would be beyond what is required, i.e. overengineering for this application.

5.3 Conclusion

We demonstrated a wide field, time resolved device thermography technique for the surface temperature mapping of a pulsed operated device at the MHz range with sub-micron spatial resolution, which requires only one-off equipment dependent calibration. The transient HQTI (T-HQTI) measurements were verified by TTR technique. It was discussed that at the 100s of μs-length-pulsing regime, quasi thermal equilibrium between the QRs and the surface of the DUT can be reached, allowing the approximation of QR temperature $\approx$ surface temperature of the DUT. However, as the time scales decreases by an order of magnitude, down to the 10s of μs, then the thermal contact resistance between the temperature sensors and the DUT might break this approximation, as estimated on similar test systems [30]. It was also highlighted that the intrinsic time resolution of the technique is only limited by the radiative life time of the QRs with the current configuration and can be improved even further by using high speed time gated scientific cameras. The main advantages are that the technique being generic and can be easily applied for different devices, requiring only one-off calibration and having the potential of GHz range time resolution surface temperature imaging.

CHAPTER 6

THERMAL BOTTLENECKS OF GAN ON SILICON MULTIFINGER POWER DEVICES

GaN based HEMTs are viable candidates not only for RF but also for high power applications due to high breakdown voltage of GaN which is up to 3 MV/cm [183]. Thermal considerations for an improved performance for RF applications have been addressed for GaN based devices extensively during the last several decades [20]. At the device level, the focus has been on the minimization of the thermal boundary resistance (TBR_{eff}) between the GaN buffer and the substrate of the choice (Si, SiC) [117, 184–186], which originates from interfacial resistance of the strain relief layer (or nucleation layer for SiC substrates) grown in between these layers, which has inherently low thermal conductivity due to its polycrystalline nature [117]. An alternative approach for an improved thermal performance is the integration of a high thermal conductivity substrate, namely diamond, which is also an active area of research [16]. TBR_{eff} between the material interfaces was also speculated to be a possible thermal bottleneck for GaN based power devices [187]. However, the thermal management strategies adopted for RF devices might not be the optimum solution for power devices, which have different device geometry and layout. A recent study by Power [20] focused on alternative electro-thermal modeling of GaN based high power Schottky barrier diodes under DC operation to identify possible thermal reliability issues, namely non-uniform heating due to current crowding and the

impact of the device epilayer on the lifetime estimations. As a part a joint project with Infineon Technologies, in this chapter, we aim to identify the possible thermal bottlenecks at the device level for a GaN based multi-finger power HEMT under DC operation, using on-wafer samples. The findings are expected to be useful to determine the optimum strategy for performance improvement with the current GaN technology for customer market applications where the low cost solutions are of concern.

6.1 Multi-Finger Power Device Details

Multi-finger power devices have an interdigitated layout as shown in Figure 6.1(a), where the fingers are connected in parallel with a common source, drain and gate contact pad to achieve a compact layout and withstand high powers. Such a compact layout is the standard practice in power device design where the current requirements exceed 1 A [183]. This compact design where multiple fingers embedded in a single device, rather than connecting multiple transistors in parallel, saves material and therefore the cost decreases. The channel widths of power devices, being the largest dimension of the device, are on the order of several hundreds of micrometers or even a mm to decrease the power density. The gate contact pad is smaller compared to drain and source pads as it carries only small leakage currents (typically 1 mA/mm [119]). Figure 6.1(b) shows an image of a normally-off 70 mΩ power GaN HEMT, which can withstand up to 600 V [187]. The power HEMTs tested in this work have a similar layout shown in Figure 6.1 (a)-(b), consisting of 100 gate fingers. The design includes source and drain connected field plates. The device is on the same wafer with the structure tested in Chapter 4-5. Therefore, the epitaxy is the same as shown and described in Chapter 4.3. The source-gate and gate-drain distances of the tested 1.2 mm wide multi-finger device are 1.8 μm and 12 μm, respectively. The total channel width is 14.6 μm.

6.2 Wafer level thermal characterisation

IR thermography was used first in order to screen devices for anomalous temperature distributions and to validate the accuracy of the heating profile assumption in the simulations. IR

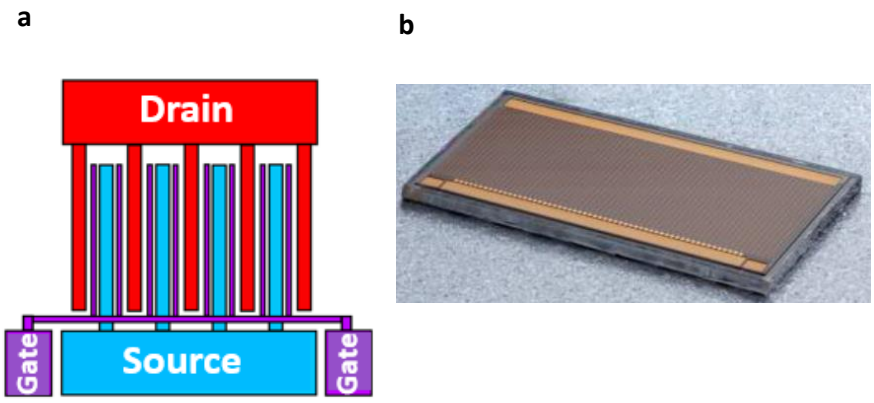

FIGURE 6.1. Multi-finger design of the power device: (a) The top view schematic of an interdigitated design of a multi-finger power device design. Adopted from [20] (b) Photograph of a normally-off 600 V GaN device with 4.4x2.3 mm^2. Image taken from [187]. © 2015 IEEE.

thermography has two disadvantages as discussed in Section 3.2: (1) Spatial resolution is limited ($\approx 6\mu$m in this case). (2) Spurious temperatures may be measured in transparent semiconductors (Silicon is transparent at the measured IR wavelengths). For IR thermography measurements, the device, which includes 100 gate fingers, was operated at a power dissipation of P_{diss}=19.6 W, corresponding to a power density of $\approx$ 0.16 W/mm. The chuck temperature was set to 70^{o}C to elevate the device IR emission above the ambient IR radiation in order to improve the accuracy, by increasing IR emission following Planck's law of radiation, as discussed in Chapter 3.2. One quarter of the device was screened to gain insight into the temperature profile. A thermal only finite element model (FEM), calibrated with standard Raman thermography measurements, was simulated to compare temperature profile of the channel with those of IR measurements. One quarter of the device was modeled due to symmetric boundary conditions, decreasing the computational time for such large device simulations. The material property estimations explained in Chapter 4 were used for this model. The model was simplified by neglecting thin AlGaN (80 nm) and passivation layers (800 nm) as well as metal contacts as these layers (< 1 μm) had been shown to have a negligible effect on the heat transfer in the previous works, especially for large area devices [20, 27]. Thermal-only models require the assumption of the heating profile unlike

coupled electro-thermal models which can quantify the distribution of the heating profile by solving drift-diffusion equations to obtain current density and electric potential distributions within the device. The previous work implementing such coupled models for field plated devices shows that the heating profile can be modeled as a surface heater distributed between the gate edge and the drain contact [18]. We used this estimation as a starting assumption for the thermal-only model. Figure 6.2 shows the heating profile input representing the Joule heating in the channel, placed between the 12 μm gap between the gate foot and the drain contacts for the first five adjacent fingers, while the rest of them was represented as a block heater to decrease the computational time.

Although IR thermal maps are not expected to give accurate temperatures, they are useful to estimate the heating profile qualitatively and check the accuracy of the heater assumption. As IR thermography is a wide-field technique, it is particularly useful for screening of such large area devices. Figure 6.3 (a-c) illustrates a comparison between the IR measured and simulated temperature distributions across the DUT. The simulation qualitatively matches the measured temperature distribution, although there is an offset as shown in the line profile in Figure 6.3(b)

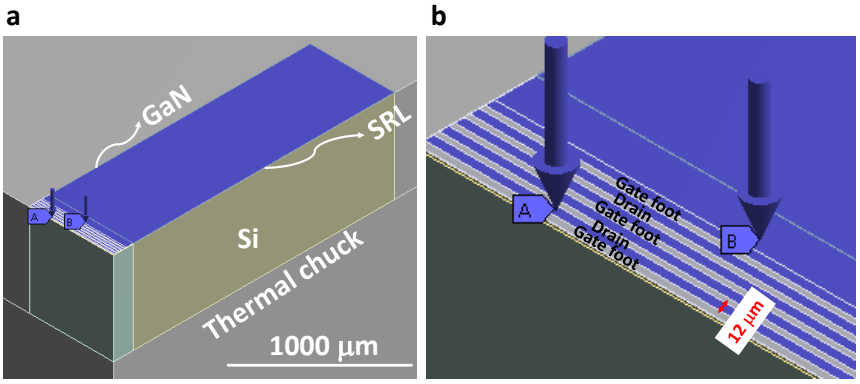

FIGURE 6.2. Finite element model heat input: (a) Simplified thermal model and heat input representing the Joule heating due to the sheet charge density between AlGaN/GaN layers. (b) Zoomed view of the heat input deposited between the gate foot and the drain contacts due to dominant Joule heating there at the given operation conditions.

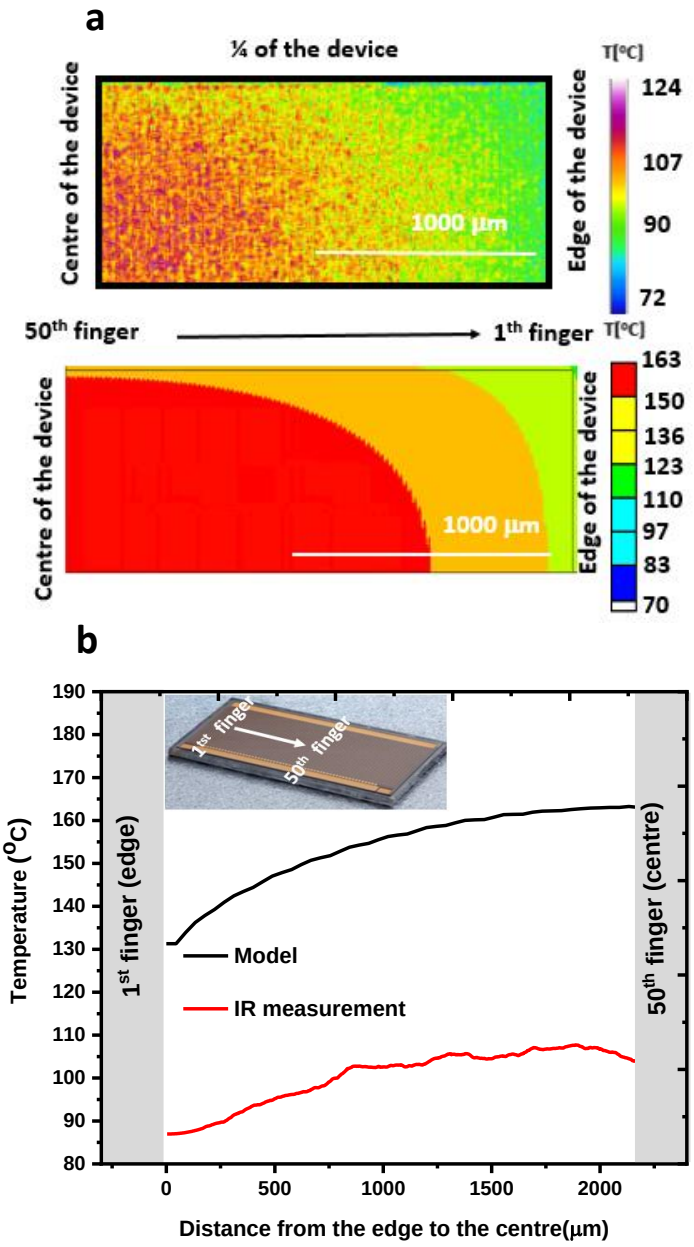

FIGURE 6.3. Thermal model and the verification of the heating profile assumption by IR thermography: (a) IR thermal image of the ≈ 4x1.2 mm^2 power device at V_{ds}=4 V, textitI$_{ds}$=5 A, V_{gs}=1.8 A, $T_{backplate}$=70^{o}C. A quarter of the geometry was imaged. The equivalent thermal simulation results based on the assumed heating profile is shown in (b). One quarter of the device was simulated due to symmetric boundary conditions in order to reduce the computational effort. (b) Line profiles of the IR measurements and the thermal model in (a), showing the the temperature profile (of the channel) from the edge of the device to the centre.

which can be accounted for by a change in the wafer-chuck thermal contact resistance and the underestimation of temperature due to transparent substrate as discussed previously. For a more quantitative investigation, subsequent Raman thermography measurements were performed at power dissipations of $P_{diss} \approx$ 10, 15, 20 and 25 W and chuck temperature of 25^{o}C. In this case the wafer temperature was measured ≈300 μm away from the active region, where only wafer-to-chuck contact resistance would affect the temperature rise, and used to calibrate the thermal model wafer-chuck conductance, which was estimated as 3500 W/m^{2}K. Figure 6.4(a) shows that the simulated temperature distribution reasonably matches the measured Raman thermography distribution, verifying the model calibration. Based on the thermal model, ΔT between the GaN and Si is <1^o C owing to the low local channel heat flux, as shown in Figure 6.4(b). This is because the device area is large, despite the relatively high power dissipation in this measurement; for measurement purposes the GaN and Si temperature can be treated as equal during steady state heating. It is also apparent in Figure 6.4(a) that the temperature non-uniformity across the channel becomes significant as power dissipation increases, which should be taken into consideration during the design stage as large temperature gradients across the channel might be a reliability issue, for example due to non-uniform thermal expansion of the device. This could even induce cracking if the temperature gradients are too large such that tensile and compressive stresses do not balance each other and the net stress exceeds the critical stress of the channel material. This non-uniform temperature distribution is also the reason of non-uniform current distribution in the channel due to the temperature dependence of carrier mobility.

Figure 6.4(b) shows the simulated depth temperature profile from the channel to the substrate. We observe that for steady state heating, the relative thermal resistance of the GaN and strain relief layer are negligible with respect to the substrate and chuck thermal resistance. This means that TBR$_{eff}$ between the channel and the substrate is not critical for large-area power devices, unlike suggested by [187]. This is because although the total power dissipation is high, it is distributed over a large area. The simulations shown in Figure 6.4(b) indicates that it is the substrate resistance that is critical as the power density increases, reaching up to ≈50^{o}C for a power density of 0.33 W/mm, corresponding to P_{diss}=40 W for the 100-finger-device measured

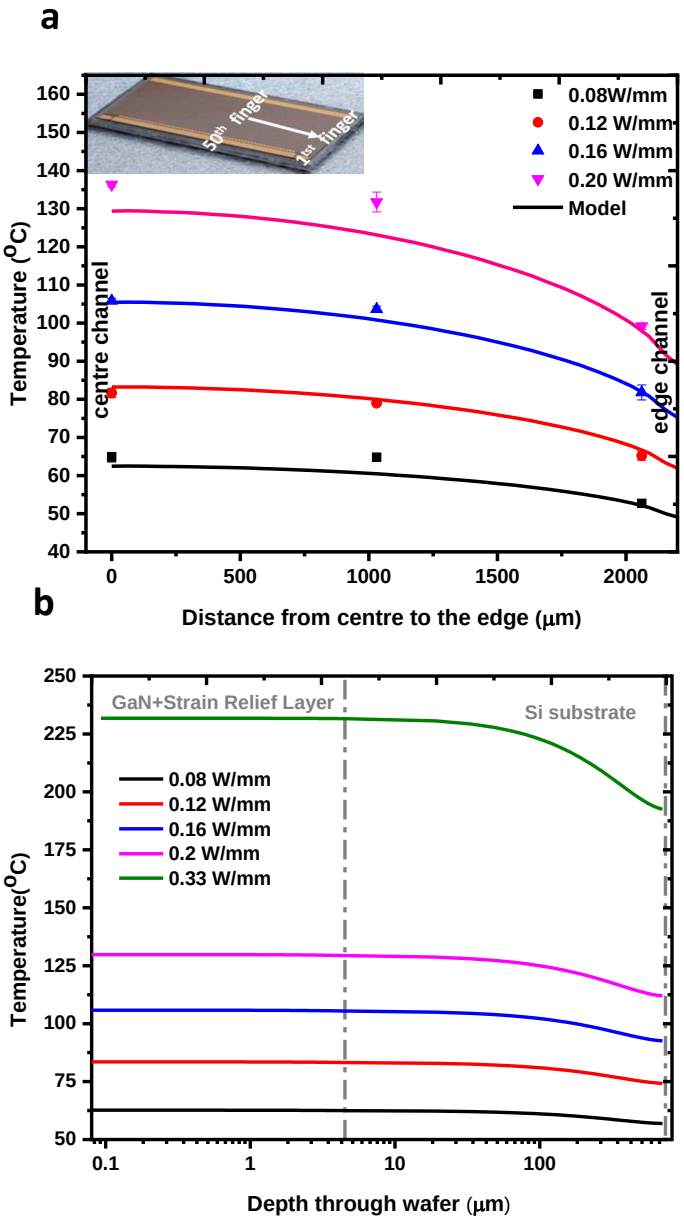

FIGURE 6.4. (a) Simulated and measured temperature distributions of the channel at various power densities. The figure shows half of the channel, from the centre channel to edge channel as shown in the inset. Back plate temperature is set to 25^{o}C. (b) Simulated depth temperature profiles through the GaN/SRL layers and Si substrate, based on more accurate Raman thermography measurements. The back side of the chuck is fixed at 25^{o}C and the wafer-to-chuck thermal contact resistance is 3500 W/m^{2}K, illustrating that largest ΔT component is at the wafer-to-chuck interface.

in this work. We also investigated how the substrate resistance varies with different device dimensions by simulating different sized devices at the same experimental conditions with that of Raman thermography measurements, for a power density of 0.33 W/mm. Figure 6.5(a) supports our conclusion that substrate thermal resistance becomes more significant as the device area increases, showing that it can triple when the number of fingers increases from 25 to 100. This highlights that the thermal strategy adopted could change when combining small devices in parallel or using a single power device. For the former one, substrate resistance might not be as critical as for the latter one. However, TBR_{eff} due to the interface between the channel and substrate would be still negligible.

The above-mentioned findings indicate that strategies such as substrate thinning (reducing the heat path length through the silicon) can be a beneficial and low cost strategy for large

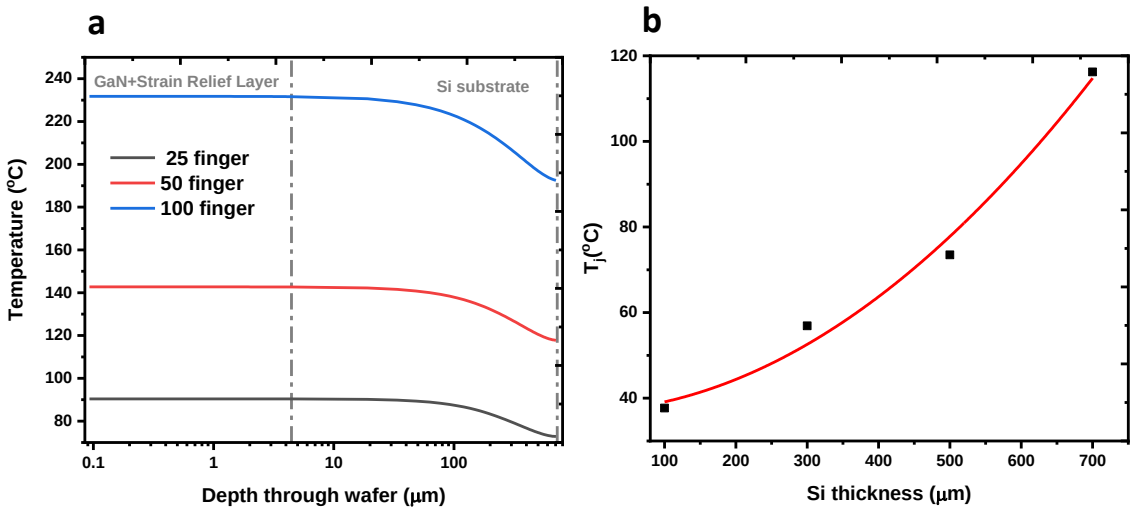

FIGURE 6.5. The effect of device geometry on the temperature rise: (a) The effect of device size on the substrate resistance. Back plate temperature is set to 25^{o}C, a power density of 0.33 W/mK was considered. The estimated thermal contact resistance of 3500 W/m^{2}K was considered between the wafer and the substrate. (b) The effect of substrate thickness on the junction temperature, T_j, when the back of the substrate is subjected to a cold reservoir (no contact resistance) at 25^{o}C, for a power density of 0.33 W/mK, for 100-finger-device.

area GaN power devices. We quantified how much thinning the substrate can affect the junction (peak) temperature by simulating the same 100-finger-on-wafer device by subjecting the back of the substrate to a cold reservoir at 25 ^{o}C (no thermal resistance between the heat sink and the substrate). Figure 6.5(b) shows that it is possible to decrease the junction temperature x3, by thinning the 700 μm-substrate to 100 μm, if the substrate is close to an ideal (no contact resistance) heat sink. These findings also indicates that the wafer-to-chuck thermal resistance (or packaging) is likely to be the main factor determining the thermal resistance of large area devices, considering that wafer-to-chuck thermal resistance could increase the peak temperature by ≈100%, as shown in Figure 6.5(a)-(b) for a 100-finger device.

6.3 Conclusion

As a result of the combined experimental and thermal modeling approach, thermal bottlenecks of a multi-finger lateral GaN power device at the device level were identified as the substrate. SRL contribution was found to be negligible for such large area devices due to lower power densities despite higher absolute power dissipations compared to their RF counterparts, where the channel lengths are on the order of several μm and the widths are on the order of 100s of μm. We also identified that increased power densities might lead to non-uniform channel temperatures across the device, which could be a potential reliability issue and need to be considered during the design stage and can be circumvented by designing the devices with varying gate pitches to engineer the heat transfer path between the adjacent device fingers. These findings highlight that the optimum thermal management strategy would be thinning the substrate at the device level. However, it is critical that the ultimate decision be made by considering both electro-thermal performance, taking the breakdown strength of the thinner substrate into account. We also pointed out that SRL contribution to the thermal resistance is negligible even when number of device fingers decreases to its one fourth; however, the contribution of substrate to the thermal resistance decreases in that case. Therefore, the thermal strategy adopted at the device level might differ when a multiple power devices are used in parallel rather than a single larger one.

CHAPTER 7

CONCLUSION AND FUTURE WORK

Wide band gap devices, in particular GaN HEMTs, have already started replacing the mature Si transistors; although with a small market share of 10% as of now. However, they have not reached their full potential yet and require optimisation of the design and technology integration to increase their reliability. It is clear that addressing these challenges require a holistic approach, which assesses the device design, fabrication and reliability from both electrical and thermal viewpoint. This thesis focused only on the thermal aspects, which seems to be usually tempting to be overlooked by the device designers yet very crucial for the long-term reliability.

As the reliable assessment of the thermal performance of the device, which is directly linked to its lifetime, requires an accurate and practical thermal metrology, which seems to be lacking in the industry at the moment, we focused on the development of the new wide field, sub-micron resolution, surface sensitive thermography technique with a one-off calibration. We combined highly efficient quantum rod emitters as the surface temperature sensors and a hyperspectral camera equipment as the detector. We showed the feasibility of this technique, hyperspectral quantum rod thermal imaging (HQTI), in Chapter 4 successfully on a GaN HEMT. The temperature precision of the current set-up is $\approx 4\ ^{o}$C. We demonstrated ≈700-800 nm lateral optical resolution; the depth resolution is determined by the thickness of the quantum rod coating.

The results showed a very close agreement with the well-established nanoparticle assisted Raman thermography. A calibrated thermal model also supported the accuracy of our approach. We highlighted the importance of an accurate thermography tool by benchmarking it against the standard IR thermography: IR thermography was found to underestimate the device temperature by ≈60% compared to HQTI measurements, due to lateral and depth averaging. We demonstrated that the quantum rod coating layer affects neither DC characteristics of the device nor its thermal performance due to the existence of the passivation layer and the small thickness of the the coating layer which is on the order of <≈500 nm. Currently, the quantum rods are susceptible to photoblinking at high temperatures due to increasing non-radiative recombination rates. We quantified that the signal to noise ratio decreases by a factor of 10 due to this reversible change in the emission intensity at a typical operating temperature of GaN HEMTs, i.e. ≈ 155 ^{o}C, compared to its room temperature value. This might increase the acquisition time of the measurement at even higher temperatures if the signal to noise ratio is not enough to recover the temperature map. We also noted that external electric field can cause a shift in the peak emission wavelength of the quantum nanopartıcles sensors due to Quantum Confined Stark Effect; yet, this effect was found to be non-measurable for the ensemble of the quantum nanorods distributed in random orientations, both in the literature [166] and in this work. It was highlighted that the reason of this observation was attributed to the reverse orientations of the nanorods (with respect to the direction of the external electric field) within the ensemble such that the Stark shifts in the opposite directions due to the reverse orientation cancel each other, and does not exhibit a measurable effect on the peak emission wavelength. However, Stark effect contributions might need to be considered for the ensemble of quantum dots for which the Stark effect would be red-shifted, independent of the orientation of the nanoparticles, or for single isolated nanoparticle measurements (either rods or dots). In that case, this effect can be circumvented if the reference condition is set to pinched-OFF state, rather than the OFF state, if the surface electric field is high; as the surface electric field would be similar to the ON state when the device is at the pinched-OFF state (at the same drain-source voltage with that of ON state), considering that the electric field due to gate voltage is negligible. HQTI technique is advantageous compared to standard thermography techniques as it requires only one-off, equipment dependent calibration.

Although we demonstrated the technique on a GaN HEMT, it is easily applicable to other wide band gap or ultra wide band gap materials. When applied to materials, the band gap of which is smaller than the energy of the excitation light, optical absorption by the sample needs to be given special care as the photoluminescence signal from the sample might interfere with the quantum rod emission. By the introduction of this technique, it is possible to measure temperature of various surfaces such as metals, semiconductors or insulators with a single technique, at the sub-micron resolution and with high accuracy.

As a logical next step, the steady state HQTI technique was extended for time resolved measurements (T-HQTI) by implementing boxcar averaging approach. We demonstrated 20 μs time resolution due to the limitations of our hardware. The results were verified with a combined implementation of nanoparticle assisted transient Raman thermography and TTR. The ultimate time resolution achievable with the T-HQTI measurements is limited by the radiative life-time (relaxation time) of the QRs and can be extended down to 10 ns for the QRs considered here with small modifications in the test set-up, such as using a higher power LED or a CCD with a higher quantum efficiency. It is also possible to decrease the time resolution below the radiative recombination limit of the QRs, depending on the application, using time-gated scientific cameras with ps frame rates. This development can be a valuable substitute of the current transient thermography techniques. For example, compared to the transient Raman thermography (depending on the material under test) acquisition times are several orders of magnitude shorter with T-HQTI and no scanning is required due to the high signal-to-noise ratio of quantum rod emission. More importantly, compared to TTR which is a faster technique, the interpretation of the data is more straight forward, as the nanoparticles themselves are free from temperature gradient effects, which actually can decrease accuracy of standard TTR measurements due to the different refractive index between TTR calibration and TTR measurements during device operation. It also circumvents interference related inaccuracy of TTR measurements. However, the thermal contact resistance between the surface of the device and the coating layer needs to be minimized to fully exploit the benefits of this technique. In this work, we showed that in the >100 MHz operating regime, the thermal contact resistance does not have an impact on the temperature measurements. However, for shorter time scales, even in the 10 MHz range, it is

important to consider the effects of the thermal contact resistance between the sensors and the DUT, for a reliable interpretation of temperature measurements.

We note that although we considered only device applications in this work, it is possible to apply this technique on different mediums such as biomedical applications where the sub-micron resolution temperature measurements in a living body could be of interest. In that case, the bio-compatible nanoparticles, such as carbon dots, can be injected into the body and by using a simple hyperspectral camera and a low power density light source, temperature can be monitored.

In Chapter 6, we looked at the thermal bottlenecks for large area multi-finger power devices to identify the best possible strategy for thermal management. We have found out that strain relief layer does not contribute to the thermal resistance of power devices because of the large area being heated, which results in low power densities on the order of ≈ 0.1 W/mm s even if the peak temperature exceeds 100 ^{o}C. This is different from the widely studied RF devices where the same peak temperature is reached as a result of higher power densities on the order of 10s of W/mm. In RF devices, the heat diffuses towards the substrate (out-of-plane); whereas, it diffuses laterally (in-plane) in power devices. Therefore, SRL contribution to the thermal resistance is negligible in power devices whereas it is widely known that SRL is a thermal bottleneck for RF devices due to high power densities. We also identified that at high power densities, non-uniform temperature distribution across the channel can be a reliability concern. The thermal bottleneck of large area power devices was found to be the substrate, at the device level. We showed that the contribution of the substrate to the thermal resistance increases when the device increases (by adding more fingers); however, the SRL contribution still remains insignificant. We suggested that thinning the substrate can be a cost effective solution to reduce the device temperature. This suggestion was backed up by simulations, which show that thinning a 700 μm Si wafer to 100 μm, can decrease the peak temperature to its one third. However, an efficient substrate cooling is critical to achieve this performance improvement, meaning that the heat path from the substrate to the cooler should be as less resistive as possible.

7.1 Future Work

From the technique point of view, future work for Chapter 4 can focus on pushing the optical resolution limits to nm range in order to fully exploit small size of single quantum rods, or alternatively quantum dots. This limit can be pushed by applying already established super resolution (SR) imaging techniques, which enable beating the diffraction limited optical resolution. From the hardware point of view, super resolution can be achieved, for example, by near field imaging [188, 189]. However, near field optical microscopy requires a very small optical aperture, the dimensions of which are much smaller than the excitation wavelength, for example on the order of 10s of nm [189]. Fabrication of such a small aperture would be a costly endeavour. Alternatively, the optical diffraction limits can be bet by low-cost software solutions which can provide super resolution images [190–193]. The idea behind the computational SR imaging is the recovery of the original image with a resolution higher than the diffraction limit from a series of low resolution (LR) images, which are the convoluted response of the point spread function (PSF) of the imaging system and the actual scene (with an additional system noise). This problem can be formulated as a linear inverse problem, i.e. SR image= PSF ·LR image+ noise. The challenge of solving this equation lies in the fact that PSF is usually a singular matrix, which is not directly invertible. Therefore, achieving a unique and stable solution is challenging and requires the regularisation of this formulation, which can be performed by either deterministic or statistical approach based on the prior knowledge of the system under study. This area of research dates back to late 1980s and many algorithms have been proposed for the SR image reconstruction, one of the latest applications on biological imaging using quantum dots can be found in Ref. [193], where x7 resolution improvement has been demonstrated and supported by AFM images. It would be an interesting next step to extend computational SR imaging for thermography applications, and in particular for HQTI. This would be a very useful tool for the next generation electronic devices, considering the fact that the channel dimensions are being pushed down to 100s of nanometers. This would also require a more uniform distribution of the isolated quantum rods. Achieving such a uniform distribution was experienced to be challenging in this work; however, the author thinks that it is not impossible. For example, inkjet printing, which is widely

used for the fabrication of organic LEDs, can be given a try for the QR deposition. It would be also useful to test whether/how much RF characteristics are affected by the QR deposition to identify the limits of the technique.

The future work for Chapter 5 can focus on pushing the time resolution limits with this technique. This approach can also be used for thermal property estimation; especially thermal diffusivity of materials if the time resolution limits is improved by implementing above-mentioned ideas.

Future work for Chapter 6 can focus on identifying the most cost effective packaging solutions for power devices. This would require as less interface as possible within the package material. The thermal bottlenecks for the pulsed operation should also be assessed for the full picture, both at the package and the device level.

APPENDIX A

ERROR ANALYSIS AND SUPPORTING DATA FOR THE HQTI SYSTEM

A.1 Error Analysis

This section of the appendix describes the error analysis for the Hyperspectral Quantum Thermal Imagining (HQTI) system developed in Chapter 4, which was published as a Supplementary Material in our recent work, Ref. [124] [1].

The uncertainty includes both the systematic errors and the random errors. We analysed these two contributions separately. Figure 4.23(b) in Chapter 4 shows that there is no temperature offset at zero power dissipation, i.e. ΔT=0 as expected. This is an indication of the negligible systematic errors compared to the random errors.

In order to estimate the accuracy of the mean temperature calculation and our image processing approach, a Kernel distribution (non-parametric distribution) shown in Figure 4.17 in Chapter 4 was fitted to the histogram using MATLAB Distribution Fitting application and a mean temperature of ~20 ^{o}C with a standard deviation (σ) of 8 ^{o}C was obtained (using the mean values of the calibration function), as explained in Chapter 4. Central limit theorem says that the distribution function of the "sample" mean is a normal distribution with a standard deviation

[1] *Reproduced in part with permission from ACS Appl. Electron. Mater. 2, 1, 93–102, Oner, B. et al., Submicrometer Resolution Hyperspectral Quantum Rod Thermal Imaging of Microelectronic Devices, Copyright (2020), American Chemical Society.*

of $\sigma/\sqrt{n}$, where σ is the standard deviation of the "population" mean and n is the sample size [194]. The sample size is equal to 7 for the data presented in this work. Therefore, the standard error of the "sample" mean is equal to $\sigma/\sqrt{n}$. If the information of the whole population is known, then the statistical uncertainty is σ. As this analysis (the analysis shown in Figure 4.17) was performed for a sufficiently large number of pixels, i.e. for full image size which consists of 520x696 pixels, with a non-Gaussian distribution (Kernel fitted), we consider the estimated mean as the "population" mean here, rather than the "sample" mean, i.e., the population representing all the pixels of the image where the image processing performed. Therefore, we reported the standard deviation rather than the standard error of the mean for this analysis. The resulting estimation of 20^oC with an 8^oC standard deviation covers the set temperature of 25^oC. Ideally, the offset in the room temperature can be corrected to circumvent systematic errors; however, we do not need to because the standard deviation of 8^oC already covers the room temperature. This analysis also indicates that systematic errors are negligible in the system developed.

Errors in the calibration function coefficients due to the fitting were also assessed as another source of uncertainty, other than random statistical errors. Its effect on the temperature measurements were estimated for a representative example: the deviation of the mean temperature estimations were calculated at each pixel by applying the upper and lower limits of the calibration function, which results in a variation of $\pm 7\ ^oC$ for a sample size of n=3 measurements for the device and operating conditions presented in Figure 4.22- 4.23(b) (for an absolute device surface temperature of ~90 ^oC). This value is within the precision of the measurement for n=3 sample (~7 ^oC) and indicates that the error contribution from calibration function fitting is small. This also led to the conclusion that the systematic errors are small in the developed system at these measurement conditions compared to the random errors. Therefore, we only report statistical random errors in this work ,i.e. this is what the error bars in Figure 4.23 and Figure 5.7 represent, which also correspond to the precision of the measurement.

Increasing the number of successive measurements (n) increases the precision by $1/\sqrt{n}$ because the precision of temperature estimation at a particular pixel is defined as the standard deviation of the population mean temperature at that pixel, divided by the square root of the number of measurements, i.e.$\sigma/\sqrt{n}$ which corresponds to the standard deviation of the "sample"

mean from the “population” mean. The temperature estimations reported in this work represent this sample mean over n=7 successive measurements and the error associated with this indicates the deviation of the sample mean from the population mean.

A.2 Supporting Data

A.2.1 Thermal Image and Noise for a Single Acquisition

Figure A.1(a)-(b) shows the HQTI maps obtained from a single acquisition. It can be seen that the number of data in the thermal map shown in Figure A.1(b) is lower than that of (a), which implies that the noise in the image for Figure A.1(b) was higher initially than that of (a) and was reduced by eliminating the noisy pixels during data processing. The apparent noise in both images also highlights the necessity of averaging for a "cleaner" image, as done in Figure 4.18(b)-(d) and Figure 4.23(a). Figure A.1 also gives insights into the source of noise in the thermal maps, in

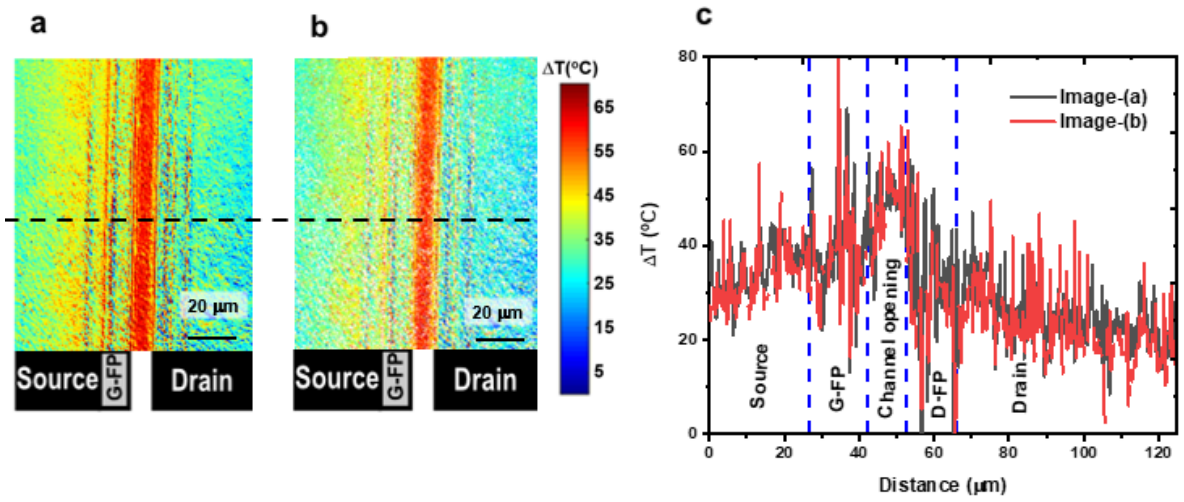

FIGURE A.1. HQTI noise for a single image acquisition, before averaging, for the data presented in Figure 4.18(d) (which represents the mean of n=7 successive measurements). The back plate temperature is 25^{o}C; the device is biased at V_{ds}=10 V, I_{ds}=83.2 mA, P_{diss}=4.165 W/mm: (a) Thermal map for a single acquisition, at n=1. (b) Thermal map for a single acquisition, at n=7. (c) Temperature line profiles for (a) and (b) along the dashed line. The line profile represents the temperature values at a single pixel across the device channel, indicating the noise in the images in the absence of averaging.

terms of whether it is a fixed pattern noise or random noise. The line profile in Figure A.1(c) , although noisy due to the lack of averaging, shows that the noise is of a fixed pattern at the fine edges of the source and drain connected field plates as well as at the edges between the semiconductor and the metal (See the optical image of the DUT in Figure 4.18(a) for the details of the field plate metal features). Temperature sharply drops at these regions, rather than decaying smoothly. This sharp drop in the temperature measurements at the edges is partly attributed to the edge effects, which is observed because the distance between the two materials at the edges is smaller than the diffraction limit and the signal is coupled there. Similar observations were also made in the literature for other thermal imaging techniques, such as thermoreflectance [195]. Besides, slight drifts of the sample during the tests might also exacerbate the noise at the edges. Even though we have not observed a drift in the images within a pixel size, which corresponds to 180 nm in our system, as mentioned in Chapter 4, the drifts at the sub-pixel levels might contribute to the noise at the edges. For these reasons, the temperature measurements at the edges should be assessed with caution.

APPENDIX B

PUBLICATIONS AND CONFERENCES ATTENDED

B.1 Publications

- **B.Öner**, J.W. Pomeroy, M. Kuball, Submicrometer resolution hyperspectral quantum rod thermal imaging of microelectronic devices, *ACS Appl. Electron. Mater.*, 2, 1, pp.93-102, 2020.

- **B.Öner**, J.W. Pomeroy, M. Kuball, Time resolved hyperspectral quantum rod thermography of microelectronic devices: Temperature transients in a GaN HEMT, *IEEE Elect. Device Lett.*, 41, 6, pp.812-815, 2020.

- M. Kuball, J.W. Pomeroy, F. Gucmann, **B.Öner**, Thermal analysis of semiconductor devices and materials - Why should I not trust a thermal simulation?, *Proceedings of IEEE BiCMOS and Compound semiconductor Integrated Circuits and Technology Symposium (BCICTS)*, Nashville, TN, USA, 2019.

B.2 Conference Presentations

- **B.Öner**, J. W. Pomeroy, M. Kuball. Hyperspectral quantum rod thermal imaging of GaN electronic devices, *MRS Fall Meeting*, Boston, US, 2018.

- J. W. Pomeroy, M. Kuball, **B.Öner**. Advances in sub-micron and nanosecond resolution thermal characterization of wide band gap semiconductor devices and materials, *(invited talk)*, *MRS Fall Meeting*, Boston, US, 2018.

- M. Kuball, J. W. Pomeroy, F. Gucmann, **B.Öner**. Thermal analysis of semiconductor devices and materials - Why should I not trust a thermal simulation?, *IEEE BCICTS*, Nashville, TN, US, 2019.

BIBLIOGRAPHY

[1] W. Brattain, "Bell labs logbook," pp. 7–8, 1947, last accessed 1 July 2020. [Online]. Available: https://www.pbs.org/transistor/science/labpages/labpg5

[2] J. Bardeen and W. H. Brattain, "The transistor, a semiconductor triode," *Physical Review*, vol. 74, no. 12, pp. 230–231, 1948.

[3] M. Tanenbaum, L. B. Valdes, E. Buehler, and N. B. Hannay, "Silicon n-p-n grown junction transistors," *Journal of Applied Physics*, vol. 26, no. 6, pp. 686–692, 1955.

[4] N. Dahad, "Semiconductor industry to rebound in 2020 with 4% growth," 2019, last accessed 10 February 2020. [Online]. Available: https://www.eetimes.com/semiconductor-industry-to-rebound-in-2020-with-4-growth

[5] C. A. Mead, "Schottky barrier gate field effect transistor," *Proceedings of the IEEE*, vol. 54, no. 2, p. 307–308, 1966.

[6] U. K. Mishra, P. Parikh, and Y. F. Wu, "AlGaN/GaN HEMTs - An overview of device operation and applications," *Proceedings of the IEEE*, vol. 90, no. 6, pp. 1022–1031, 2002.

[7] M. Takashi, H. Satoshi, F. Toshio, and N. Kazuo, "A new field-effect transistor with selectively doped GaAs /n-$Al_xGa_{1-x}As$ Heterojunctions," *Japanese Journal of Applied Physics*, vol. 19, no. 5, pp. 225–227, 1980.

[8] J. Y. Tsao, S. Chowdhury, M. A. Hollis, D. Jena, N. M. Johnson, K. A. Jones, R. J. Kaplar, S. Rajan, C. G. Van de Walle, E. Bellotti, C. L. Chua, R. Collazo, M. E. Coltrin, J. A. Cooper, K. R. Evans, S. Graham, T. A. Grotjohn, E. R. Heller, M. Higashiwaki, M. S.

Islam, P. W. Juodawlkis, M. A. Khan, A. D. Koehler, J. H. Leach, U. K. Mishra, R. J. Nemanich, R. C. Pilawa-Podgurski, J. B. Shealy, Z. Sitar, M. J. Tadjer, A. F. Witulski, M. Wraback, and J. A. Simmons, "Ultra wide-bandgap semiconductors: research opportunities and challenges," *Advanced Electronic Materials*, vol. 4, no. 1, 2018.

[9] S. Nakamura and M. R. Krames, "History of gallium-nitride-based light-emitting diodes for illumination," *Proceedings of the IEEE*, vol. 101, no. 10, pp. 2211–2220, 2013.

[10] M. Asif Khan, A. Bhattarai, J. N. Kuznia, and D. T. Olson, "High electron mobility transistor based on a GaN-$Al_xGa_{1-x}N$ heterojunction," *Applied Physics Letters*, vol. 63, no. 9, pp. 1214–1215, 1993.

[11] C. J. Hodges, "An optical study of III-nitride semiconductor devices, their thermal properties and degradation mechanisms," Ph.D. dissertation, University of Bristol, 2014.

[12] A. Letellier, M. R. Dubois, J. P. Trovao, and H. Maher, "Gallium nitride semiconductors in power electronics for electric vehicles: advantages and challenges," *2015 IEEE Vehicle Power and Propulsion Conference, VPPC 2015 - Proceedings*, pp. 1–6, 2015.

[13] U. E. I. Administration, "International energy outlook 2016," 2016, last accessed 1 February 2020. [Online]. Available: https://www.eia.gov/outlooks/ieo

[14] I. C. Kizilyalli, E. P. Carlson, D. W. Cunningham, J. S. Manser, and A. Y. Liu, "Wide band-gap semiconductor based power electronics for energy efficiency," 2018, last accessed 10 February 2020. [Online]. Available: https://arpa-e.energy.gov/sites/default/files/documents/files/ARPA-E_Power_Electronics_Paper-April2018.pdf

[15] G. Longobardi, "GaN for power devices: Benefits, applications, and normally-off technologies," in *Proceedings of the International Semiconductor Conference(CAS)*, Sinaia, 2017, pp. 11–18.

[16] H. Amano, Y. Baines, E. Beam, M. Borga, T. Bouchet, P. R. Chalker, M. Charles, K. Chen, N. Chowdhury, R. Chu, C. De Santi, M. De Souza, S. Decoutere, L. Di Cioccio, B. Eckardt, R. Egawa, P. Fay, J. Freedsman, L. Guido, O. Häberlen, G. Haynes, T. Heckel,

D. Hemakumara, P. Houston, J. Hu, M. Hua, Q. Huang, A. Huang, S. Jiang, H. Kawai, D. Kinzer, M. Kuball, A. Kumar, K. B. Lee, X. Li, D. Marcon, M. März, R. McCarthy, G. Meneghesso, M. Meneghini, E. Morvan, A. Nakajima, E. Narayanan, S. Oliver, T. Palacios, D. Piedra, M. Plissonnier, R. Reddy, M. Sun, I. Thayne, A. Torres, N. Trivellin, V. Unni, M. Uren, M. Van Hove, D. Wallis, J. Wang, J. Xie, S. Yagi, S. Yang, C. Youtsey, R. Yu, E. Zanoni, S. Zeltner, and Y. Zhang, "The 2018 GaN power electronics roadmap," *Journal of Physics D: Applied Physics*, vol. 51, no. February, p. 163001, 2018.

[17] A. Sarua, H. Ji, M. Kuball, M. J. Uren, T. Martin, K. J. Nash, K. P. Hilton, and R. S. Balmer, "Piezoelectric strain in AlGaN/GaN heterostructure field-effect transistors under bias," *Applied Physics Letters*, vol. 88, no. 10, pp. 103 502–1–103 502–3, 2006.

[18] J. W. Pomeroy, M. J. Uren, B. Lambert, and M. Kuball, "Operating channel temperature in GaN HEMTs: DC versus RF accelerated life testing," *Microelectronics Reliability*, vol. 55, no. 12, pp. 2505–2510, 2015.

[19] G. D. Via, "GaN reliability - Where we are and where we need to go," in *CS MANTECH 2014 - 2014 International Conference on Compound Semiconductor Manufacturing Technology*, Denver,Colorado, USA, 2014, pp. 15–18.

[20] M. Power, "Characterisation of temperature and mechanical stress in AlGaN / GaN devices designed for power electronic applications," Ph.D. dissertation, University of Bristol, 2016.

[21] B. Lambert, J. Thorpe, R. Behtash, B. Schauwecker, F. Bourgeois, H. Jung, J. Bataille, P. Mezenge, C. Gourdon, C. Ollivier, D. Floriot, and H. Blanck, "Reliability data's of 0.5 μm AlGaN/GaN on SiC technology qualification," *Microelectron. Reliab.*, vol. 52, no. 9-10, pp. 2200–2204, 2012.

[22] J. Kuzmík, P. Javorka, A. Alam, M. Marso, M. Heuken, and P. Kordoš, "Determination of channel temperature in AlGaN/GaN HEMTs grown on sapphire and silicon substrates using DC characterization method," *IEEE Transactions on Electron Devices*, vol. 49, no. 8, pp. 1496–1498, 2002.

[23] G. Pavlidis, D. Kendig, E. R. Heller, and S. Graham, "Transient thermal characterization of AlGaN/GaN HEMTs under pulsed biasing," *IEEE Transactions on Electron Devices*, vol. 65, no. 5, pp. 1753–1758, 2018.

[24] J. Joh, J. A. Del Alamo, U. Chowdhury, T. M. Chou, H. Q. Tserng, and J. L. Jimenez, "Measurement of channel temperature in GaN high-electron mobility transistors," *IEEE Transactions on Electron Devices*, vol. 56, no. 12, pp. 2895–2901, 2009.

[25] P. W. Webb, "Thermal imaging of electronic devices with low surface emissivity," *Circuits, Devices and Systems, IEE Proceedings G*, vol. 138, no. 3, pp. 390–400, 1991.

[26] D. L. Blackburn and G. NBS, "A review of thermal characterization of power transistors," *Fourth Annual IEEE Semiconductor Thermal and Temperature Measurement Symposium*, pp. 1–7, 1988.

[27] N. Killat, "Reliability: Thermal and electrical challenges in AlGaN/GaN high electron mobility transistors," Ph.D. dissertation, University of Bristol, 2012.

[28] C. H. Oxley and R. H. Hopper, "Effect of transparency within a semiconductor on emissivity mapping for thermal profile measurements of a semiconductor device," *IET, Science, Measurement Technology*, vol. 1, no. 2, pp. 79–81, 2007.

[29] M. Kuball and J. W. Pomeroy, "A review of Raman thermography for electronic and opto-electronic device measurement with sub-micron spatial and nanosecond temporal resolution," *IEEE Transactions on Device and Materials Reliability*, vol. 16, no. 4, pp. 667–684, 2016.

[30] R. B. Simon, J. W. Pomeroy, and M. Kuball, "Diamond micro-raman thermometers for accurate gate temperature measurements," *Applied Physics Letters*, vol. 104, no. 21, pp. 213 503–1–213 503–4, 2014.

[31] P. Gu, Y. Zhang, Y. Feng, T. Zhang, H. Chu, T. Cui, Y. Wang, J. Zhao, and W. W. Yu, "Real-time and on-chip surface temperature sensing of GaN LED chips using PbSe quantum dots," *Nanoscale*, vol. 5, p. 10481–10486, 2013.

[32] D. G. Cahill, K. E. Goodson, and A. Majumdar, "Thermometry and thermal transport in micro/nanoscale solid-state devices and structures," *Journal of Heat Transfer*, vol. 124, no. 2, p. 223, 2002.

[33] J. Christofferson and A. Shakouri, "Thermoreflectance based thermal microscope," *Rev. Sci. Instrum.*, vol. 76, pp. 024 903–1–024 903–6, 2005.

[34] K. Maize, A. Ziabari, W. D. French, P. Lindorfer, B. O'Connell, and A. Shakouri, "Thermoreflectance CCD imaging of self-heating in power MOSFET arrays," *IEEE Trans. Electron Devices*, vol. 61, pp. 3014–3053, 2014.

[35] S. Gomes, A. Assy, and P. O. Chapuis, "Scanning thermal microscopy: A review," *Phys.Status Solidi A.*, vol. 212, pp. 477–494, 2015.

[36] L. Shi, S. Plyasunov, A. Bachtold, P. L. McEuen, and A. Majumdar, "Scanning thermal microscopy of carbon nanotubes using batch-fabricated probes," *Appl.Phys.Lett.*, vol. 77, pp. 4295–4297, 2000.

[37] J. Bodzenta, J. Juszczyk, A. Kazmierczak-Balata, P. Firek, A. Fleming, and M. Chirtoc, "Quantitative thermal microscopy measurement with thermal probe driven by dc+ac current," *Int. J Thermophy.*, vol. 37:73, pp. 1–17, 2016.

[38] P. Tovee, M. Pumarol, D. Zeze, K. Kjoller, and O. Kolosov, "Nanoscale spatial resolution probes for scanning thermal microscopy," *Journal of Applied Physics*, vol. 112, pp. 114 317–1–114 317–11, 2012.

[39] J. C. Waters, "Accuracy and precision in quantitative flourescence microscopy," *Journal of Cell Biology*, vol. 185, pp. 1135–1148, 2009.

[40] P. T. Chin, T. Buckle, A. A. d. Miguel, S. C. Meskers, R. A. Janssen, and F. W. Leeuwen, "Dual-emissive quantum dots for multispectral intraoperative flourescence imaging," *Biomaterials*, vol. 31, pp. 6823–6832, 2010.

[41] J. Xiong, M. Zhao, X. Han, Z. Cao, X. Wei, Y. Chen, C. Duan, and M. Yin, "Real-time microscale temperature imaging at low cost based on flourescent intensity ratio," *Scientific Reports*, vol. 7, pp. 41 311–1–41 311–8, 2017.

[42] C. D. Brites, P. P. Lima, N. J. Silva, A. Millan, V. S. Amaral, F. Palacio, and L. D. Carlos, "Thermometry at the nanoscale," *Nanoscale*, vol. 4, pp. 4799–4829, 2012.

[43] C. K. Gan, Y. P. Feng, and D. J. Srolovitz, "First-principles calculation of the thermodynamics of Inx Ga1-x N alloys: Effect of lattice vibrations," *Physical Review B - Condensed Matter and Materials Physics*, vol. 73, no. 23, pp. 1–8, 2006.

[44] O. Ambacher, "Growth and applications of group III-nitrides," *Journal of Physics D: Applied Physics*, vol. 31, no. 20, pp. 2653–2710, 1998.

[45] M. Farahmand and K. Brennan, "Full band Monte Carlo comparison of wurtzite and zincblende phase GaN MESFETs," *Materials Research Society Symposium - Proceedings*, vol. 595, no. 3, pp. 493–497, 2000.

[46] I. Vurgaftman and J. R. Meyer, "Band parameters for nitrogen-containing semiconductors," *Journal of Applied Physics*, no. 94, pp. 3675–3696, 2003.

[47] F. Bernardini, V. Fiorentini, and D. Vanderbilt, "Spontaneous polarization and piezoelectric electric constants of III-V nitrides," *Phys. Rev. B*, no. 56, pp. R10 024– R10 027, 1997.

[48] D. Guerra, M. Saraniti, N. Faralli, D. K. Ferry, S. M. Goodnick, and F. A. Marino, "Comparison of N- and Ga- face GaN HEMTs through cellular Monte Carlo simulations," *IEEE Transactions on Electron Devices*, vol. 57, no. 12, pp. 3348–3354, 2010.

[49] J. W. Chung, E. L. Piner, and T. Palacios, "N-face GaN/AlGaN HEMTs fabricated through layer transfer technology," *IEEE Electron Device Letters*, vol. 30, no. 2, pp. 113–116, 2009.

[50] S. Bloom, "Band structures of GaN and AIN," *Journal of Physics and Chemistry of Solids*, vol. 32, no. 9, pp. 2027–2032, 1971.

[51] M. Suzuki, T. Uenoyama, and A. Yanase, "First-principles calculations of effective-mass parameters of AlN and GaN," *Physical Review B*, vol. 52, no. 11, pp. 8132–8139, 1995.

[52] M. Palummo, C. M. Bertoni, L. Reining, and F. Finocchi, "The electronic structure of gallium nitride," *Physica B: Physics of Condensed Matter*, vol. 185, no. 1-4, pp. 404–409, 1993.

[53] D. A. Neamen, *Semiconductor Physics and Devices: Basic Principles*. McGraw Hill, 2012.

[54] C. Bungaro, K. Rapcewicz, and J. Bernholc, "Ab initio phonon dispersions of wurtzite AlN, GaN, and InN," *Phys. Rev. B - Condens. Matter Mater. Phys.*, vol. 61, no. 10, pp. 6720–6725, 2000.

[55] G. Chen, *Nanoscale Energy Transport and Conversion: A Parallel Treatment of Electrons, Phonons, and Photons*. Oxford University Press, Inc., 2005.

[56] H. Harima, "Properties of GaN and related compounds studied by means of Raman scattering," *J.Phys.: Condens. Matter*, vol. 14, pp. R967–R993, 2002.

[57] H. Siegle, G. Kaczmarczyk, L. Filippidis, A. Litvinchuk, A. Hoffmann, and C. Thomsen, "Zone-boundary phonons in hexagonal and cubic GaN," *Phys. Rev. B - Condens. Matter Mater. Phys.*, vol. 55, no. 11, pp. 7000–7004, 1997.

[58] T. Mimura, "The early history of the high electron mobility transistor," *IEEE Transactions on Microwave Theory and Techniques*, vol. 50, no. 3, pp. 780–782, 2002.

[59] D. Garrido-DIez and I. Baraia, "Review of wide bandgap materials and their impact in new power devices," *Proc. 2017 IEEE Int. Work. Electron. Control. Meas. Signals their Appl. to Mechatronics, ECMSM 2017*, pp. 1–6, 2017.

[60] B. Ozpineci and L. M. Tolbert, "Comparison of wide-bandgap semiconductors for power electronics applications-Oak Ridge National Laboratory," pp. 1–34, 2003, last accessed 05 July 2020. [Online]. Available: http://web.ornl.gov/webworks/cppr/y2001/rpt/118817.pdf

[61] N. Donato, N. Rouger, J. Pernot, G. Longobardi, and F. Udrea, "Diamond power devices: State of the art, modelling and figures of merit," *Journal of Physics D: Applied Physics*, vol. 53, no. 093001(38p), 2020.

[62] D. Lubyshev, J. M. Fastenau, Y. Qiu, A. W. K. Liu, E. J. Koerperick, J. T. Olesberg, D. Norton, N. N. Faleev, and C. B. Honsberg, "MBE growth of Sb-based nBn photodetectors on large diameter GaAs substrates," in *Proc. SPIE 8704,Infrared Technology and Applications XXXIX*, vol. 8704, Baltimore, Maryland, United States, 2013.

[63] L. F. S. Alves, R. C. M. Gomes, P. Lefranc, R. D. A. Pegado, O. Jeannin, B. A. Luciano, and F. V. Rocha, "SiC power devices in power electronics : An overview," in *2017 Brazilian Power Electronics Conference (COBEP)*, Juiz de Fora, 2017.

[64] W. M. Waller, "Optimisation of AlGaN / GaN power devices," Ph.D. dissertation, University of Bristol, 2018.

[65] C. Middleton, "Optimising heat flow in high performance wide and ultra-wide bandgap devices: The application of diamond in heat spreading." Ph.D. dissertation, University of Bristol, 2019.

[66] Y. Yamamoto, T. Imai, K. Tanabe, T. Tsuno, Y. Kumazawa, and N. Fujimori, "The measurement of thermal properties of diamond," *Diam. Relat. Mater.*, vol. 6, no. 8, pp. 1057–1061, 1997.

[67] J. Cho, D. Francis, D. H. Altman, M. Asheghi, and K. E. Goodson, "Phonon conduction in GaN-diamond composite substrates," *Journal of Applied Physics*, vol. 121, no. 055105, pp. 055 105–1–055 105–9, 2017.

[68] O. Ambacher, J. Smart, J. R. Shealy, N. G. Weimann, K. Chu, M. Murphy, W. J. Schaff, L. F. Eastman, R. Dimitrov, L. Wittmer, M. Stutzmann, W. Rieger, and J. Hilsenbeck, "Two-dimensional electron gases induced by spontaneous and piezoelectric polarization charges in N- And Ga-face AIGaN/GaN heterostructures," *Journal of Applied Physics*, vol. 85, no. 6, pp. 3222–3233, 1999.

[69] T. Huang, A. Malmros, J. Bergsten, S. Gustafsson, O. Axelsson, M. Thorsell, and N. Rorsman, "Suppression of dispersive effects in AlGaN/GaN high-electron-mobility transistors using bilayer SiN," *IEEE Electron Device Lett.*, vol. 36, no. 6, pp. 537–539, 2015.

[70] S. Arulkumaran, G. I. Ng, K. Ranjan, G. Z. Saw, P. P. Murmu, and J. Kennedy, "Improved device isolation in AlGaN/GaN HEMTs on Si by heavy Kr+ Ion implantation," in *72th Device Research Conference - Conference Digest*, Santa Barbara, CA, USA, 2014, pp. 115–116.

[71] O. Ambacher, J. Majewski, C. Miskys, A. Link, M. Hermann, M. Eickhoff, M. Stutzmann, F. Bernardini, V. Fiorentini, V. Tilak, B. Schaff, and L. F. Eastman, "Pyroelectric properties of Al(In)GaN/GaN hetero- and quantum well structures," *Journal of Physics Condensed Matter*, vol. 14, no. 13, pp. 3399–3434, 2002.

[72] O. Ambacher, R. Dimitrov, M. Stutzmann, B. E. Foutz, M. J. Murphy, J. A. Smart, J. R. Shealy, N. G. Weimann, K. Chu, M. Chumbes, B. Green, A. J. Sierakowski, W. J. Schaff, and L. F. Eastman, "Role of spontaneous and piezoelectric polarization induced effects in group-III nitride based heterostructures and devices," *Physica Status Solidi (B) Basic Research*, vol. 216, no. 1, pp. 381–389, 1999.

[73] J. P. Ibbetson, P. T. Fini, S. P. Ness, K D.and DenBaars, J. S. Speck, and U. K. Mishra, "The source of electrons in AlGaN / GaN heterostructure field effect transistors," *Applied Physics Letter*, vol. 77, no. 2, pp. 250–252, 2000.

[74] H. W. Jang, C. M. Jeon, K. H. Kim, J. K. Kim, S. B. Bae, J. H. Lee, J. W. Choi, and J. L. Lee, " Mechanism of two-dimensional electron gas formation in $Al_xGa_{1-x}N$/GaN heterostructures," *Applied Physics Letter*, vol. 81, no. 7, p. 1249–1251, 2002.

[75] G. Greco, F. Iucolano, and F. Roccaforte, "Review of technology for normally-off HEMTs with p-GaN gate," *Materials Science in Semiconductor Processing*, vol. 78, pp. 96–106, 2018.

[76] F. Roccaforte, G. Greco, P. Fiorenza, and F. Iucolano, "An overview of normally-off GaN-based high electron mobility transistors," *Materials*, vol. 12, no. 1599, pp. 1–18, 2019.

[77] M. Meneghini, O. Hilt, J. Wuerfl, and G. Meneghesso, "Technology and reliability of normally-Off GaN HEMTs with p-type gate," *Energies*, vol. 10, no. 153, pp. 1–15, 2017.

[78] Y. Uemoto, M. Hikita, H. Ueno, H. Matsuo, H. Ishida, M. Yanagihara, T. Ueda, T. Tanaka, and D. Ueda, "Gate injection transistor(GIT)— A normally-off conductivity modulation," *IEEE Transactions on Electron Devices*, vol. 54, no. 12, pp. 3393–3399, 2007.

[79] S. Yang, C. Zhou, S. Han, J. Wei, K. Sheng, and K. J. Chen, "Impact of substrate bias polarity on buffer-related current collapse in AlGaN/GaN-on-Si power devices," *IEEE Transactions on Electron Devices*, vol. 64, no. 12, pp. 5048–5056, 2017.

[80] W. A. Melton and J. I. Pankove, "GaN growth on sapphire," *Journal of Crystal Growth*, vol. 178, no. 1-2, pp. 168–173, 1997.

[81] M. Khoury, O. Tottereau, G. Feuillet, P. Vennéguès, and J. Zúñiga-Pérez, "Evolution and prevention of meltback etching: Case study of semipolar GaN growth on patterned silicon substrates," *Journal of Applied Physics*, vol. 122, no. 10, pp. 105 108–1–105 108–7, 2017.

[82] F. Medjdoub, *Gallium nitride (GaN): physics, devices, and technology*. CRC, 2015.

[83] D. G. Cahill, W. K. Ford, K. E. Goodson, G. D. Mahan, A. Majumdar, H. J. Maris, R. Merlin, and S. R. Phillpot, "Nanoscale thermal transport," *Journal of Applied Physics*, vol. 93, no. 2, pp. 793–818, 2003.

[84] A. Sarua, H. Ji, K. P. Hilton, D. J. Wallis, M. J. Uren, T. Martin, and M. Kuball, "Thermal boundary resistance between GaN and substrate in AlGaN/GaN electronic devices," *IEEE Transactions on Electron Devices*, vol. 54, no. 12, pp. 3152–3158, 2007.

[85] R. Pelzel, "A comparison of MOVPE and MBE growth technologies for III-V epitaxial structures," *2013 International Conference on Compound Semiconductor Manufacturing Technology, CS MANTECH 2013*, vol. C, no. 610, pp. 105–108, 2013.

[86] E. Borovitskaya and M. S. Shur, "Low-dimensional systems," *International Journal of High Speed Electronics and Systems*, vol. 12, no. 1, pp. 1–14, 2002.

[87] M. Fox, *Optical Properties of Solids*. Oxford University Press, 2001.

[88] D. Bimberg, M. Grundmann, and N. N. Ledentsov, *Quantum Dot Heterostructures*. John Wiley Sons, 1999.

[89] H. Daming, M. A. Reshchikov, and H. Morkoc, "Growth, structures, and optical properties of III-nitride quantum dots," *International Journal of High Speed Electronics and Systems*, vol. 12, no. 1, pp. 79–110, 2002.

[90] S. B. Brichkin and V. F. Razumov, "Colloidal quantum dots: synthesis, properties and applications," *Russian Chemical Reviews*, vol. 85, no. 12, pp. 1297–1312, 2016.

[91] C. B. Murray, D. J. Norris, and M. G. Bawendi, "Synthesis and characterization of nearly monodisperse CdE (E = S, Se, Te) semiconductor nanocrystallites," *Journal of the American Chemical Society*, vol. 115, no. 19, pp. 8706–8715, 1993.

[92] M. S. Mehata and R. K. Ratnesh, "Luminescence properties and exciton dynamics of core-multi-shell semiconductor quantum dots leading to QLEDs," *Dalton Transactions*, vol. 48, no. 22, pp. 7619–7631, 2019.

[93] B. Mahler, P. Spinicelli, S. Buil, X. Quelin, J. P. Hermier, and B. Dubertret, "Towards non-blinking colloidal quantum dots," *Nature Materials*, vol. 7, no. 8, pp. 659–664, 2008.

[94] A. M. Smith and S. Nie, "Semiconductor nanocrystals: structure, properties, and band gap engineering," *Acc Chem Res*, vol. 43, no. 2, pp. 190–200, 2010.

[95] W. N. Wenger, F. S. Bates, and E. S. Aydil, "Functionalization of Cadmium Selenide quantum dots with poly(ethylene glycol): Ligand exchange, surface coverage, and dispersion stability," *Langmuir*, vol. 33, no. 33, pp. 8239–8245, 2017.

[96] D. Vasudevan, R. R. Gaddam, A. Trinchi, and I. Cole, "Core-shell quantum dots: Properties and applications," *Journal of Alloys and Compounds*, vol. 636, pp. 395–404, 2015.

[97] Y. Varshni, "Temperature dependence of the energy gap in semiconductors," *Physica*, vol. 34, pp. 149–154, 1967.

[98] G. Chen, *Nanoscale Energy Transport and Conversion: A Parallel Treatment of Electrons, Molecules, Phonons and Photons*. Oxford University Press, 2005.

[99] J. W. Vandersande and C. Wood, "The thermal conductivity of insulators and semiconductors," *Contemp. Phys.*, vol. 27, no. 2, pp. 117–144, 1986.

[100] E. T. Swartz, "Thermal boundary resistance," *Rev. Mod. Phys.*, vol. 61, no. 3, pp. 605–668, 1989.

[101] T. Zeng and G. Chen, "Phonon heat conduction in thin films: Impacts of thermal boundary resistance and internal heat generation," *J. Heat Transfer*, vol. 123, no. 2, pp. 340–347, 2001.

[102] G. Chen, "Particularities of heat conduction in nanostructures," *J. Nanoparticle Res.*, vol. 2, no. 2, pp. 199–204, 2000.

[103] H. Kuzmany, *Solid State Spectroscopy: An introduction*. Springer-Verlag Berlin Heidelberg, 2009.

[104] C. V. Raman and K. S. Krishnan, "A new type of secondary radiation," *Nature*, vol. 121, p. 501–502, 1928.

[105] D. A. Long, *The Raman Effect: A Unified Treatment of The Theory of Raman Scattering by Molecules*. John Wiley Sons Ltd, 2002.

[106] S. P. Porto, J. A. Giordmaine, and T. C. Damen, "Depolarization of raman scattering in calcite," *Phys. Rev.*, vol. 147, p. 608–611, 1966.

[107] G. Pezzotti, H. Sueoka, and T. C. Damen, "Raman tensor elements for wurtzitic gan and their applications to assess crystallographic orientation at film/substrate interface," *Journal of Applied Physics*, vol. 10, pp. 013 527–1–013 527–10, 2011.

[108] M. Tsuboi, J. M. Benevides, and G. J. Thomas, "Raman tensors and their application in structural studies of biological systems," *Proceedings of the Japan Academy Series B: Physical and Biological Sciences*, vol. 85, no. 3, pp. 83–97, 2009.

[109] R. Loudon, "The Raman effect in crystals," *Advances in Physics*, vol. 13, no. 52, pp. 423–482, 1964.

[110] J. B. Cui, K. Amtmann, J. Ristein, and L. Ley, "Noncontact temperature measurements of diamond by Raman scattering spectroscopy," *Journal of Applied Physics*, vol. 83, no. 12, p. 7929–7933, 1998.

[111] K. R. Bagnall and E. N. Wang, "Contributed Review:Experimental characterization of inverse piezoelectric strain in GaN HEMTs via micro-Raman spectroscopy," *Review of Scientific Instruments*, vol. 87, pp. 061 501–1–061 501–22, 2016.

[112] V. Y. Davydov, Y. E. Kitaev, I. N. Goncharuk, A. N. Smirnov, J. Graul, O. Semchinov, D. Uffmann, M. B. Smirnov, A. P. Mirgorodsky, and R. A. Evarestov, "Phonon dispersion and Raman scattering in hexagonal GaN and AlN," *Physical Review B*, vol. 58, no. 19, 1998.

[113] J. Anaya, S. Rossi, M. Alomari, E. Kohn, L. Tóth, B. Pécz, and M. Kuball, "Thermal conductivity of ultrathin nano-crystalline diamond films determined by Raman thermography assisted by silicon nanowires," *Applied Physics Letters*, vol. 106, pp. 223 101–1–223 101–5, 2015.

[114] J. Dallas, G. Pavlidis, B. Chatterjee, J. S. Lundh, M. Ji, J. Kim, T. Kao, T. Detchprohm, R. D. Dupuis, S. Shen, S. Graham, and S. Choi, "Thermal characterization of gallium nitride p-i-n diodes," *Applied Physics Letters*, vol. 112, no. 7, 2018.

[115] N. Lundt, S. T. Kelly, T. Rödel, B. Remez, A. M. Schwartzberg, A. Ceballos, C. Baldasseroni, P. A. Anastasi, M. Cox, F. Hellman, S. R. Leone, and M. K. Gilles, "High spatial resolution Raman thermometry analysis of TiO_2 microparticles," *Review of Scientific Instruments*, vol. 84, pp. 104 906–1–104 906–7, 2013.

[116] J. Anaya, T. Bai, Y. Wang, C. Li, M. Goorsky, T. L. Bougher, L. Yates, Z. Cheng, S. Graham, K. D. Hobart, T. I. Feygelson, M. J. Tadjer, T. J. Anderson, B. B. Pate, and M. Kuball, "Simultaneous determination of the lattice thermal conductivity and grain/grain thermal resistance in polycrystalline diamond," *Acta Materialia*, vol. 139, pp. 215–225, 2017.

[117] J. Gernot, "Time resolved Raman thermography : Thermal dynamics of GaN-based electronic devices," Ph.D. dissertation, University of Bristol, 2010.

[118] Q. F. I. Corp., *InfraScope User's Manual*, 2003.

[119] K. R. Bagnall, "Device-level thermal analysis of GaN-based electronics," Master's thesis, Massachusetts Institute of Technology, 2009.

[120] E. L. Radue, J. A. Tomko, A. Giri, J. L. Braun, X. Zhou, O. V. Prezhdo, E. L. Runnerstrom, J.-P. Maria, and P. E. Hopkins, "Hot electron thermoreflectance coefficient of gold during electron-phonon nonequilibrium," *ACS Photonics*, vol. 5, no. 12, pp. 4880–4887, 2018.

[121] D. Kendig, K. Yazawa, and A. Shakouri, "Hyperspectral thermoreflectance imaging for power devices ," in *Proc.3rd SEMI-THERM Symposium*, San Jose, CA, USA, 2017, pp. 2–5.

[122] D. I. Yakubovsky, A. V. Arsenin, Y. V. Stebunov, D. Y. Fedyanin, and V. S. Volkov, "Optical constants and structural properties of thin gold films," *Optics Express*, vol. 25, no. 21, p. 25574, 2017.

[123] G. Tessier, S. Holé, and D. Fournier, "Quantitative thermal imaging by synchronous thermoreflectance with optimized illumination wavelengths," *Applied Physics Letters*, vol. 78, no. 16, pp. 2267–2269, 2001.

[124] B. Öner, J. W. Pomeroy, and M. Kuball, "Submicron resolution hyperspectral quantum rod thermal imaging of microelectronic devices," *ACS Appl. Electron. Mater.*, vol. 2, pp. 93–102, 2020.

[125] Y. Garini, I. T. Young, and G. Mcnamara, "Spectral imaging : principles and applications," *Cytometry Part A*, vol. 69, no. 8, pp. 735–747, 2006.

[126] J. M. Prats-Montalbán, A. de Juan, and A. Ferrer, "Multivariate image analysis: A review with applications," *Chemometrics and Intelligent Laboratory Systems*, vol. 107, no. 1, pp. 1–23, 2011.

[127] P. R. Edwards, L. K. Jagadamma, J. Bruckbauer, C. Liu, P. Shield, D. Allsopp, T. Wang, and R. W. Martin, "High-Resolution cathodoluminescence hyperspectral imaging of nitride nanostructures," *Microscopy and Microanalysis*, vol. 18, no. 6, pp. 1212–1219, 2012.

[128] H. Liang, "Advances in multispectral and hyperspectral imaging for archaeology and art conservation," *Appl Phys A*, vol. 106, pp. 309–323, 2012.

[129] J. R. Mansfield, "Multispectral imaging : A review of its technical aspects and applications in anatomic pathology," vol. 51, no. 1, pp. 185–210, 2014.

[130] T. Udelhoven, M. Schlerf, K. Segl, K. Mallick, C. Bossung, R. Retzlaff, G. Rock, P. Fischer, A. Müller, T. Storch, A. Eisele, D. Weise, W. Hupfer, and T. Knigge, "A satellite-based imaging instrumentation concept for hyperspectral thermal remote sensing," *Sensors*, vol. 1542, pp. 1–16, 2017.

[131] NEO, "Hyperspectral imaging," 2019, last accessed 1 July 2019. [Online]. Available: https://www.hyspex.no

[132] Resonon, "Hyperspectral applications," 2019, last accessed 1 July 2019. [Online]. Available: https://resonon.com/applications

[133] X. Zhong, J. Labed, G. Zhou, K. Shao, and Z. L. Li, "A multi-channel method for retrieving surface temperature for high-emissivity surfaces from hyperspectral thermal infrared images," *Sensors*, vol. 15, no. 6, pp. 13 406–13 423, 2015.

[134] Thorlabs, "Kurios liquid cyrstal tunable bandpass filters," 2019, last accessed 1 July 2019. [Online]. Available: https://www.thorlabs.com/newgrouppage9.cfm?objectgroup_id=3488&pn=KURIOS-WB1l

[135] E. Hect, *Optics*. Adison Wesley, 2002.

[136] T. Brazzini, H. Sun, F. Sarti, J. W. Pomeroy, C. Hodges, M. Gurioli, A. Vinattieri, M. J. Uren, and M. Kuball, "Mechanism of hot electron electroluminescence in GaN-based transistors," *Journal of Physics D: Applied Physics*, vol. 49, no. 43, pp. 435 101–1–6, 2016.

[137] B. T. Diroll and C. B. Murray, "High-temperature photoluminescence of CdSe/CdS core/shell nanoheterostructures," *ACS Nano*, vol. 8, no. 6, pp. 6466–6474, 2014.

[138] T. Brazzini, M. A. Casbon, H. Sun, M. J. Uren, J. Lees, P. J. Tasker, H. Jung, H. Blanck, and M. Kuball, "Electroluminescence of hot electrons in AlGaN/GaN high-electron-mobility transistors under radio frequency operation," *Applied Physics Letters*, vol. 106, no. 21, pp. 213 502–1–213 502–4, 2015.

[139] M. Tapajna, N. Killat, V. Palankovski, D. Gregusova, K. Cico, J. F. Carlin, N. Grandjean, M. Kuball, and J. Kuzmik, "Hot-electron-related degradation in InAlN/GaN high-electron-mobility transistors," *IEEE Transactions on Electron Devices*, vol. 61, no. 8, pp. 2793–2801, 2014.

[140] C. Shannon, "Communication in the presence of noise (Republished)," *Proceedings of the IEEE*, vol. 86, no. 2, pp. 447–457, 1998.

[141] C. Cremer and B. R. Masters, "Resolution enhancement techniques in microscopy," *European Physical Journal H*, vol. 38, no. 3, pp. 281–344, 2013.

[142] S. E. Reichenbach, "Characterizing digital image acquisition devices," *Optical Engineering*, vol. 30, no. 2, pp. 170–177, 1991.

[143] "Standard practice for minimum resolvable temperature difference for thermal imaging systems," ASTM Standards, PA, Standard, 2018.

[144] Electrophysics, "Infrared inspection white paper: Understanding infrared camera thermal image quality," 2011, last accessed 20 August 2019. [Online]. Available: https://www.electrophysics.com

[145] M. Guizar-Sicairos, T. Thurman, and J. Fienup, "Efficient subpixel image registration algorithms," *Optics Letter*, vol. 33, no. 2, pp. 156–158, 2008.

[146] M. Notomi, M. Okamoto, and T. Tamamura, "Study of the factors affecting the broadening of the photoluminescence spectra of InGaAs/InP quantum wires," *Journal of Applied Physics*, vol. 75, no. 8, pp. 4161–4166, 1994.

[147] T. G. Mack, L. Jethi, and P. Kambhampati, "Temperature dependence of emission line widths from semiconductor nanocrystals reveals vibronic contributions to line broadening processes," *Journal of Physical Chemistry C*, vol. 121, no. 51, pp. 28 537–28 545, 2017.

[148] O. Chen, J. Zhao, V. P. Chauhan, J. Cui, C. Wong, D. K. Harris, H. Wei, H. S. Han, D. Fukumura, R. K. Jain, and M. G. Bawendi, "Compact high-quality CdSe-CdS core-shell nanocrystals with narrow emission linewidths and suppressed blinking," *Nature Materials*, vol. 12, no. 5, pp. 445–451, 2013.

[149] I. Sychugov, A. Fucikova, F. Pevere, Z. Yang, J. G. Veinot, and J. Linnros, "Ultranarrow luminescence linewidth of silicon nanocrystals and influence of matrix," *ACS Photonics*, vol. 1, no. 10, pp. 998–1005, 2014.

[150] A. Narayanaswamy, L. F. Feiner, A. Meijerink, and P. J. van der Zaag, "The effect of temperature and dot size on the spectral properties of colloidal InP/ZnS core-shell quantum dots," *ACS Nano*, vol. 3, no. 9, pp. 2539–2546, 2009.

[151] M. Pelton, J. J. Andrews, I. Fedin, D. V. Talapin, H. Leng, and S. K. O'Leary, "Nonmonotonic dependence of Auger recombination rate on shell thickness for CdSe/CdS core/shell nanoplatelets," *Nano Letters*, vol. 17, no. 11, pp. 6900–6906, 2017.

[152] X. F. Liu, R. Wang, Y. P. Jiang, Q. Zhang, X. Y. Shan, and X. H. Qiu, "Thermal conductivity measurement of individual CdS nanowires using microphotoluminescence spectroscopy," *Journal of Applied Physics*, vol. 108, no. 5, 2010.

[153] R. D. Deegan, O. Bakajin, and T. F. Dupont, "Capillary flow as the cause of ring stains from dried liquid drops," *Nature*, vol. 389, pp. 827–829, 1997.

[154] Y. Ooi, I. Hanasaki, D. Mizumura, and Y. Matsuda, "Suppressing the coffee-ring effect of colloidal droplets by dispersed cellulose nanofibers," *Science and Technology of Advanced Materials*, vol. 18, no. 1, pp. 316–324, 2017.

[155] C. Leys, C. Ley, O. Klein, P. Bernard, and L. Licata, "Detecting outliers: Do not use standard deviation around the mean, use absolute deviation around the median," *Journal of Experimental Social Psychology*, vol. 49, no. 4, pp. 764–766, 2013.

[156] A. Sarua, H. Ji, M. Kuball, M. J. Uren, T. Martin, K. P. Hilton, and R. S. Balmer, "Integrated micro-Raman / infrared thermography probe for monitoring of self-Heating in AlGaN / GaN transistor structures," *IEEE Transactions on Electron Devices*, vol. 53, no. 10, pp. 2438–2447, 2006.

[157] N. Killat, M. Kuball, T. M. Chou, U. Chowdhury, and J. Jimenez, "Temperature assessment of AlGaN/GaN HEMTs: A comparative study by Raman, electrical and IR thermography," *IEEE International Reliability Physics Symposium Proceedings*, pp. 528–531, 2010.

[158] W. Liu and A. A. Balandin, "Temperature dependence of thermal conductivity of $Al_xGa_{1-x}N$ thin films measured by the differential 3ω technique," *Applied Physics Letters*, vol. 85, no. 22, p. 5230, 2004.

[159] J. W. Pomeroy, M. Bernardoni, D. C. Dumka, D. M. Fanning, and M. Kuball, "Low thermal resistance GaN-on-diamond transistors characterized by three-dimensional Raman thermography mapping," *Applied Physics Letters*, vol. 104, no. 8, pp. 1–6, 2014.

[160] T. Batten, J. W. Pomeroy, M. J. Uren, T. Martin, and M. Kuball, "Simultaneous measurement of temperature and thermal stress in AlGaN/GaN high electron mobility transistors using Raman scattering spectroscopy," *Journal of Applied Physics*, vol. 106, no. 9, pp. 094 509–1–094 509–4, 2009.

[161] A. Darwish, A. J. Bayba, and H. A. Hung, "Channel temperature analysis of GaN HEMTs with nonlinear thermal conductivity," *IEEE Transactions on Electron Devices*, vol. 62, no. 3, pp. 840–846, 2015.

[162] S. A. Empedocles and M. G. Bawendi, "Quantum-confined stark effect in single cdSe nanocrystallite quantum dots," *Science*, vol. 278, no. 5346, pp. 2114–2117, 1997.

[163] K. Park, Z. Deutsch, J. J. Li, D. Oron, and S. Weiss, "Single molecule quantum-confined Stark effect measurements of semiconductor nanoparticles at room temperature," *ACS Nano*, vol. 6, no. 11, pp. 10 013–10 023, 2012.

[164] K. Park and S. Weiss, "Design rules for membrane-embedded voltage-sensing nanoparticles," *Biophys. J.*, vol. 112, no. 4, pp. 703–713, 2017.

[165] J. Muller, J. M. Lupton, P. G. Lagoudakis, F. Schindler, R. Koeppe, A. L. Rogach, J. Feldmann, D. V. Talapin, and H. Weller, "Wave function engineering in elongated semiconductor nanocrystals with heterogeneous carrier confinement," *Nano Lett.*, vol. 5, no. 10, pp. 2043–2049, 2005.

[166] O. Bar-Elli, D. Steinitz, G. Yang, R. Tenne, A. Ludwig, Y. Kuo, A. Triller, S. Weiss, and D. Oron, "Rapid voltage sensing with single nanorods via the quantum confined Stark effect," *ACS Photonics*, vol. 5, no. 7, pp. 2860–2867, 2018.

[167] "The European project PROFIT: Prediction of temperature gradients influencing the quality of electronic products," *Annual IEEE Semiconductor Thermal Measurement and Management Symposium*, pp. 120–125, 2001.

[168] A. Qian, M. Gheitaghy, J. Fan, H. Tang, B. Sun, H. Ye, and G. Zhang, "Thermal management on IGBT power electronic devices and modules," *IEEE Access*, vol. 6, pp. 12 868–12 884, 2018.

[169] F. M. Barradas, L. C. Nunes, T. R. Cunha, P. M. Lavrador, P. M. Cabral, and J. C. Pedro, "Compensation of long-term memory effects on GaN HEMT-based power amplifiers,"

IEEE Transactions on Microwave Theory and Techniques, vol. 65, no. 9, pp. 3379–3388, 2017.

[170] B. Öner, J. W. Pomeroy, and M. Kuball, "Time resolved hyperspectral quantum rod thermography of microelectronic devices: Temperature transients in a GaN HEMT," *IEEE Electron Device Lett.*, vol. 41, no. 6, pp. 812–815, 2020.

[171] D. F. Holcomb and R. E. Norberg, "Nuclear spin relaxation in alkali metals," *Physical Review*, vol. 98, no. 4, pp. 1074–1091, 1955.

[172] P. Fimpel, C. Riek, L. Ebner, A. Leitenstorfer, D. Brida, and A. Zumbusch, "Boxcar detection for high-frequency modulation in stimulated Raman scattering microscopy," *Applied Physics Letters*, vol. 112, no. 16, pp. 2–5, 2018.

[173] M. M Farzaneh, K. Maize, D. L¨uerßen, J. Summers, P. Mayer, P. Raad, K. Pipe, A. Shakouri, R. Ram, and J. A. Hudgings, "CCD-based thermoreflectance microscopy : principles and applications," *Journal of Physics D: Applied Physics*, vol. 42, pp. 143 001–1–20, 2009.

[174] Thorlabs, "Camera noise and temperature tutorial," 2019, last accessed 24 September 2019. [Online]. Available: https://www.thorlabs.com/newgrouppage9.cfm?objectgroup_id=10773

[175] A. Shakouri, A. Ziabari, D. Kendig, J. H. Bahk, Y. Xuan, P. D. Ye, K. Yazawa, and A. Shakouri, "Stable thermoreflectance thermal imaging microscopy with piezoelectric position control," *Annual IEEE Semiconductor Thermal Measurement and Management Symposium*, vol. Part F121464, pp. 128–132, 2016.

[176] S. Martin-Horcajo, J. W. Pomeroy, B. Lambert, H. Jung, H. Blanck, and M. Kuball, "Transient thermoreflectance for gate temperature assessment in pulse operated GaN-based HEMTs," *IEEE Electron Device Letters*, vol. 37, no. 9, pp. 1197–1200, 2016.

[177] M. Farzaneh, K. Maize, D. Lüerßen, J. A. Summers, P. M. Mayer, P. E. Raad, K. P. Pipe, A. Shakouri, R. J. Ram, and J. A. Hudgings, "CCD-based thermoreflectance microscopy:

principles and applications," *Journal of Physics D: Applied Physics*, vol. 42, no. 14, p. 143001, 2009.

[178] R. B. Wilson, B. A. Apgar, L. W. Martin, and D. G. Cahill, "Thermoreflectance of metal transducers for optical pump-probe studies of thermal properties," *Optics express*, vol. 20, no. 27, pp. 28 829–38, 2012.

[179] D. U. Kim, K. S. Park, C. B. Jeong, G. H. Kim, and K. S. Chang, "Quantitative temperature measurement of multi- layered semiconductor devices using spectroscopic thermoreflectance microscopy," *Opt. Express*, vol. 24, no. 13, pp. 950–960, 2016.

[180] S. Dilhaire, S. Grauby, and W. Claeys, "Calibration procedure for temperature measurements by thermoreflectance under high magnification conditions," *Applied Physics Letters*, vol. 84, no. 5, pp. 822–824, 2004.

[181] T. Favaloro, J. H. Bahk, and A. Shakouri, "Characterization of the temperature dependence of the thermoreflectance coefficient for conductive thin films," *Review of Scientific Instruments*, vol. 86, pp. 024 903–1–024 903–9, 2015.

[182] Q. D. Europe, "Highest speed cameras," 2019, last accessed 19 September 2019. [Online]. Available: https://lot-qd.de/en/products/imaging/highest-speed-cameras/

[183] J. B. Baliga, *Gallium nitride and silicon carbide power devices*. World Scientific, 2017.

[184] Y. Won, J. Cho, D. Agonafer, M. Asheghi, and K. E. Goodson, "Fundamental cooling limits for high power density GaN electronics," *IEEE Transaction on Components, Packaging, and Manufacuring Technology*, vol. 5, no. 6, pp. 737–744, 2015.

[185] A. Bar-Cohen, J. D. Albrecht, and J. J. Maurer, "Near-junction thermal management for wide bandgap devices," *Technical Digest - IEEE Compound Semiconductor Integrated Circuit Symposium, CSIC*, pp. 1–5, 2011.

[186] J. Kuzmik, S. Bychikhin, E. Pichonat, C. Gaquie're, E. Morvan, E. Kohn, J.-P. Teyssier, and D. Pogany, "Self-heating phenomena in high-power III-N transistors and new thermal characterization methods developed within EU project," vol. 1, no. 2, pp. 153–160, 2017.

[187] O. Hilt, R. Zhytnytska, J. Bocker, E. Bahat-Treidel, F. Brunner, A. Knauer, S. Dieckerhoff, and J. Wurfl, "70 m-ohm/600 V normally-off GaN transistors on SiC and Si substrates," *Proceedings of the International Symposium on Power Semiconductor Devices and ICs*, vol. 2015-June, no. 287602, pp. 237–240, 2015.

[188] A. Vertikov, M. Kuball, A. V. Nurmikko, and H. J. Maris, "Time-resolved pump-probe experiments with subwavelength lateral resolution," *Appl. Phys. Lett.*, vol. 69, no. 17, pp. 2465–2467, 1996.

[189] P. Bazylewski, S. Ezugwu, and G. Fanchini, "A review of three-dimensional scanning near-field optical microscopy (3D-SNOM) and its applications in nanoscale light management," *Appl. Sci.*, vol. 7, no. 10, 2017.

[190] S. Farsiu, D. Robinson, M. Elad, and P. Milanfar, "Advances and challenges in super-resolution," *International Journal of Imaging Systems and Technology*, vol. 14, no. 2, pp. 47–57, 2004.

[191] C. P. Sung, K. P. Min, and M. G. Kang, "Super-resolution image reconstruction: a technical overview," *IEEE Signal Processing Magazine*, vol. 20, no. 3, pp. 21–36, 2003.

[192] A. M. Tekalp, M. K. Ozkan, and M. I. Sezan, "High-resolution image reconstruction from lower-resolution image sequences and space-varying image restoration," in *International Conference on Acoustics, Speech, and Signal Processing*, San Francisco, CA, USA, USA, 1992, pp. 169–172.

[193] Z. Qiu, R. S. Wilson, Y. Liu, A. R. Dun, R. S. Saleeb, D. Liu, C. Rickman, M. Frame, R. R. Duncan, and W. Lu, "Translation microscopy (TRAM) for super-resolution imaging," *Scientific Reports*, vol. 6:19993, pp. 1–10, 2016.

[194] S. G. Kwak and J. H. Kim, "Central limit theorem: the cornerstone of modern statistics," *Korean J Anesth.*, vol. 70, no. 2, pp. 144–156, 2017.

[195] A. Ziabari, J. H. Bahk, Y. Xuan, P. D. Ye, D. Kendig, K. Yazawa, P. G. Burke, H. Lu, A. C. Gossard, and A. Shakouri, "Sub-diffraction limit thermal imaging for HEMT devices," *Annu. IEEE Semicond. Therm. Meas. Manag. Symp.*, no. 1, pp. 82–87, 2015.